UNIVERSITY OF OKLAHOMA

GRADUATE COLLEGE

MICROPHYSICAL PROPERTIES OF ICE CRYSTAL GROWTH REVEALED IN

POLARIMETRIC RADAR DATA

A THESIS

SUBMITTED TO THE GRADUATE FACULTY

In partial fulfillment of the requirements for the

Degree of

MASTER OF SCIENCE IN METEOROLOGY

By

JELENA ANDRIĆ
Norman, Oklahoma
2011

MICROPHYSICAL PROPERTIES OF ICE CRYSTAL GROWTH REVEALED IN
POLARIMETRIC RADAR DATA

A THESIS APPROVED FOR THE
SCHOOL OF METEOROLOGY

BY

_____
Dr. Dusan Zrnić, chair

_____
Dr. Jerry Straka

_____
Dr. Guifu Zhang

_____
Dr. Valery Melnikov

ACKNOWLEDGEMENTS

TABLE OF CONTENTS

LIST OF TABLES

LIST OF FIGURES

ABSTRACT

A polarimetric signature characterized by a large gradient of Z_H, enhanced Z_{DR} and reduced ρ_{hv} has been observed at approximately 4.5 km AGL, above the melting layer in winter stratiform clouds. With a focus on levels above the melting layer, we are investigating the potential of S-band dual-polarization radar to provide an insight into the microphysical structure of winter clouds. Vertical profiles and high-resolution RHIs of the polarimetric variables, Z_H, Z_{DR}, ρ_{hv}, and K_{DP}, observed with KOUN (research polarimetric radar, located in Norman, OK) during mixed winter precipitation, have been examined. The focus is on the nature of the enhanced Z_{DR} signature as well as the ρ_{hv} signature that appears at the same level.

Near-zero values of Z_{DR} at the cloud top suggest the presence of nearly spherical particles. From the cloud top downward, Z_{DR} increases up to a maximum of 2.5 dB, at approximately 4.5 km, AGL. These values suggest the presence of horizontally oriented plate-like crystals. Enhanced Z_{DR} is followed by decreasing of ρ_{hv} with height. Also, a slightly increased vertical gradient of Z_H is observed. Z_{DR} decreases quite rapidly below 4.5 km, where snow aggregates are expected to be dominant. Since Z_{DR} is strongly dependent on particle density, interpretation of this signature requires knowledge about the nature of growth process of ice crystals at the enhanced Z_{DR} level. The one-dimensional, two-moment microphysical scheme of ice crystal growth along with the scattering model is used in attempt to replicate the observed polarimetric signature. The two-moment microphysical scheme includes the processes of nucleation, deposition, riming, and aggregation, while the scattering model calculates Z_H, Z_{DR}, ρ_{hv} and K_{DP} using

the microphysical scheme's output. Results from the model show fair agreement with the observed polarimetric signature from the considered winter case.

1. Introduction

The significance of polarimetric radar, used for detection, tracking, and analysis of convective, as well as stratiform storms, is already well known. Polarimetric variables introduce new information regarding the microphysical and dynamical structure of convective storms (Kumjian and Ryzhkov 2008a,b; Kumjian and Ryzhkov 2009; Kumjian et al. 2010). The National Oceanic and Atmospheric Administration's (NOAA) research and development polarimetric radar KOUN employs a polarimetric mode with simultaneous transmission and reception of horizontally (H) and vertically (V) polarized waves (Doviak et al. 2000). In addition to the standard spectral moments, KOUN routinely measures the following polarimetric variables: 1) differential reflectivity (Z_{DR}), 2) differential phase (Φ_{DP}), and 3) copolar correlation coefficient (ρ_{hv}), (e.g., Doviak and Zrnic, 2006, section 6.8).

One of the most challenging goals of radar polarimetry is icing detection. The main characteristics of icing conditions are subfreezing temperatures and presence of supercooled liquid droplets of various sizes. Direct radar detection of smaller-sized droplets is not possible. The challenge is to understand how detectable are crystals that grow in icing conditions, or how detectable are the consequences of presence of small supercooled liquid droplets. The enhanced Z_{DR} signature above the melting layer, observed in winter stratiform clouds has been investigated in several other studies (Hogan et al. 2002; Moisseev et al. 2009; Kennedy and Rutledge 2011). It is important to understand the real nature of enhanced Z_{DR} signature because it can be used as additional information in icing detection applications. In this study, data collected during the 2009

winter, indicative of ice crystal habit and dominant growth process are analyzed in an attempt to provide answers regarding processes that lead to observed polarimetric signatures above the melting layer. In order to do that a one-dimensional model, coupled with microphysical and scattering component is used in attempt to reproduce the observed polarimetric signature.

The following chapter provides the background for cloud physics with a focus on ice crystal properties, their growth processes, as well as a literature review of relevant ice crystal studies. The third chapter gives the background for radar polarimetric variables, their definitions and typical values, but also their characteristics related to analyses of winter stratiform clouds. The synoptic situation for the studied winter storm is given at the beginning of the chapter four, followed by the description of the data used for analysis. At the end of this chapter, studies that used radar polarimetry to investigate microphysical structure of stratiform clouds are reviewed. Chapter five contains a description of the microphysical scheme and scattering model that have been used. Finally, results along with discussion are presented in chapter six.

2. Microphysical properties of ice crystals

Knowledge of the cloud physics is one the most important aspects for accurate interpretation and understanding of radar data, especially polarimetric data. Radar polarimetric data can be used for studying the microphysical cloud structure, precipitation particles and their life cycle from the moment they form until they reach the ground along with microphysical processes occurring during that cycle. Since the subject of this study is winter stratiform clouds, this chapter focuses on the ice phase particles and processes. Ice crystals appear in a great variety of shapes (habits) and related literature is quite extensive, thus only ice crystal habits that are important for the analysis of the observed polarimetric data are described.

2.1 Shape, size and concentration of ice crystals

Snow crystals appear in a large variety of shapes. However, detailed laboratory studies reveal that snow crystals have one common basic shape: hexagonal prism with two basal planes of type **a,** and six prism planes of type **b**, (Fig. 2.1).
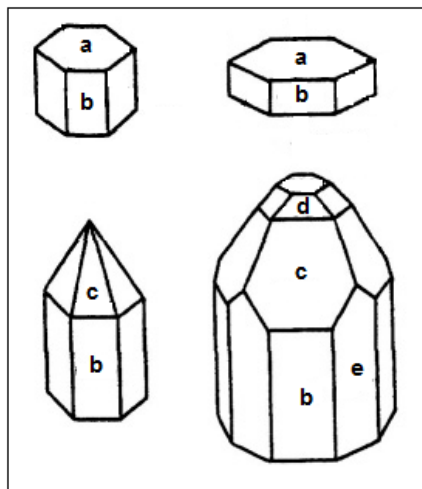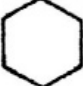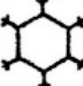
Figure 2.1: Schematic representation of two basic ice crystals shapes. (Adapted from Pruppacher and Klett 1997)

Faces marked with **c**, **d** and **e** (Fig. 2.1) grow quickly to become the crystal's edges and corners, whereas faces marked with **a** and **b** grow slowly and become the bounding faces of the crystal. The rate of growth along the crystallographic direction of type **a** or type **b** is a function of temperature and supersaturation with respect to ice (Nakaya 1954; Mason and Shaw 1955; Kobayashi 1957, 1958; Hallett and Mason 1958). The slowest growing faces will determine the habit of the crystal. Table 2.1 represents selected ice crystal habits from the Magono-Lee (1966) classification of natural crystals, relevant to this study. Some of these habits are included in microphysical scheme that is presented in Chapter 5.

Table 2.1: Selected ice crystal habits from the Magono-Lee classification of natural crystals. (Adapted from Magono and Lee 1966)

	N1a Elementary needle		C1g Solid thick plate		P1e Ordinary dendritic crystal
	N1c Elementary sheath		P1a Hexagonal plate		P2c Dentritic crystal with plates at ends
	N1e Long solid column		P1c Crystal with broad branches		P2e Plate with simple extensions
	C1e Solid column		P1d Stellar crystal		P2f Plate with dentritic extensions
	C1f Hollow column		P1b Crystal with sectorlike branches		P3a Two-branched crystal

As shown in Fig. 2.2, with decreasing temperature and with high supersaturation with respect to ice, crystals change their habit in a cyclic manner from a plate to needle to column, to a sector plate, to a dendrite, back to a sector plate and again to a column.

These changes in shape are due to a cyclic change in preferential growth direction along the crystallographic direction of type **a** or **b**, and they occur at temperatures near -4 °C, -9 °C (relatively sharp change) and -22 °C (change in temperature range centered around -22 °C).
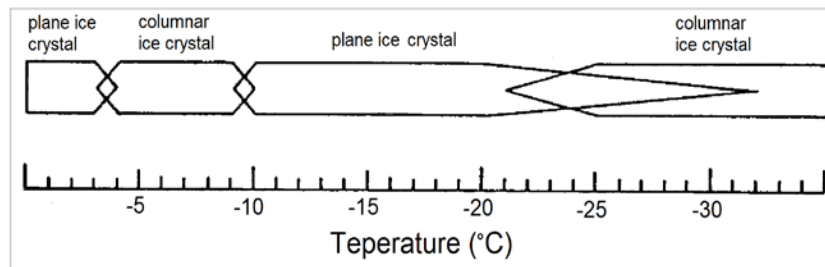
Figure 2.2: Simplified representation of ice crystals habit dependence on temperature. (Adapted from Ono 1970)

Fig. 2.3 from Young (1993) shows how supersaturation with respect to ice affects the growth properties of ice crystals. With increasing vapor density excess, and near -15 °C, ice crystals habit changes from thick plate to thin plate, to a sector plate and to a dendrite. Near -5 °C and with increasing vapor density excess ice crystal habits vary from a short solid column, to a hollow column, to a needle. Laboratory observations (Kobayashi 1965a,b; Kumai 1982) have not shown new ice crystal habits at temperature range of -22 °C to -50 °C. Sheaths (long solid columns) appear between -45 °C and -50 °C, at low supersaturation, but they change into hollow columns for high supersaturation. These conclusions drawn from laboratory observations initially are supported by a number of observations of natural ice crystals from different parts of the world (Bailey and Hallett 2009; Korolev *et al.* 1999).
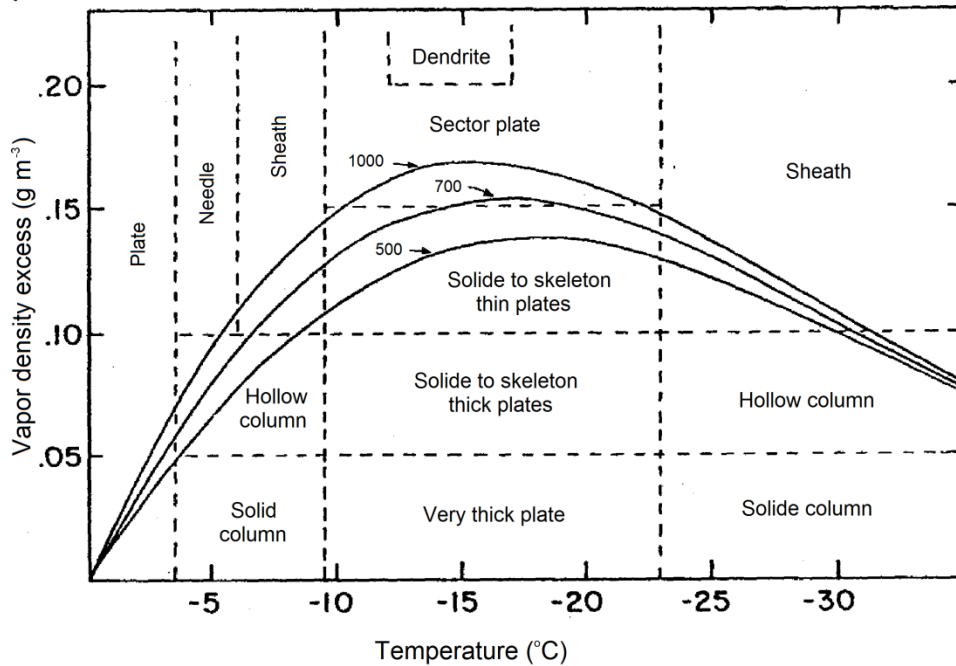
Figure 2.3: The growth of natural ice crystals of different habit in different temperature and humidity conditions based on laboratory observations. (Young 1993)

In general, the size of an ice crystal is characterized by two dimensions: the diameter (horizontal axis) and the thickness (vertical axis) for plate-like crystals, and the length (horizontal axis) and the width (vertical axis) for columnar crystals. From measurements obtained at several locations, the typical size of plate-like crystals range from 20 µm to 2 mm for diameter and 10 to 60 µm for thickness. Typical sizes for columnar crystals range from 20 µm to 2 mm in length, and 10 to 60 µm for thickness, whereas width ranges from 10 to 200 µm. Crystals grow in such a manner that if the diameter (the length) of planar (columnar) crystals increases then the thickness (the width) also increases.

The newer results from laboratory experiments and over a million CPI images of in situ observations of ice crystals from a broad range of cloud types resulted in a new habit diagram (Bailey and Hallett 2008). The new habit diagram given in Fig. 2.4, agrees

6

well with older diagrams (Magono and Lee 1966; Young 1993) showing that temperature range of 0 °C to -4 °C and -8 °C to -22 °C is favorable for plate-like crystals, and temperature range of -4 °C to -8 °C for columns. However, the new habit diagram reveals that for temperatures below -18 °C, polycrystals of two distinct habit regimes dominate, plate-like from -20 °C to -40 °C, and columnar crystals from -40 °C to -70 °C. Another new and important feature of this diagram is the emphasis on the irregularity and complexity of most single crystals, which is in agreement with observations by Korolev et al. (1999; 2000).
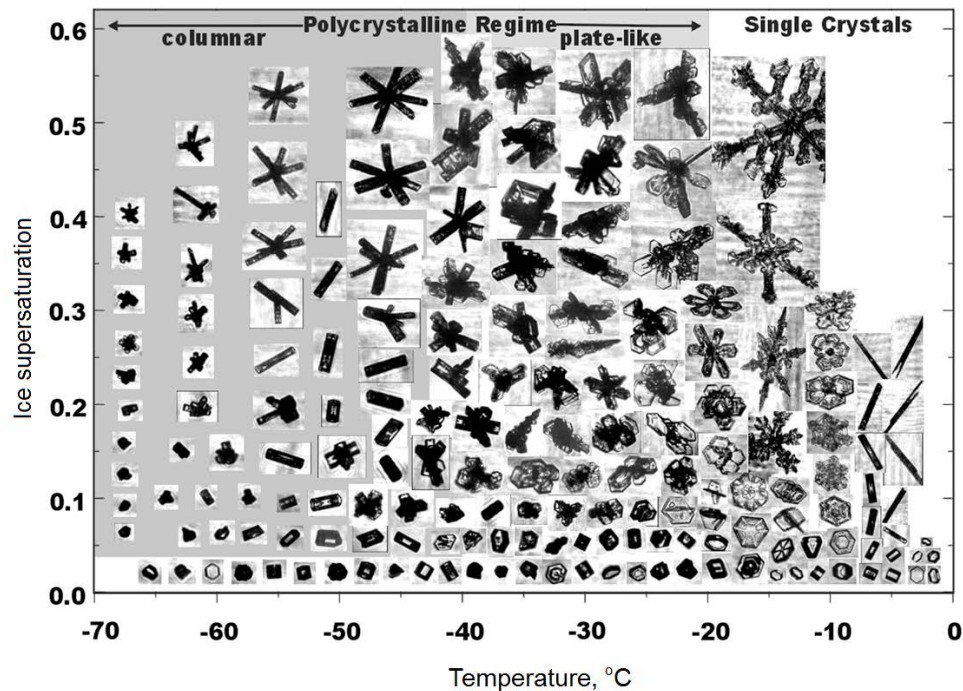
Figure 2.4: The habit diagram constructed from laboratory experiments along with CPI images of natural ice crystals. (Adapted from Bailey and Hallett 2008)

Ice crystals usually grow in skeletal fashion and thus they have small amounts of air in capillary spaces. As a result, ice crystals have densities lower than the density of solid ice, which is 0.917 g cm^{-3}. Observations taken by Iwai (1973) and Jayaweera and Ohtake (1974) show that short columns have densities close to that of solid ice. They

7

observed that with increasing column length, density decreases rapidly, reaching value of 0.5 g cm^{-3} for length of 1 mm. In the case of needles and sheaths, density is 0.3 to 0.4 g cm^{-3} for lengths larger than 1 mm.

Aside from vapor and temperature gradients, crystal surface forces are very important for crystal growth. These forces depend on ice crystal faces and control the incorporation of water molecules into the ice lattice, as a function of temperature. At an early stage of crystal growth, if vapor density excess is low to moderate, the crystal habit is determined by surface kinetic effects. Vapor flux to the corners and edges of the crystal is successfully redistributed by surface diffusion, so that geometry of the crystal can not significantly alter. This is not the case when there is high vapor density excess, and surface diffusion can not compensate for large non-uniform vapor deposition. Consequently, further growth will be at the corners and edges of the crystal, resulting in formation of dendrites, stellars, sector plates, etc.

Classifications of ice crystals depict diversity of particle types, but they provide no information about ice crystal frequency or spatial distribution of occurrence. Korolev et al. (1999) made aircraft measurements in Arctic clouds within the temperature range from 0 °C to -45 °C. They divided particles with maximum dimension exceeding 40 µm, into two categories: pristine (faceted ice single crystal) and irregular crystals. They found that 97% of ice particles were irregular and evenly distributed in all size categories, and only 3% were pristine. Possible causes of irregular ice formation are: fluctuations of supersaturation, freezing of droplets as polycrystals (Hallett 1964), and growth from the vapor on droplets, which froze individually or by accretion onto other snow crystals. Korolev et al. (2000) studied the frequency of occurrence of different habits of ice

particles in natural clouds from aircraft observations. They have collected data over the Great Lakes and in the Canadian and US Arctic over the North Atlantic, near Newfoundland. Cloud particles were classified into four categories: spheres, irregulars, needles/columns and dendrites. Classification of particles by size was done for three size ranges: >125 µm, >250 µm, and >500 µm. Mostly, data were collected in stratiform clouds (St, Sc, Ns, As, Ac) related to frontal systems. In a number of flights, 95% – 98% of all particles were classified as irregular. On average, irregular particles with diameters >125 µm are more common than those with diameters >500 µm. For particles with diameters >125 µm and >250 µm, the fraction of irregular particles gradually increases from 69% and 63% at 0 ℃, to 95% and 97% at -40 ℃, respectively (Korolev *et al*. 2000).

The maximum frequency of occurrence of dendrites was observed at temperatures ranging from -15 ℃ to -10 ℃, which agrees with laboratory observations. However, in this temperature range, instead of dendrites, irregular particles were observed in the majority of cases. Also, a significant number of dendrites were observed in the temperature range from -10 °C to 0 °C, which does not correspond to the Magono-Lee diagram (Korolev *et al.* 2000). The fraction of dendrites can reach 100% in isolated cells embedded in zones of irregular particles, suggesting that dendritic formation occurs only in limited conditions. The size of these cells ranges from hundreds of meters to tens of kilometers.

The maximum frequency of occurrence of needles is in the temperature range of -5 °C to 0 °C, which is in agreement with laboratory studies. On average, the fraction of needles is about 6% for diameter >125 µm and >500 µm. In many cases, dendrites and needles at temperatures from -5 °C to 0 °C, and columns at temperatures -45 °C to -40 °C

occurred in isolated cells. Within these cells needles are frequently mixed with irregulars and rarely with dendrites.

The fraction of spherical particles, within size intervals 125 µm and 500 µm, on average is 7% to 6%. A fraction of 6 to 20% of spherical particles, associated with freezing drizzle events, was observed at a temperature of interval -10 °C to 0 °C. At lower temperatures, the fraction of spherical particles is decreased and reaches 0% at range -40 °C to -45 °C for diameters >125 µm, and similarly for diameters > 500 µm. The estimated average particle number concentrations for ice particles with diameters > 125 µm, 250 µm, and 500 µm, obtained from Arctic, maritime and continental stratiform clouds are given in Fig. 2.5 (Korolev *et al*. 2000). For temperature interval of 0 °C to -35 °C, number concentration of particles with diameters > 125 µm is 3 to 4 l^{-1} and mostly constant, with a sharp decrease below -35 °C. The concentration of particles with diameters > 250 µm is about 1.5 to 1.8 l^{-1} and it is constant for temperatures higher than -30°C, but decreases for temperatures below -30 °C. The concentration of largest particles, with diameters > 500 µm reaches maximum of 1.2 l^{-1} at -15 °C, and decreases below this temperature.
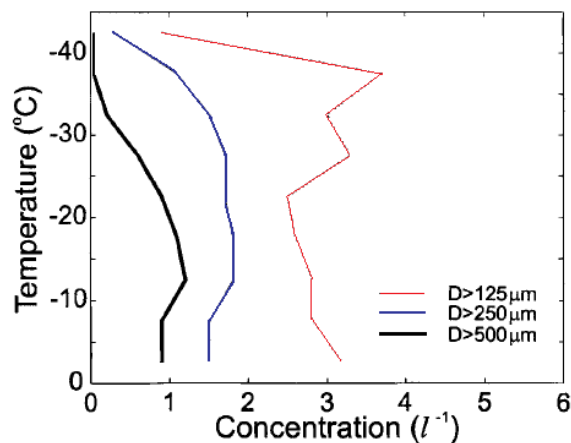
Knowing that ice phase occurrence in clouds is more probable with decreasing temperature, one would expect that ice crystal concentration would rise at low temperatures. However, very often when glaciation occurs, ice concentration does not depend much on further decrease in temperature. For a temperature range of -4 °C to -25 °C, the number concentration of ice particles reaches values of 10^4 per liter, and varies very little with the cloud top temperature (measured in clouds over the Cascade Mountains, Washington, Hobbs et. al. 1974b). In some cases, ice concentration does depend on cloud temperature, but the largest ice concentration appears at -12°C to -14°C instead at the lowest temperatures (Hobbs et. al. 1980). Fig. 2.6 represents particle size spectra obtained from snow storms at selected altitudes.
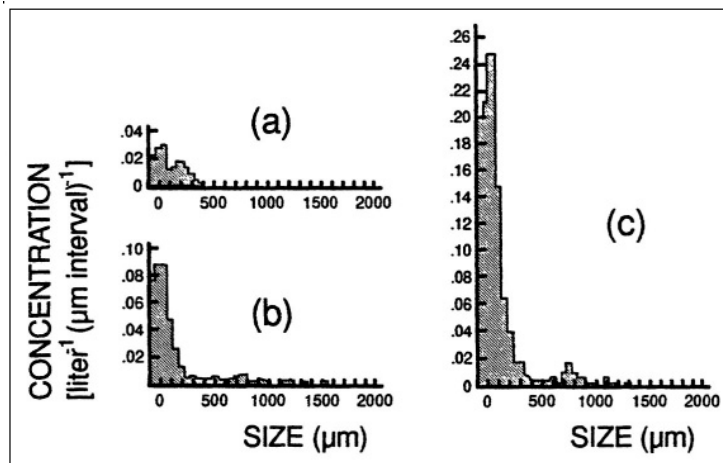
Figure 2.6: Snow crystal size spectra at selected altitudes, (a) at 6694 m to 6567 m, with temperatures-27.4to -26.5 °C, (b) at 5668 to 5504 m, with temperatures -22 to -19.9 °C, (c) at 5034 to 4898 m, with temperatures -16.7 to -15 °C. (Adapted from Rauber 1987b)

Maximum concentration occurs for particles smaller than 1 mm, and it decreases rapidly toward the large size at the end of the spectrum. Changes of ice crystal concentration with height for the same cloud as in figure 2.6, is given in Fig. 2.7.
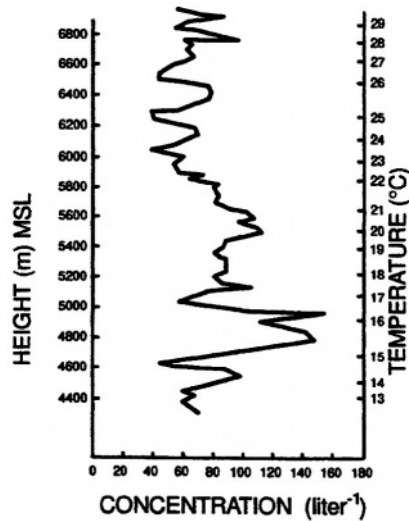
Figure 2.7: Variation of ice crystal concentration with height in snow storms over North Colorado. (Adapted from Rauber 1987)

2.2 Nucleation and secondary ice production

There are four basic modes for producing ice nuclei (IN): *deposition mode*, *condensation freezing mode*, *immersion mode* and *contact mode*. Ice initiation for each mode occurs at a specific temperature. Also, aerosols with variety of size and chemical characteristics can act as IN at one or possibly all of the four modes.

In the *deposition mode*, the environment needs to be supersaturated with respect to ice. Water vapor gets absorbed directly from the vapor phase onto the surface of the IN, which transforms into ice at sufficiently low temperatures. In the *condensation freezing mode*, an aerosol particle acts as a CCN to form a drop which freezes at some time during the condensation at temperatures below 0 °C. In the *immersion mode*, the IN immerses into a drop at temperatures above 0 °C, but freezes whenever the temperature of the drop becomes sufficiently low. In the *contact mode*, IN and cloud droplets come into contact, due to Brownian, thermophoretic and diffusiophoretic effects, Young (1974a,b). Brownian motion is a random-walk transport of aerosols due to collisions with

air molecules. Thermophoresis occurs due to attraction and repulsion of aerosols particles by a droplet along temperature gradients (Pruppacher and Klett 1997), whereas diffusiophoresis occurs along gradients of water vapor (Cotton *et al*. 1986).

There are numerous observations over the Cascade Mountains (Hobbs 1969; Hobbs *et al*. 1974b), over Japan (Isono 1965; Ono 1972; Magono and Lee 1973), in cumulus clouds over Australia and Tasmania (Mossop 1970, 1971, 1972; Mossop *et al.* 1967, 1968, 1970, 1972; Mossop and Ono 1969), and in cumulus clouds over Missouri (Braham 1964; Koenig 1963, 1965), showing that the concentration of ice particles may exceed the concentration of ice nuclei, which is determined at the cloud top temperature. The mechanism that explains these observations is called secondary ice production. Secondary ice production can occur in three ways: 1) mechanical fracturing of fragile crystals, 2) fragmentation of cloud drops during freezing, and 3) Hallett-Mossop (1974) multiplication of ice during riming.

The first mechanism is dominant at temperatures ranging from -12 °C to -14 °C, where fragile and delicate dendritic crystals form. Studies done by Hobbs (1969, 1972, 1974b), Hobbs and Farber (1972), Jiusto and Weickmann (1973), Vardiman (1974) and Vali (1980) show that the concentration of ice crystals can be significantly increased due to fracturing mechanism. Such enhanced ice concentrations are also supported by large amounts of ice crystal fragments collected in clouds and at the ground.

Observations from Japan (Ono 1972), Australia (Mossop 1970, 1972; Mossop *et al*. 1968, 1970, 1972), and Missouri (Koenig 1963; Braham 1964) suggested that increases in ice concentration can also be due to fragmentation of relatively large individual cloud drops (> 250 µm) during freezing. These findings show different ice

crystal concentration enhancement factors at various temperature ranges involving drop diameters from 50 µm to 240 µm, but the enhancement was finite and quite small.

The third secondary ice production mechanism occurs during riming of ice particles. Hallett and Mossop (1974), Mossop and Hallett (1974) and Mossop (1976) demonstrated that this process is very sensitive to and dependent on several factors: drop size distribution, liquid water content, the velocity of the drops impacting on a riming ice particle, the air temperature and the surface temperature of the riming ice particle. They found that significant ice splinter production occurs for liquid water contents of about 1 g m^{-3}, at a temperature range of -3 °C to -8 °C, drop diameters larger than 24 µm, and drop impact velocities between 1.4 and 3 m s^{-1}. One secondary ice splinter is produced per 100 to 250 drops of diameter larger than 24 µm, impacting the ice particle under optimal conditions, (Mossop 1985a,b,c, 1976; Hallett and Mossop 1974; Mossop and Hallett 1974). Mossop (1985a,b,c) and Heymsfield and Mossop (1984) showed that the surface temperature of the riming ice particle is more important than air temperature and it needs to be near -5 °C. The rate of secondary ice production depends also on the presence of droplets with diameters less than 13 µm that cover a riming ice crystal, (Mossop 1978). Secondary ice particles appeared as small columnar crystals. The sequence of events during this process is captured on motion picture film by Choularton *et al*. (1980). Consider a riming ice particle covered by droplets of diameter less than 13 µm at a temperature below -8 °C. If a supercooled drop lands on surface of the riming ice crystal, it freezes symmetrically, creating an ice shell around the drop. Then, as the interior of the drop starts freezing, ice shell breaks and produces an ice spike, which fractures. At temperatures below -8 °C, ice growth inward dominates the ice shell formation and there

14

is no ice spike formation. On the other hand, at temperatures higher than -3 °C, ice shell formation is not possible, because a drop landing on an ice crystal spreads over the crystal before it freezes.

2.3 Ice growth processes

An explanation about growth of crystals by vapor diffusion, accretion of supercooled drops (riming), and aggregation are given in the following subsections.

2.3.1. Deposition

Deposition is the process by which ice particles grow by diffusion of water vapor. There are three possible scenarios that can occur during depositional growth and they depend on a proportion between vapor pressure (e), vapor pressure over liquid water (e_s) and over ice (e_i). These scenarios are described schematically in Fig 2.8 (Korolev 2007). In case (1) where $e > e_s > e_i$, both droplets and ice crystals grow simultaneously as long as the condition is satisfied. Vertical velocity, which provides simultaneous growth within mixed-phase clouds ranges from a few cm s^{-1} to a few m s^{-1}, Korolev (2007). In case (2) where $e_s > e > e_i$, droplets evaporate and ice particles grow. In air saturated with respect to ice, but subsaturated with respect to water supercooled liquid droplets and ice crystals cannot co-exist in equilibrium.
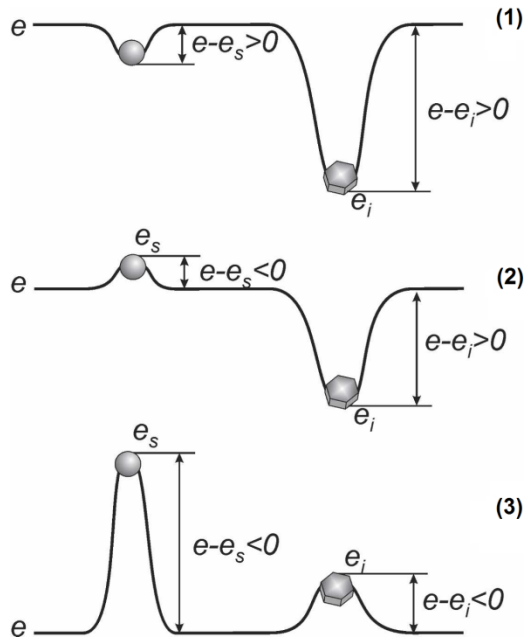
Figure 2.8: Schematic diagram of possible proportions between e, e_s and e_i in a mixed-phase cloud. Liquid droplets and ice crystals are embedded in water vapor pressure, e. In condition: (1) both droplets and ice particle grow, (2) droplets evaporate and ice particles grow, WBF process, (3) both droplets and ice crystals evaporate. (Adapted from Korolev 2007)

Thus, when water vapor evaporates from the drops and deposit on crystals as showed in Fig. 2.9. This precipitation mechanism was first described by Wegener (1911), Bergeron (1935), Findeisen (1938), and is therefore named accordingly (WBF process). The result of WBF is glaciation of a mixed-phased cloud and it can occur in both updrafts and downdrafts (Korolev 2007).

16
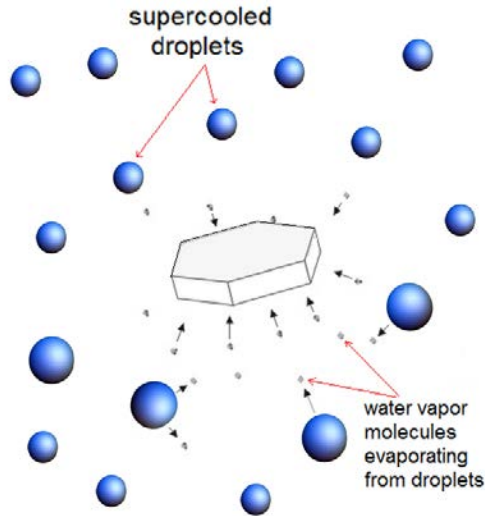
Figure 2.9: Schematic description of depositional growth of ice crystals by WBF process.

In case (3) where $e_s > e_i > e$, both droplets and ice crystals evaporate and it can occur in downdrafts, which exceed a few m s^{-1}. The most possible process that causes simultaneous evaporation of both droplets and ice crystals is entrainment and mixing with dry air near cloud boundaries.

The difference between supersaturation with respect to ice and water has maximum at -12 °C. However, the resulting mass growth rate (dm/dt) occurs at lower temperature (near -15 °C), because local heating from latent heat release causes the vapor pressure difference between ice crystal surface and its environment to be reduced slightly. Growth of crystals by deposition is common in stratus clouds with low supersaturation and very weak updrafts. Ice particles that have grown by this mechanism are called *ice crystals* or *snow crystals*. Some examples of the type of crystals that grow by deposition are given in Fig. 2.10.
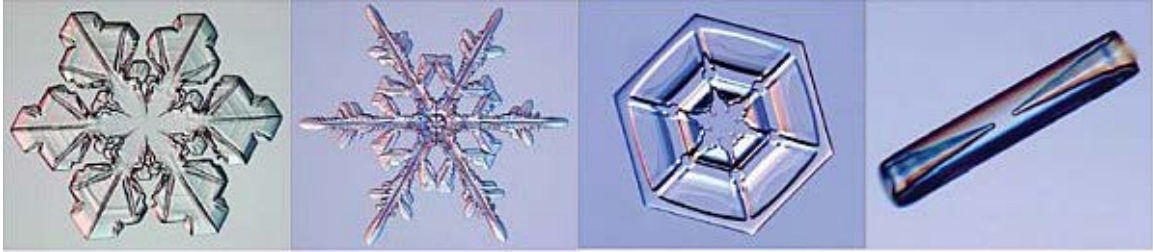
Figure 2.10: Examples of ice crystals that grown by deposition (stellar crystal with plates at ends; ordinary dendritic crystal; hexagonal plate; hollow column).

2.3.2. Accretion

Accretion or riming is a process of collecting of supercooled droplets by crystals (Fig 2.11). Droplets that are involved in riming process have diameters ranging from 10 to 80 µm, whereas drops with diameters larger than 80 µm are generally absent (Pruppacher and Klett 1997). The collision efficiency is higher for larger sizes of the collecting crystal due to a larger effective sweepout area. If the collector crystal is smaller than a critical size, the collection efficiency drops to zero. This means that a crystal needs to have a certain size before riming can occur (Ono 1969; Hobbs et al. 1971a; Kikuchi 1972a; Iwai 1973). The critical size (diameter) for hexagonal plate is about 110 µm, and about 200 µm for crystal with broad branches (Wang and Ji 1992). Columnar crystals need to grow by deposition until they reach critical width of about 35 µm (Ji 1991).
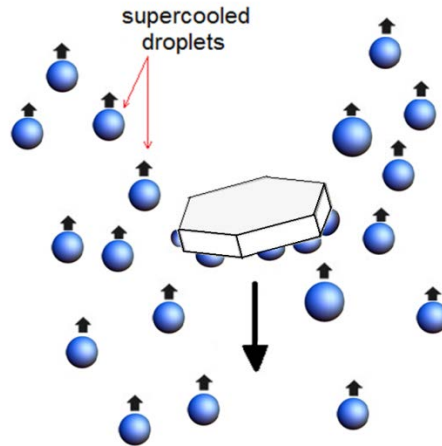
Figure 2.11: Schematic description of riming (an ice crystal collecting droplets as it falls).

In the initial stages of riming, as long as the original habit of ice crystal is still clearly distinguishable, the ice particle is simply called a lightly or densely *rimed snow crystal* (Fig. 2.12). When the features of the primary ice particle are no longer visible, the ice particle is called a *graupel particle,* a *soft hail particle,* or a *snow pellet.* Such a particle has a white, opaque, and fluffy appearance due to the presence of a large number of air capillaries in the ice structure, and usually bulk density is less than 0.8 g cm^{-3} (List 1958a,b).
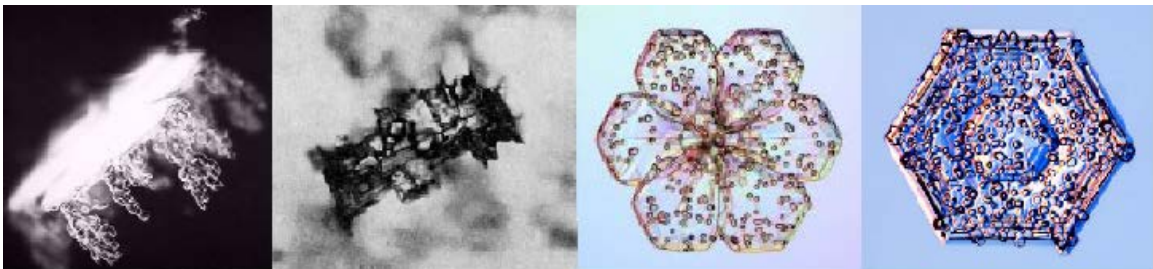
Figure 2.12: Examples of rimed ice crystals (rimed crystal with broad branches; rimed column; rimed crystal with sector-like branches; rimed hexagonal plate).

2.3.3. Aggregation

Aggregation is the process of collision and coalescence of snow crystals producing clusters of ice crystals or snowflakes (snow aggregates). This growth process

is strongly dependent on temperature, as well as on the shape of the ice crystals. Observations show that snow crystals clump to each often in two ways. If the air temperature is relatively close to 0 °C, ice crystals "stick" to each other by forming an ice bond across the surface of contact (Hobbs *et al.* 1974b; Rogers 1974a,b). This mechanism is most efficient at temperatures close to 0 °C, when a quasi-liquid film covers the crystal's surface. The second way of forming snow aggregates is by an "interlocking mechanism" that occurs among crystals with dendritic features. Conditions that make this mechanism most efficient are temperatures ranging from -12 °C to -17 °C, and high ice supersaturations (Ohtake 1970b,c). Figure 2.13 represents snowflakes formed by aggregation.
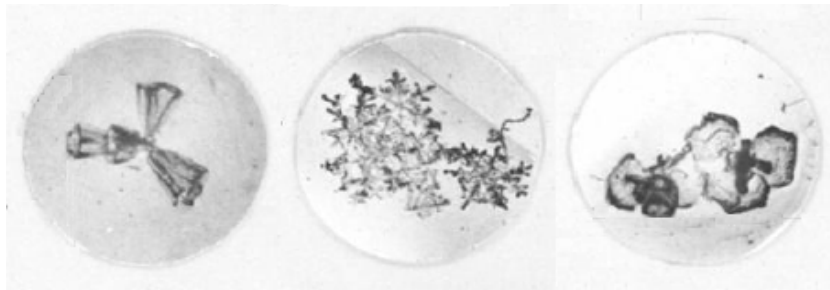
Figure 2.13: Examples of snow crystals produced by aggregation. (Adapted from Locatelli and Hobbs 1974).

From field observations of Hobbs et al. and of Jiusto and Weickmann (1973) we know that the most snowflakes are aggregate planar crystals with dendritic habit features. Aggregates of columns and needles tend to stay small, whereas aggregates of dendritic crystals tend to become large. Most of the snowflakes have diameters between 2 and 5 mm, but maximum diameters can reach 15 mm. Magono and Nakamura (1965), Matsuo and Sasyo (1981b) and Sasyo and Matsuo (1980) studied the density of snowflakes. The

most frequent values of snow flakes densities were between 0.01 and 0.2 g cm^{-3}, but typical values were ranging from 0.005 to 0.5 g cm^{-3}.

2.4 Observed ice crystals characteristics

The evolution of a particle size distribution depends on advection (air motion and particle fallspeed), the dominant growth particle process (deposition, aggregation, accretion), and production of new ice particles. Plots of vertical variation of intercept parameter N_0, versus slope parameter Λ, (spectral trajectory) obtained by aircraft flights during winter, show the effect of a growth process on particle size distribution (Lo and Passarelli 1982). During depositional growth, N_0 increases and Λ decreases slowly, suggesting the increase in concentration is due to the growth of small particles into detectable sizes. Large particles grow faster than small particles, thus slope of the distribution is decreased. In this stage deposition is dominant since particles are small and collisions are rare. This stage is characterized as stage one of the ice crystals growth process given in Fig. 2.14.
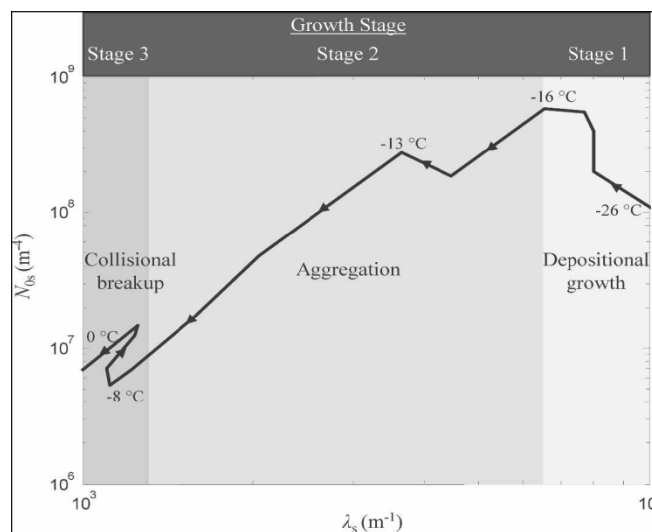
Figure 2.14: The vertical variation of N_o versus Λ (i.e. spectral trajectory) obtained by aircraft observations. (Woods et al. 2007)

The second stage of growth is characterized by aggregation, where both parameters decrease due to the depletion of small particles which go into creating the large ones. The transition from deposition to aggregation is very sudden and occurs around -15 ºC, which is the dendritic growth temperature regime. The third stage is characterized by increase of both parameters indicating an increase in the number of small particles and a decrease in the number of large particles. This means that depletion of small particles is balanced by the secondary ice production mechanism and that large particles (aggregates) are somehow depleted. Lo and Passarelli (1982) suggested collisional breakup as a secondary ice production mechanism.

Woods *et al*. (2008) analyzed snow particle size spectra collected during aircraft observations (in the Pacific Northwest) at variety of altitudes and temperatures in winter frontal and orographic precipitation systems. They examined the size spectral parameters (intercept and slope parameters) as a function of temperature, particle habit and storm environment. In general, the particle size distribution agrees with an exponential size distribution. Size spectra parameters for nonfrontal environments result in a greater range of values compared to frontal environments, due to the more complex microphysical processes in terrain-induced lifting of air. Woods *et al*. (2008) observed a tendency for higher concentrations of small particles and lower concentrations of large particles in nonfrontal orographic situations. Analysis of size distribution parameters as a function of temperature showed that both parameters decrease with warming temperatures. However, the decrease is most significant in temperatures ranging from -30 ºC to -10 ºC, due to the effects of aggregation. At temperatures above -10 °C, values of slope and intercept

parameters are higher, so the temperature dependence is smaller. From their trajectory analysis, they have concluded that Hallet-Mossop multiplication is responsible for secondary ice production. Their conclusions are based on observed elevated concentration of droplets greater then 24µm, as well as appearance of needle and column habit types at temperatures warmer than -10 ℃.

3. Radar polarimetric variables

A description of polarimetric variables used in this study and their physical meaning is given in this section. These variables include: reflectivity factor at horizontal polarization Z_H, differential reflectivity Z_{DR}, cross-correlation coefficient ρ_{hv}, and specific differential phase K_{DP}. To decrease noise influence on estimations of Z_{DR} and ρ_{hv}, the one-lag estimators are used (Melnikov and Zrnic 2004).

Typical values and characteristics of these variables will be given mostly in terms of winter weather precipitation. The physical meaning of Z_{DR} and ρ_{hv} at lag one is the same as for zero-lag estimators (conventional), so an explanation will be given for conventional estimators. All polarimetric values presented are for S-band radars, unless stated differently. Material used in this section is from Matthew Kumjian's thesis (2008), lecture notes from Alexander Ryzhkov, and Melnikov and Zrnic (2004).

3.1 One-lag estimators

As a result of low signal to noise ratio (SNR) observed in distant precipitation, light rain, weak clouds and snow, Z_{DR} and ρ_{hv} estimates can be biased by noise. Desirable

accuracies for Z_{DR} and ρ_{hv} needed to distinguish between water droplets, snowflakes or crystals are about 0.1 dB and 0.01, respectively. With the focus on errors occurring at SNR intervals of 2 to 15 dB, accuracy of Z_{DR} and ρ_{hv} measurements depends on uncertainty of the noise levels used in the estimator. In the WSR-88D radars, noise is measured at high antenna elevation in the absence of precipitation before each volume scan. Then, radar moments are calculated using the measured noise. The uncertainties in the noise due to imperfections of radar devices, and noise from clouds and the ground, produce errors in the estimators. To avoid these errors, the one-lag estimators Z_{DR1} and ρ_{hv1}, which are not biased by noise, can be used instead of conventional ones. The estimators at lag one are given as (Melnikov and Zrnić 2006):

$$Z_{DR1} = 10\log_{10}\frac{\left|R_h(T)\right|}{\left|R_v(T)\right|} \qquad (3.1)$$

$$\rho_{hv1} = \frac{\left|R_{hv1}(T)\right| + \left|R_{hv2}(T)\right|}{2\left|R_h(T)R_v(T)\right|^{1/2}} \qquad (3.2)$$

where R_h and R_v are the correlation functions, R_{hv1} and R_{hv2} are the correlation functions for voltages in the horizontal and vertical channels at lag T (the pulse repetition interval).

3.2. Reflectivity factor

The reflectivity factor at horizontal polarization, expressed in mm^6 m^{-3}, is:

$$Z_h = \int D_e^6 N(D)\,dD \qquad (3.3)$$

where D_e is equivalent spherical diameter, and $N(D)$ is the concentration of particles as a function of diameter. For convenience the reflectivity factor, Z_H is expressed in logarithmic units (dBZ) as:

$$Z_H = 10\log_{10}\left(\frac{Z_h}{1\,mm^6 m^{-3}}\right) \qquad (3.4)$$

Z_H is strongly dependent on particle size and concentration. This equation assumes spherical, horizontally oriented liquid particles that obey the Rayleigh scattering approximation. A few large particles in the sampling volume can produce the same Z_H as the sampling volume filled with thousands of small particles. Z_H alone can not provide insight into cloud microphysical properties. Typical values of the reflectivity factor of snow particles are given in Table 3.1.

Table 3.1: Typical values of reflectivity factor Z_H, differential reflectivity Z_{DR}, cross correlation coefficient ρ_{hv}, and specific differential phase K_{DP} for snow.

	Ice crystals	Dry aggregated snow	Wet aggregated snow
Z_H (dBZ)	< 30	< 35	< 55
Z_{DR} (dB)	< 4	0.0 to 0.3	0.5 to 2.5
ρ_{hv}	0.98 to 1.0	0.97 to 1.0	0.90 to 0.97
K_{DP} (deg/km)	- 0.5 to 0.5	0.0 to 0.05	0.0 to 0.5

3.3. Differential reflectivity

The ratio of the reflectivity factor at horizontal and vertical polarizations, or differential reflectivity, first proposed by Seliga and Bringi (1976), is given as:

$$Z_{DR} = \log_{10}\left(\frac{Z_{hh}}{Z_{vv}}\right) \qquad (3.5)$$

Since Z_H is affected by large hydrometeors, Z_{DR} will be affected too. Differential reflectivity depends on size, shape, orientation, density and phase composition of hydrometeors. However, it is independent of concentration of the hydrometeors. Z_{DR} is positive in rain, and presence of ice hydrometeors decrease Z_{DR} since dielectric constant

of ice is much lower than dielectric constant of water. Thus, Z_{DR} of dry snow is generally lower than Z_{DR} of rain, but there are cases where Z_{DR} of rain can reach 4 dB or higher. Z_{DR} for snow depends on aspect ratio, density and orientation of dry snowflakes. For spherical or randomly oriented crystals, Z_{DR} is equal to 0 dB. However, Z_{DR} will increase with increasing oblateness, density or water fraction. Snow particles with pronounced nonspherical shape, high density and preferably horizontal orientation produce high Z_{DR} (> 4 dB). On the other hand, snow aggregates are larger but they have very low density and more spherical shape, so they will produce much smaller Z_{DR}. A dependence of differential reflectivity on the density of snow crystals is given in Fig 3.1, and some typical values are given in Table. 3.1.
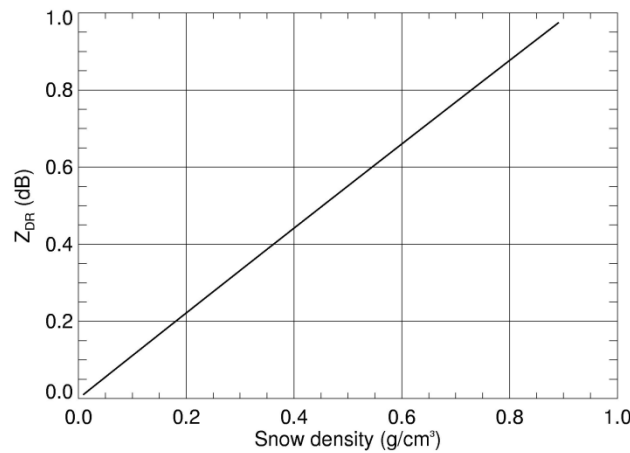
Fig. 3.1: Z_{DR} as a function of snow particle density. Courtesy of Alexander Ryzhkov

3.4. Cross correlation coefficient

The cross-correlation coefficient at zero lag is a measure of the correlation between the backscattered horizontal and vertical polarized signals from each scatterer within a sampling volume, and it is defined as (Doviak and Zrinć 2006):

$$\rho_{hv}(0) = \frac{\left\langle S_{vv}S_{hh}^{*}\right\rangle}{\left[\left\langle \left|S_{hh}\right|^{2}\right\rangle^{1/2}\left\langle \left|S_{vv}\right|^{2}\right\rangle^{1/2}\right]}$$

(3.6)

where $\left\langle S_{vv}S_{hh}^{*}\right\rangle$ is a complex element from the backscattering covariance matrix (off-diagonal quantity), and $\left\langle \left|S_{vv}\right|^{2}\right\rangle$ and $\left\langle \left|S_{hh}\right|^{2}\right\rangle$ are real elements (diagonal quantities). ρ_{hv} is affected by diversity of shapes, sizes, orientations and phase composition within a sampling volume. In rain ρ_{hv} is very close to unity, although sometimes it decreases (not below 0.98) due to diversity in orientation and shape of raindrops. For spherical particles of any size ρ_{hv} is equal to unity, but it will decrease with increasing diversity in oblateness, randomness in orientations and water content. In melting snow (or hail) ρ_{hv} decreases noticeably because of mixture of water and ice. ρ_{hv} also decreases if particles change their shape due to collisions or breakup or due to increased growth rate. ρ_{hv} is very sensitive to resonance effects. At S band, resonance effects are important for liquid particles larger than 6 mm. Resonance-sized particles (melting snow) will cause ρ_{hv} to decrease. At S band radar, the lowest values of ρ_{hv} (0.5 to 0.8, for insects and birds, 0.3 to 0.6 for sea surface) are produced by nonmeteorological scatterers, while for meteorological scatterers ρ_{hv} remains above 0.80. Typical values of ρ_{hv} for snow particles are given in Table. 3.1.

3.5. Specific differential phase

The specific differential phase (K_{DP}), given in deg km^{-1}, is the range derivative of differential phase (Φ_{DP}) defined as:

$$K_{DP} = \frac{1}{2}\frac{d\Phi_{DP}}{dr} = \frac{180\lambda}{\pi}\int_0^\infty \mathrm{Re}\left[f_H^F(D) - f_V^F(D)\right]N(D)dD$$

(3.7)

where $f_{H,V}^F$ is the forward scattering amplitude at horizontal and vertical polarization, and λ is the radar wavelength. At Rayleigh approximation, the forward scattering amplitude is identical to the backscattering amplitude. Differential phase shift Φ_{DP}, represents a shift in phase between the horizontal and vertical waves along the radial. Φ_{DP} is independent of attenuation affects, radar miscalibration, noise bias, and partial beam blockage (Zrnić and Ryzhkov 1999). Φ_{DP} is a much more responsive to liquid than ice particles, because it depends on the dielectric constant of the medium, which is a function of phase composition. K_{DP} is positive in regions with rain, but in regions with aggregated or spherical ice, values are close to zero. In winter storms in Oklahoma, K_{DP} as low as 0.08 ° km^{-1} was observed (Zrnić and Ryzhkov 1999). However, enhanced K_{DP} could be found in regions with high-density pristine crystals, and with preferably horizontal orientation. Negative K_{DP} is produced by vertically oriented crystals, which can be aligned by strong electric fields inside clouds. The biggest disadvantage of K_{DP} measurements is that it is small in dry snow and very noisy. Typical values of K_{DP} at S band for snow are given in Table. 3.1.

3.1 Brief review of related studies

Bader *et al.* (1987) investigated the relationship between ice phase microphysical structure of a stratiform cloud and differential reflectivity using simultaneous aircraft and dual polarization radar observations. They used only a single set of observation obtained during May in stratiform cloud that produced light precipitation. Particle characteristics

reflect sorting by size and type, associated with growth regimes and weak wind shear within the fallstreak. Z_{DR} of 3 to 4 dB observed at the cloud top was associated with large dendritic crystals. Regions of enhanced Z_{DR} at approximately 3 km AGL (with average temperature of –7 °C), were associated with planar crystals (plates and stellar dendrites). The effects of sorting by wind shear were most pronounced at lowest level at 1.9 km, with temperature of -2 °C.

Evans and Vivekanandan (1990) developed multi-parameter radar (for S, X, C and Ka-band) and polarized microwave radiative transfer models for different ice crystal habits. The discrete dipole approximation was used, where particle is completely divided into a number of cubes (the discrete dipoles) with sizes much smaller than the wavelength. Using this method they calculated electromagnetic scattering properties of horizontally oriented needless, columns and hexagonal plates, columns and needles were assumed to be randomly oriented in horizontal. Sizes from 0.06 to 2 mm and particle bulk density of 0.92 and 0.23 g cm^{-3} were studied. The model computations show that for a give ice water content (0.1 g m^{-3} was used herein) radar variables (Z_H, Z_{DR}, K_{DP}, and linear depolarization ratio, LDR) can be used to distinguish between columns, needles and plates to a certain extent. Evans and Vivekanandan (1990) showed that for a given ice crystal habit Z_{DR} can be used as an average measure of particle density. Z_H along with K_{DP} can be used to isolate oriented from randomly oriented crystals, since K_{DP} is sensitive only to oriented particles and Z_H is sensitive to both. LDR can distinguish between randomly oriented prolate particles (columnar crystals) and oblate particles (plates).

Matrosov et al. (1996) suggested that elevation angle dependencies of radar depolarization ratios can be used to distinguish between plate-like, columnar crystals, and aggregates within stratiform clouds. As obtained from model calculations, plate-like and columnar crystals as well as aggregates, with random orientation in horizontal plane, have distinctly different variation of depolarization ratio. Using observations made with K_a-band radar (8.6 mm wavelength) with elliptical polarization, they obtained measurements that are in good agreement with theoretical calculations.

Hogan *et al.* (2002) investigated microphysical characteristics of warm-frontal mixed phased cloud, using simultaneous aircraft and S-band radar polarimetric measurements. They investigated stratiform cloud containing embedded convective regions, identified by the radar as narrow convective turrets. These turrets contained concentration of small crystals (near 2500 l^{-1}, two orders of magnitude larger than ambient values) along with supercooled liquid droplets (including droplets with diameter around 25 µm), and narrow updrafts of 1 to 2 m s^{-1}. Embedded convection regions had high Z_H and low Z_{DR}, suggesting nearly spherical particles that were either large in size or had high density. Immediately above the observed high Z_H region, at level of -6.1 °C temperature, there was a maximum of ice concentration measured by the aircraft. At the same level of temperature -6.1 °C, at the base of high Z_{DR} (up to 4 dB) aircraft sampling showed presence of pristine columns growing in the weak updraft (around 0.4 m s^{-1}) by deposition. Hogan et al. explained this by Hallett–Mossopp ice multiplication that was occurring during riming process and producing ice splinters, which than continue to grow by deposition producing the high Z_{DR}.

Plummer *et al.* (2010) used simultaneous S-band radar polarimetric measurements along with in situ aircraft measurements with the motivation to develop quantitative criteria for identification of potential in-flight icing conditions in clouds. They used measurements of supercooled liquid water (SLW) and ice particles within orographic cloud systems with widespread stratiform precipitation that contained embedded convection. They utilized the Z_H, Z_{DR}, K_{DP}, and their statistical difference between measurements of supercooled liquid water and ice. Plummer et al. developed an algorithm that matches radar with aircraft data in time and space along with probabilistic criteria that as a result gives probability distribution of the likelihood of SLW's presence as a function of polarization variables.

Kennedy and Rutledge (2011) used K_{DP} measurements made with S-band radar during winter storms in northeastern Colorado. They observed local maxima in K_{DP} in range of ~0.15 to 0.4° km^{-1} at the level of -15 °C. For particle growth calculation, they considered only depositional growth, in continuously water-saturation conditions. Also, they considered pristine dendrites and aggregates modeled as oblate spheroids. Based on their calculations, with microwave scattering model, oblate ice particles with moderate bulk densities and diameters in the range of ~0.8 to 1.2 mm can generate K_{DP} that matches with the observed one. They suggested that localized regions of K_{DP} within a range of near 0.1 to 0.2° km^{-1} in winter storms can be used for identification of regions with active dendritic growth.

4. Observed radar polarimetric data

At the beginning of this chapter, the 27 January 2009 winter storm and related weather conditions are presented. During this event, a polarimetric signature that reveals ice crystal habit and possibly a type of growth process is observed in subfreezing levels at a height of approximately 4.5 km above ground, and 2.5 km above the melting layer. This signature can be very useful for understanding the influence supercooled droplets have on radar polarimetry. It identifies the regions within the subfreezing part of cloud where only glaciation is occurring. Knowing the actual nature of the observed signature is valuable additional information for in-flight icing detection.

4.1 Synoptic situation for 27 January 2009

An upper-level trough, with an intense jet stream (over 62 m s^{-1}) crossing over Oklahoma provided favorable dynamical conditions for convective-type mixed winter precipitation. A cold front moved across Oklahoma the previous day, so this was a post-frontal situation with the cloud system moving from the northeast. Through the morning hours on 27 January 2009, ahead of the positively tilted trough, gradually increasing isentropic ascent combined with weak instability aloft was supporting an increase of convectively enhanced winter precipitation rates across much of Oklahoma. Across the southwest/central to northeast-east/central Oklahoma, sleet was prevalent, due to cold advection at low levels. During the afternoon, from southeast Oklahoma to further east, isentropic ascent coincident with a surface baroclinic zone maintained enhanced precipitation rates. During the late afternoon, northerly surface winds behind the cold

front continued to advect a subfreezing, low-level airmass over eastern Oklahoma, which resulted in a transition from freezing rain to mainly sleet mixed with snow.

During this event up to 7.6 cm (3 inches) of sleet fell in central Oklahoma, and nearly 5.1 cm (2 inches) of ice accumulations were reported on power lines in east-central Oklahoma. These accumulations resulted in more than 50,000 electrical utility customers losing power in Oklahoma from downed power lines. Furthermore, the Oklahoma monthly climate summary for January 2009 (Oklahoma Climatological Survey) explained that traveling across much of the state was discouraged.

Fig. 4.1 shows the vertical profile of the atmosphere at 0000 UTC 28 January in Norman, Oklahoma. Cloud top height was at approximately 7.3 km, and the temperature at that level was -26 ℃. There were two 0 ℃ levels, located close to each other. The upper one was at ~2.2 km and lower at ~1.4 km. Subfreezing temperatures in the lowest portion of the troposphere (below 1.4 km) and a layer of warmer air (with temperature slightly above 0 ℃) above and below the freezing level caused sleet and freezing rain in some areas. Relative humidity with respect to water ranged from 80% (at ~5 km) to 100% (at ~3 km), indicating that the atmosphere was supersaturated with respect to ice throughout most of the observed cloud. Also, there was very strong wind shear (31 m s^{-1} in the layer from surface to 4 km AGL).
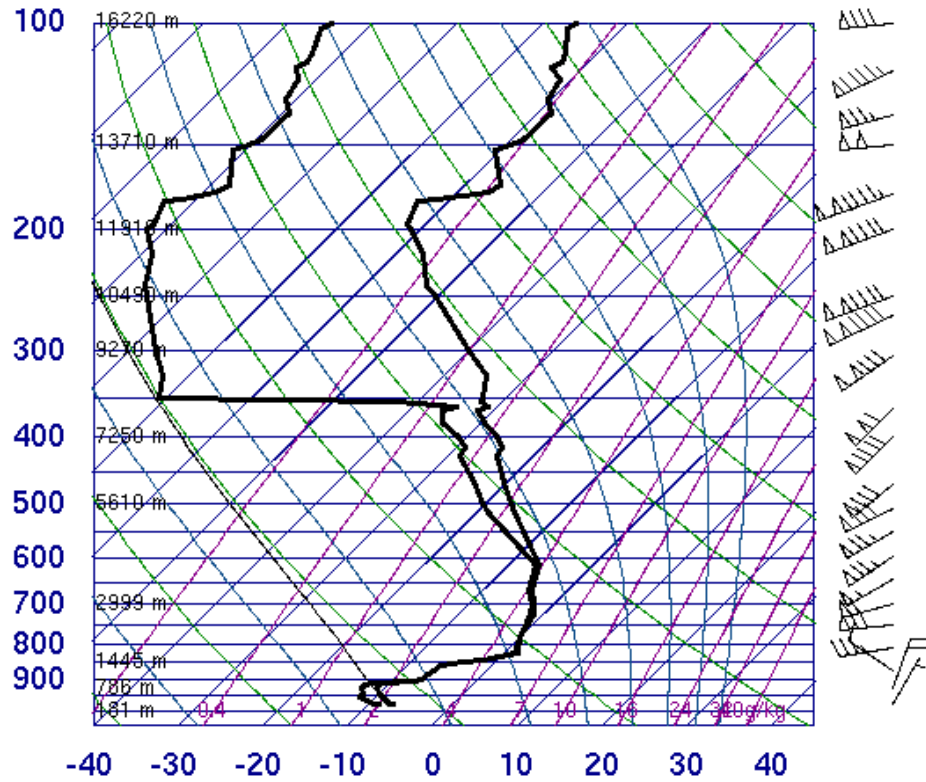
Figure 4.1: Sounding from Norman, Oklahoma at 0000 UTC January 28 2009.

Fig. 4.2 represents the reflectivity factor of this event at 2317 UTC observed with the operational National Weather Service WSR-88D radar in Oklahoma City, KTLX. The stratiform cloud covers the whole east, south and southeast parts of Oklahoma, with maximum reflectivity of 35 dBZ. The black line in Fig. 4.2 indicates the azimuth of 181° at which a vertical cross section was made with the KOUN radar, at the same time. The temperature at 1.5 m was about -7 °C in the region under consideration.
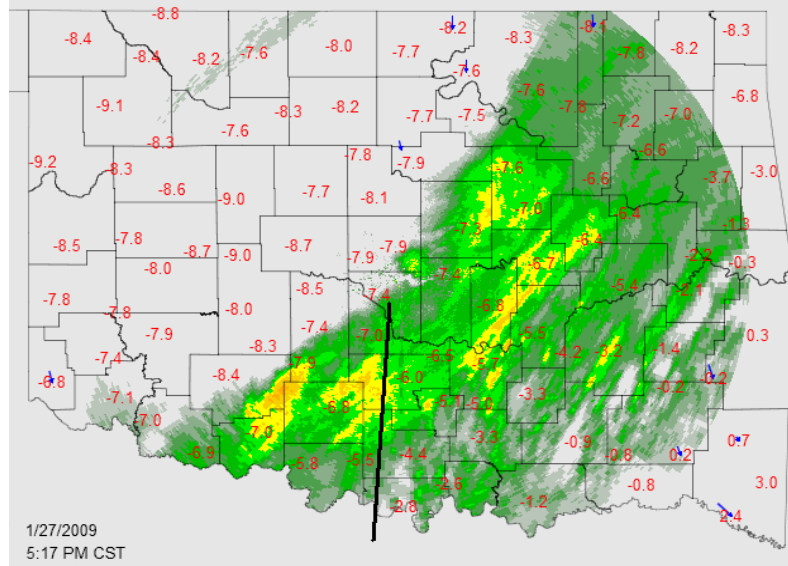
Figure 4.2: Base reflectivity (0.5° elevation angle) observed with KTLX operational radar at 2317 UTC on January 27, 2009. Black line indicates azimuth of 181°. Red numbers represent temperatures at 1.5 m, in °C.

4.2 Radar observations

To enhance quantitative measurements of polarimetric parameters in clouds, the following data collection and signal processing procedures were used:

1) Longer dwell times (i.e., 128 samples spaced 781 µs apart; about three times what is typically used by the NWS) to improve accuracy of measurements,

2) Smaller elevation increments (i.e., 0.25^o instead of 1°) to improve resolution and the number of measurements in the vertical,

3) Twice the range sampling rate (by oversampling), also to improve resolution and accuracy, and

4) Correlation estimators for polarimetric variables to lessen noise effects (Melnikov and Zrnic 2007).

These procedures improve the accuracy and resolution of the data. Cloud data have been collected at elevations angles up to 60°, the limit in elevation for the WSR-88D. At the pulse repetition frequency (PRF) of 1280 Hz, 24 s is needed to complete one

RHI when utilizing procedures 1) - 4) above. The standard deviation (i.e., SD[$\hat{Z}$ (dBZ)]) of the reflectivity factor estimate for a radar resolution volume (i.e., 1^ox0.25 km) is

$$SD(\hat{Z}) = 4.34 / (M^{1/2} SNR)[1 + 2SNR + SNR^2 / (2\sigma_{vn}\pi^{1/2})]^{1/2} \text{ (dBZ)},$$

where $\sigma_{vn} = \sigma_v/(2v_a)$, σ_v is the spectrum width, and v_a is the unambiguous velocity (Doviak and Zrnić 2006; section 6.3.1.2). The *SNR* values in the case under consideration are from 10 to 20 dB so the standard deviation is determined by the third addend in the above formula. The spectrum width values in the analyzed areas are from 1 to 3 m s^{-1}. For a *SNR* = 10 dB, σ_v=1 m s^{-1}, PRF = 1280 Hz, and *M* = 768, (i.e., 128 time samples, multiplied by the 4 angular and 1.5 range samples), we obtain SD($\hat{Z}$) = 0.7 dBZ. For σ_v= 3 m s^{-1}, SD($\hat{Z}$) = 0.4 dBZ. So accuracy of our reflectivity measurements is better than the usual accuracy for operational observations with the WSR-88D, i.e., 1.5 to 2.5 dB.

4.2.1 Data presentations in PPI and RHI displays

Radar observations are made with KOUN, the dual-polarization S-band radar located in Norman, Oklahoma. The WSR-88D KOUN research radar employs a polarimetric mode with simultaneous transmission and reception of horizontally and vertically polarized waves. Radar data herein are presented as genuine vertical cross-sections or Range Height Indicator (RHI) and vertical profiles of Z_H, Z_V, Z_{DR} and ρ_{hv} at chosen distances from the radar. Also, Plan Position Indicator (PPI) for all four variables, generated from volumetric scans is presented.

Fig. 4.3 represents the 6.2° elevation PPI of Z_H, Z_{DR}, ρ_{hv} and K_{DP}, generated from volumetric scan at 2323 UTC 27 January, 2009. This elevation has an approximate altitude of 5 km altitude at 50 km distance from the radar, where the enhanced Z_{DR} was

observed (Fig. 4.3). At this elevation, the half-ring of enhanced Z_H and Z_{DR} at ~ 15 km range from the radar signifies the melting layer. Notice areas of enhanced Z_{DR} values from 1.4 (dark red) to 2.5 (purple), that coincides with a drop in ρ_{hv} to approximately 0.97 (in red and orange colors). Z_H does not provide any significant information, whereas K_{DP} is very noisy but still identifies areas with 0.4 deg km^{-1} (purple).
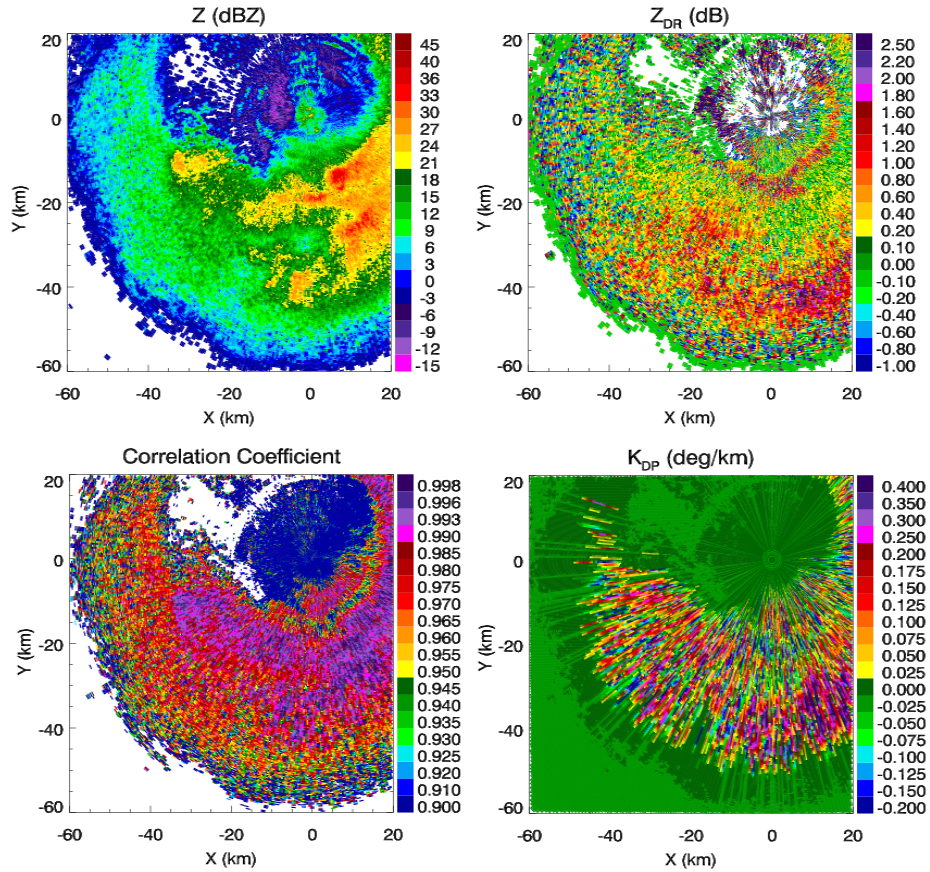
Fig 4.3: A 6.2° PPI of Z_H, Z_{DR}, ρ_{hv} and K_{DP}, generated from volumetric scan obtained by KOUN radar on 27 January, 2009 at 2323 UTC.

RHIs of Z_H, Z_{DR}, ρ_{hv} and K_{DP} obtained at 2254 (azimuth 181°) and at 2317 UTC (azimuth 189°) on 27 January 2009, are given in Fig. 4.4 and Fig. 4.5. Values of Z_H about 40 dBZ at height of approximately 1.5 km indicate the melting layer in Fig 4.4. The same type of signature is present in all given variables: Z_{DR} is between 1.5 and 2 dB, and ρ_{hv} decreases to 0.95. The melting layer signature is less obvious in K_{DP}.

In Fig. 4.5, the signature indicating the melting level is more pronounced, with Z_H values around 45 dBZ. There is also an enhanced Z_{DR} (~ 1.1 dB) signature at height of approximately 500 m, which is related to refreezing of particles (observed temperature was -11 °C). Though these features are interesting, the focus of this study is on the Z_{DR} signature observed at heights of approximately 4.5 and 5 km. So, all further discussion will be related to this elevated signature. The enhanced Z_{DR} occurs in temperature range from -10 °C to -15 °C. In Fig 4.4 enhanced Z_{DR} appears as a layer, whereas in Fig. 4.6 there are also "pockets" of enhanced Z_{DR}. In these pockets of enhanced Z_{DR} values reach 2.5 dB at nearly 5 km altitude, coincident with ρ_{hv} values of about 0.95 (Fig. 4.5). K_{DP} measurements are better in this case, with noticeable regions of enhanced values (up to 0.4 deg km^{-1} in red) that coincide with the areas of enhanced Z_{DR}. The "pockets" of enhanced Z_{DR} are present at approximately same altitude as in previous RHI (Fig. 4.4).

This signature is a consequence of different conditions that occur at the observed level, compared to the rest of the cloud. Since this event was convectively enhanced, observed "pockets" and layers indicate regions of embedded convection that is very common in stratiform clouds. However, the three-dimensional nature and evolution of these regions is not well known because of the lack of in-situ observations. Embedded convection represents very localized regions with vertical velocities (1 to 2 m s^{-1}) sufficient to maintain high supersaturations. Therefore these regions are favorable for rapid ice crystal growth by deposition in certain conditions (Korolev 2007), but also for growth by riming. If these conditions (presence of supercooled droplets with 25 µm diameter and temperature range of -3 ºC to -8 ºC) are satisfied, the Hallett-Mossopp multiplication of ice crystals can occur (Hogan et al. 2002). As already stated in section

two, this is the most efficient mechanism of secondary ice production that can significantly affect the initial concentration of ice crystals within the cloud. Fig. 4.6 is a display of vertical velocity measured from the vertically pointing beam of the Purcell wind profiler. Radial velocity is a measure of the amount of Doppler shift in the atmospheric signal returns. In this case, particles moving upward produce a positive Doppler shift and they are marked with yellow and red colors, whereas particles moving downward produce a negative Doppler shift, and are marked with cyan and blue colors. Data are obtained at 6-min intervals, from 1906 UTC until 0100 UTC 28 January 2009. Regions of enhanced updraft velocities close to 3 m s^{-1} are present in several locations (areas at about 6 km, marked with arrows and area at about 4 km marked with a circle) around the time our data was collected. The time of our radar observations matches with the time of weak updraft regions observed with wind profiler. It is possible that regions like these had caused different conditions, compared to the rest of the cloud and induced the microphysical processes that lead to the enhanced Z_{DR} signature.
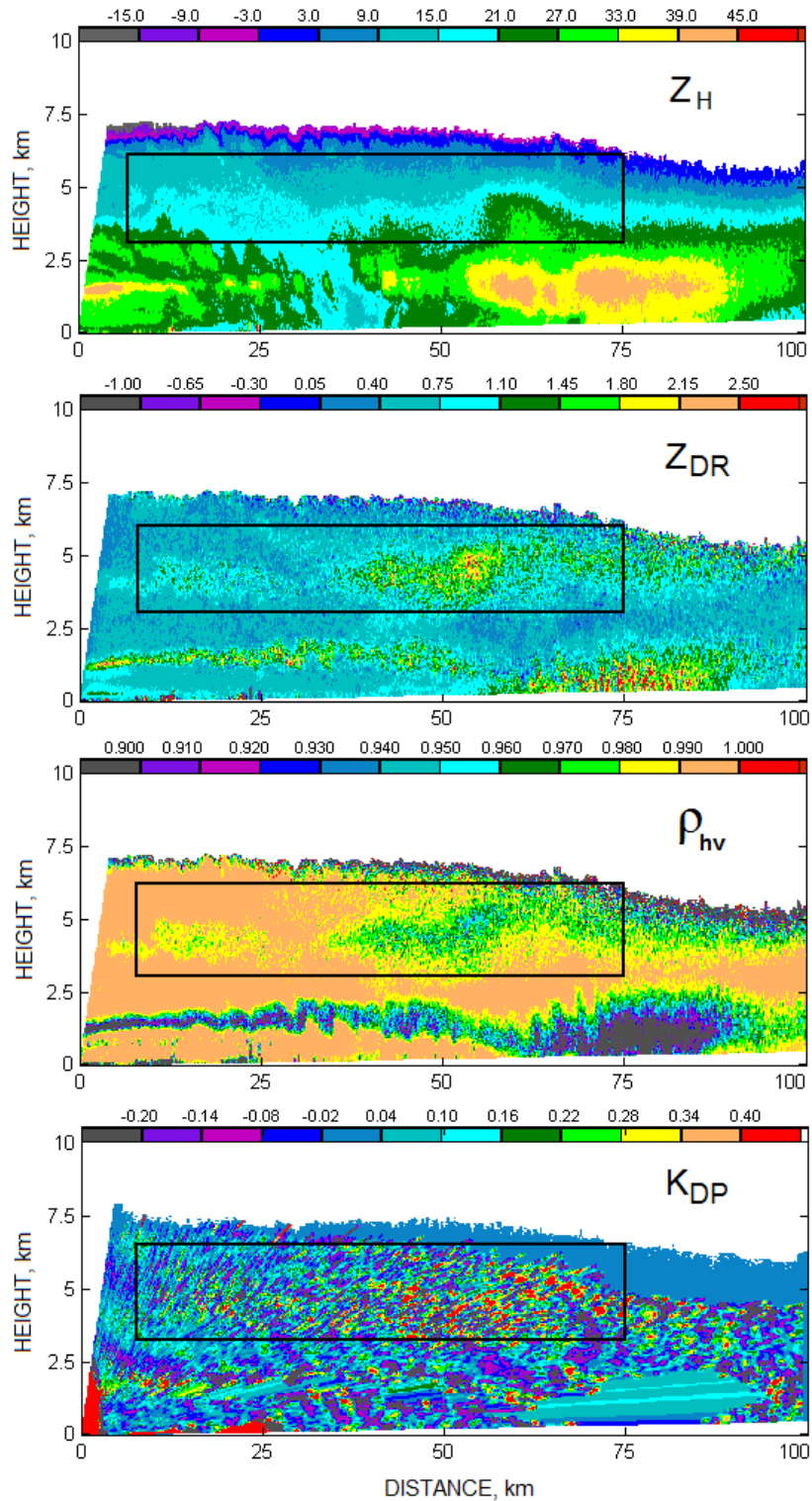
Figure 4.4: RHI of Z_H (in dB), Z_{DR},(in dBZ), ρ_{hv} and K_{DP} (in ^{o} km^{-1}) at the azimuth of 189°, measured with KOUN radar at 2254 UTC January 27 2009. Emphasized area indicates the signature under consideration in each panel.
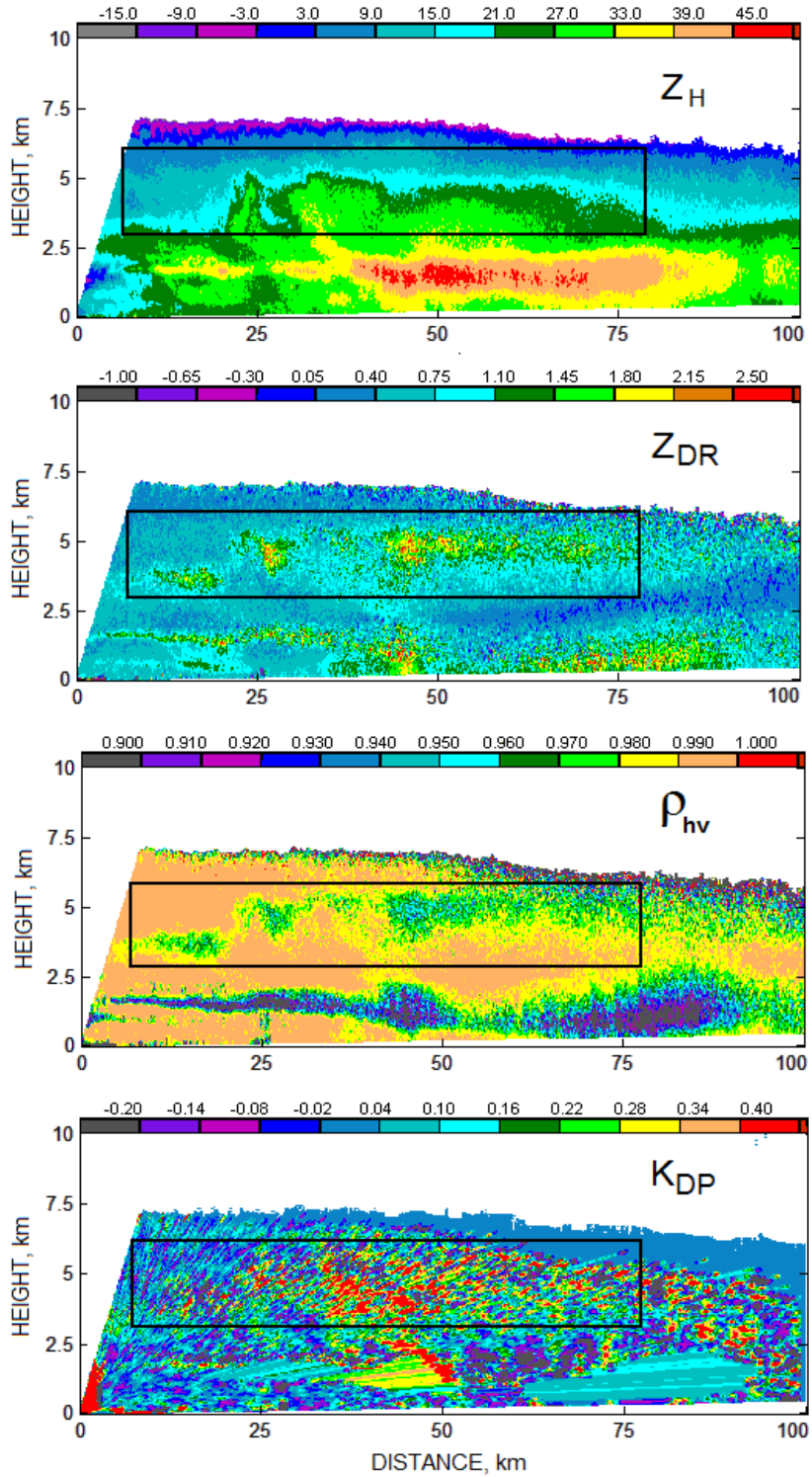
Figure 4.5: As in Fig. 4.4, at the azimuth of 181°, at 2317 UTC January 27 2009.
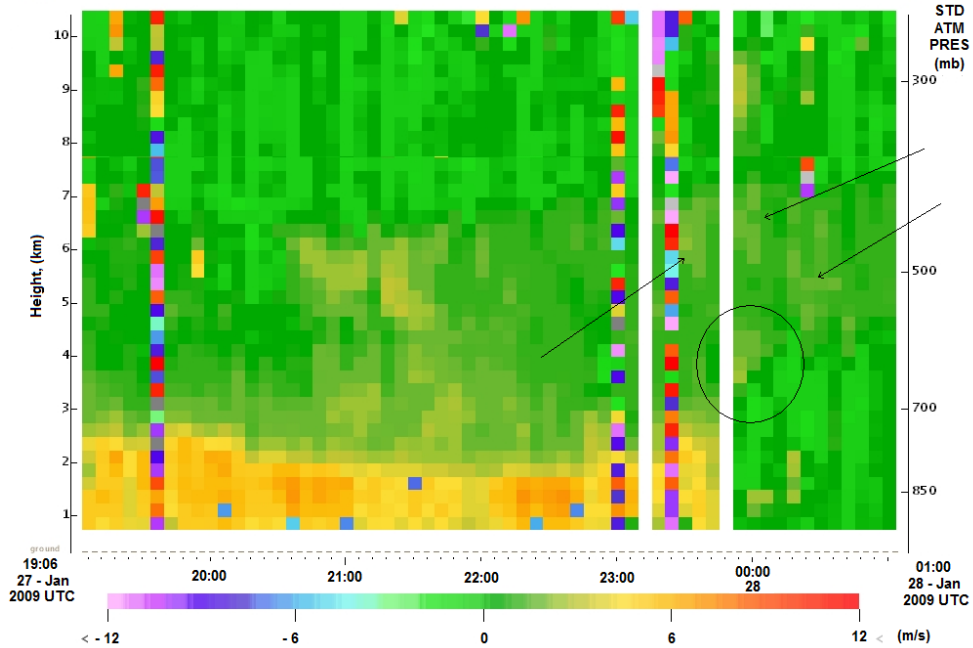
Figure 4.6: Radial velocity from the Purcell wind profiler, from vertical beam and at 6-min resolution. Marked areas indicate regions with radial velocity close to 3 m s^{-1}.

4.2.2 Vertical profiles of polarimetric variables

For a quantitative analysis of the observed polarimetric variables, vertical profiles through the "pockets" of enhanced Z_{DR} are constructed at several distances from the radar. Vertical profiles of K_{DP} are omitted because of its noisiness. For the Z_{DR} signature collected in the RHI scan along azimuth 189° (Fig. 4.7), profiles are made at 43 and 54 km from the radar. The main features in Z_H, Z_{DR} and ρ_{hv} are evident in both profiles (c.f. Figs. 4.8 and 4.9), but still they differ to some extent.
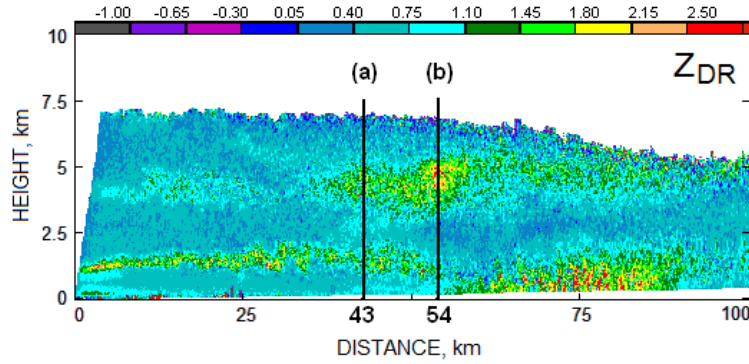
Figure 4.7: Observed Z_{DR} (in dB) along azimuth 189°, at 2254 UTC. (a) and (b) indicate the distance from radar where vertical profiles through pockets of enhanced Z_{DR}, are made.

In Fig 4.8, Z_H and Z_V gradually increase from the top of the cloud (6.6 km) all the way down to melting level (< 2 km), where Z_H reaches 36 dBZ, and Z_V 34 dBZ. In the layer from 5 to ~ 3.8 km, where enhanced Z_{DR} occurs, Z_H ranges form 12 to 18 dBZ. Z_{DR} is about 0.3 dB at the cloud top, which is a typical value for ice clouds, and it indicates particles with no extreme axis ratio or low-density particles. Approximately 400 m below cloud top height, Z_{DR} starts to increase gradually reaching 1.7 dB at 4.2 km AGL. At approximately 3.9 km AGL, Z_{DR} decreases sharply to 0.6 dB after only 200 m and remains at about 0.8 dB down to the melting layer, where it increases again. The sharp decrease in Z_{DR}, paired with increasing Z_H, indicates a decrease in particle density and increase in particle size due to aggregation. The decrease of $\rho_{hv,}$ from the cloud top downward follows the increase of Z_{DR}, falling to 0.97 at 4.6 km AGL.
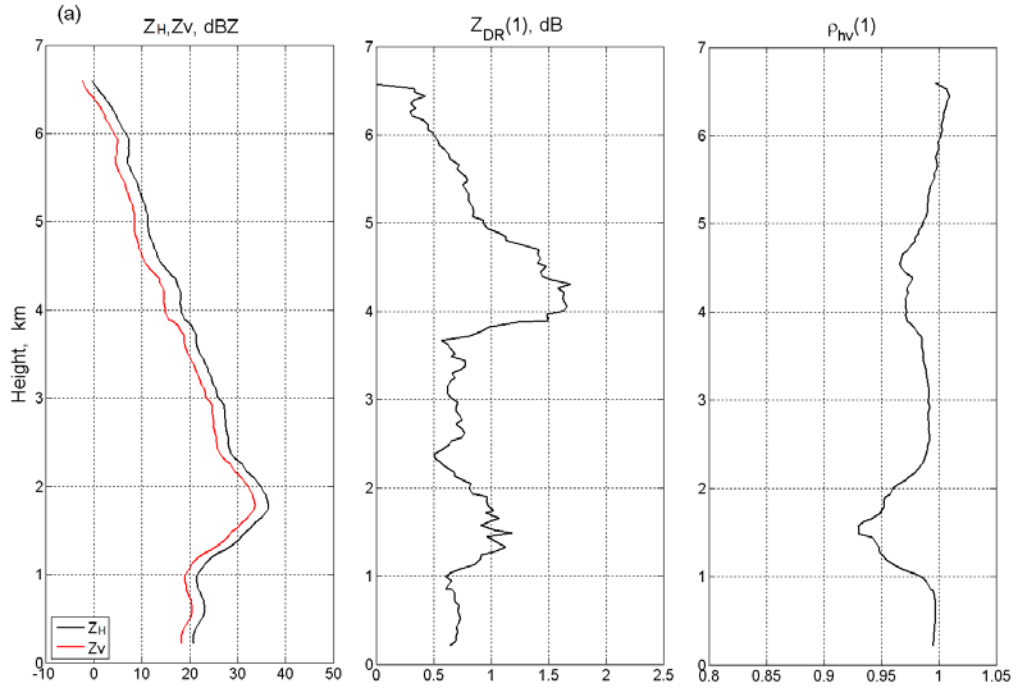
Figure 4.8: Vertical profile of Z_H, Z_V, Z_{DR} and ρ_{hv}, made at 43 km from the radar

Compared to the previous profile (Fig. 4.8), there are slight differences in all three signatures given in Fig. 4.9. The layer of enhanced Z_{DR} is wider, from 5.5 to 3.5 km, and the maximum value is 2.2 dB. This could be the consequence of stronger updraft and thus an increased growth rate of ice crystals. Z_H ranges form 13 to 19 dBZ and has a small increase at level of maximum $Z_{DR,}$ compared to the Z_{DR} signature in Fig 4.8. One possible reason for this could be a slight increase in number concentration, which is noticeable in Z_H but not in Z_{DR}. ρ_{hv} is decreased through the whole layer of enhanced Z_{DR}, reaching lower value of 0.95 at 5 km altitude, compared to the previous profile.
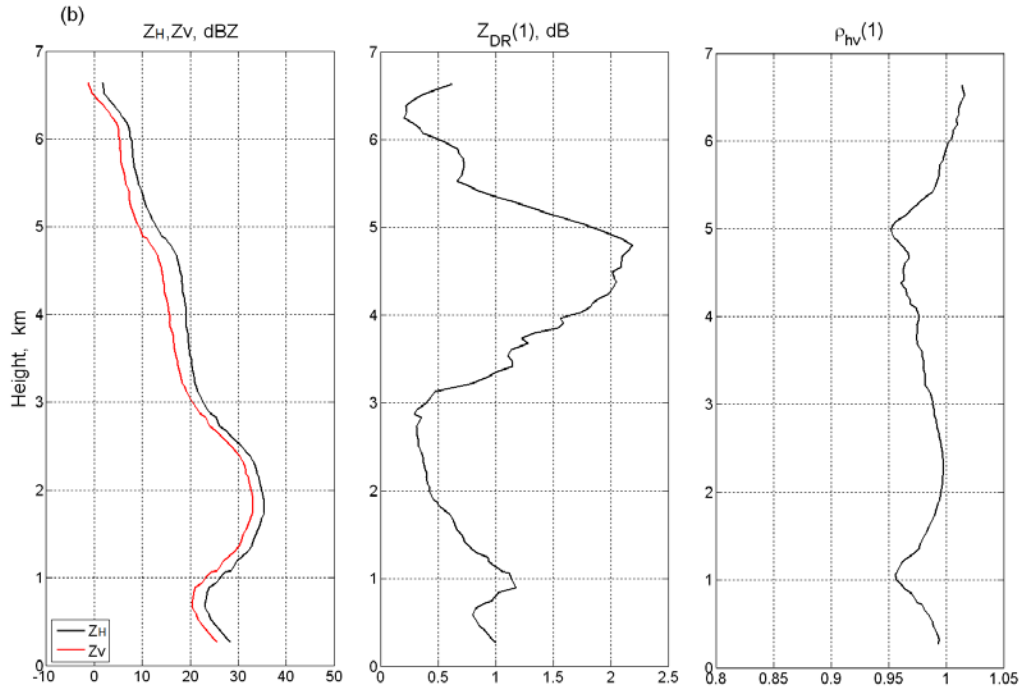
Figure 4.9: Vertical profile of Z_H, Z_V, Z_{DR} and ρ_{hv}, made at 54 km from the radar

For the Z_{DR} signature, observed in the RHI along the azimuth 181° (Fig. 4.10), profiles are made at 27, 45 and 52 km from the radar.
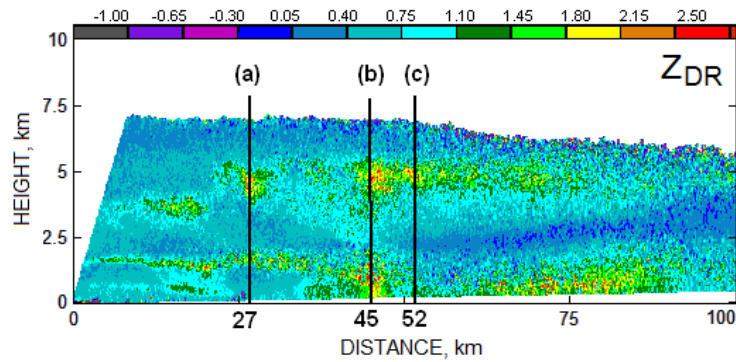
Figure 4.10: Observed Z_{DR} (in dB) at azimuth 181°, at 2317 UTC. (a), (b) and (c) indicate the distance from radar where vertical profiles through pockets of enhanced Z_{DR}, are made.

In Fig. 4.11, the profile of Z_H is different compared to the previous profiles. The increase in Z_H is not gradual and it is interrupted by a local maximum at approximately 4 km AGL. It comes just below the Z_{DR} maximum, which is at 4.6 km. Since this is the only profile with this type of Z_H signature, we cannot say whether the Z_H maximum is related to the Z_{DR} maximum. However, this decrease of Z_H could be the result of a drop in number concentration due to aggregation. Z_{DR} is about 0.3 dB at the cloud top down to 5.7 km, where it increases to 0.7 dB. Then from 5 km to 4.5 km Z_{DR} rapidly increases and reaches a maximum value of 2.2 dB. As before, the decrease in ρ_{hv} is coincident with the Z_{DR} increase, but in this case it reaches 0.95.
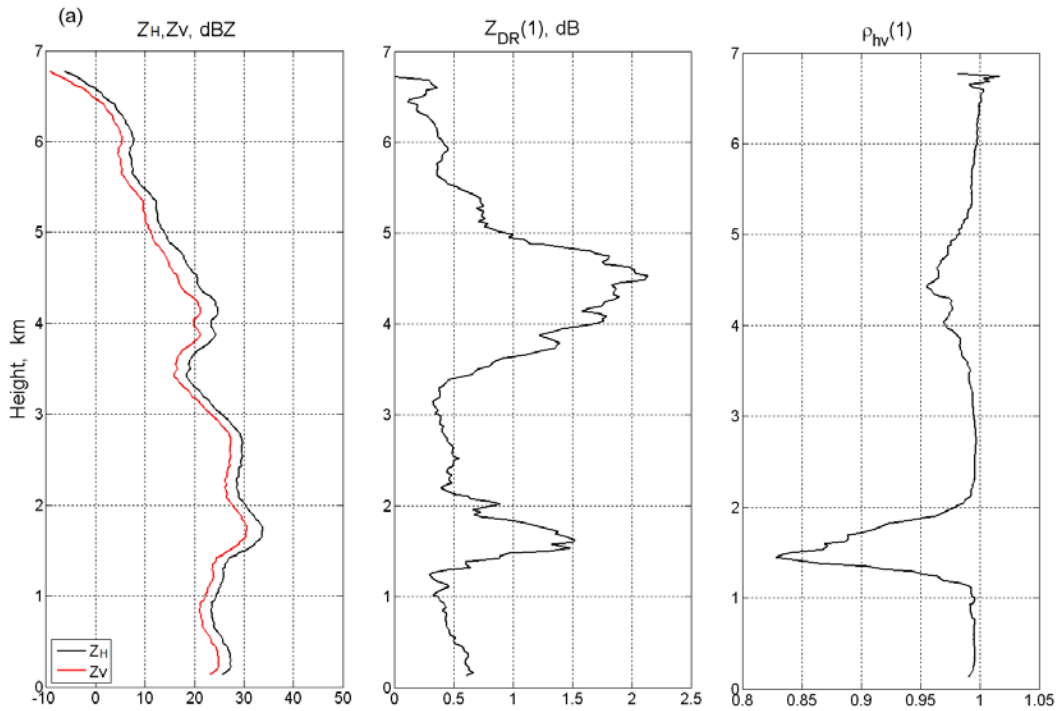
Figure 4.11: Vertical profile of Z_H, Z_V, Z_{DR} and ρ_{hv}, made at 27 km from the radar

In the vertical profile given in Fig. 4.12, Z_H and Z_V gradually increases from the cloud top down, indicating that there are no abrupt changes in concentration. In this case,

values are higher in the layer between 5 km and 4 km, ranging from 17 to 24 dBZ, respectively. As in previous profiles, Z_{DR} of 0.2 dB at 6.5 km is increasing downward and reaching 0.4 dB in 600 m thick layer. Below 5.7 km, Z_{DR} continues to increase, reaching 2.3 dB at 4.7 km. Moving down in height, Z_{DR} decreases to about 1 dB at 3.5 km, and continue to decrease to 0.7 dB at 2.3 km. ρ_{hv} is equal to unity from the cloud top down to 6 km, and then starts to decrease within the layer where Z_{DR} increases. ρ_{hv} remains above 0.95, as in previous profiles.
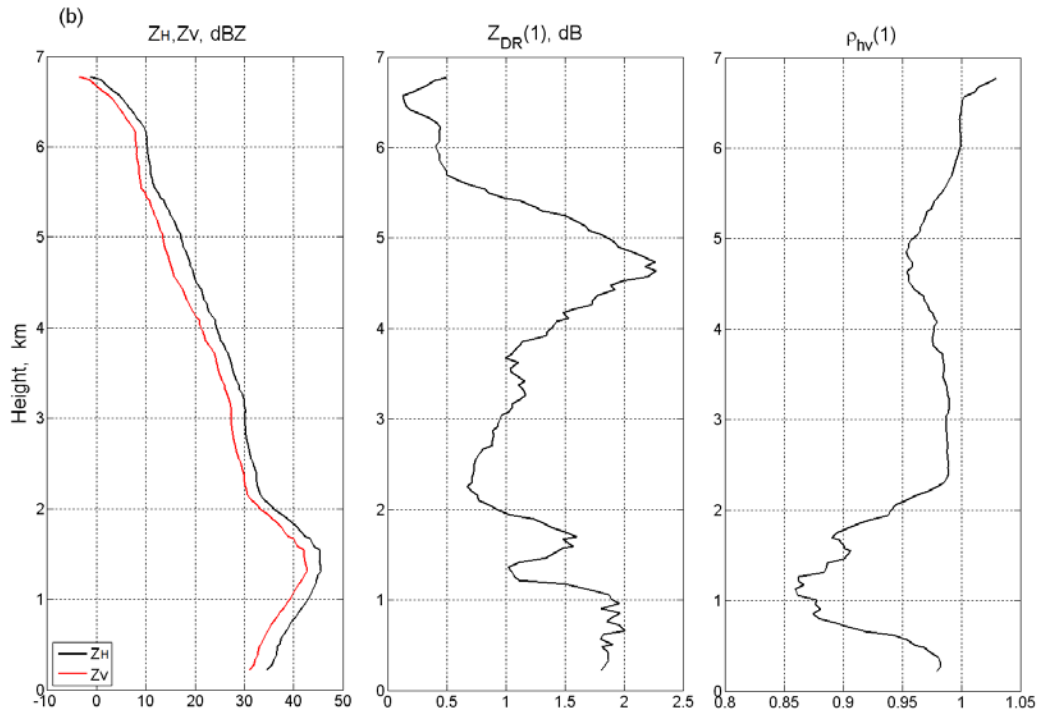
Figure 4.12: Vertical profile of Z_H, Z_V, Z_{DR} and ρ_{hv}, made at 45 km from the radar.

In the vertical profile given in Fig. 4.13, Z_H and Z_V signatures differ from the ones in Fig. 4.11, where maximum in reflectivity factor was observed. Z_H is increasing from 5.7 km (9 dBZ) down to 2.6 km (33 dBZ). Z_{DR} profile has the same shape like in previous figures, with slightly smaller value of 1.8 dB, followed by slightly higher of 0.96 ρ_{hv}. Differences in reflectivity factor from Figures 4.9, 4.11 and 4.13, compared to other

profiles (see Figures 4.8 and 4.12) might be a consequence of secondary ice production effecting the ice crystal concentration in localized areas.
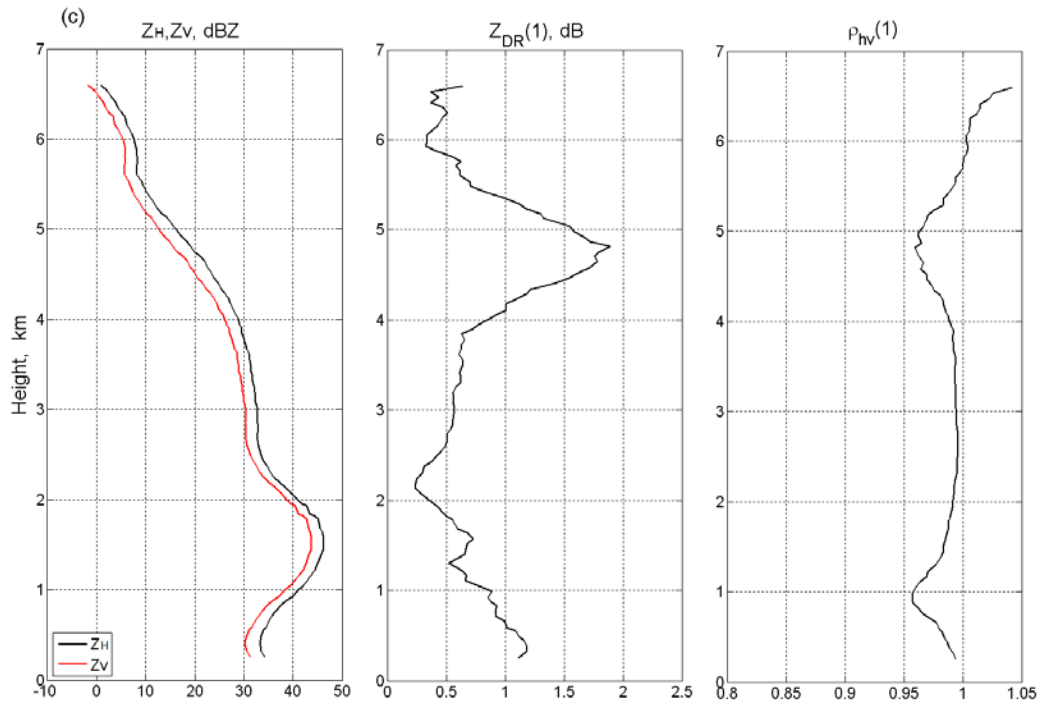
Figure 4.13: Vertical profile of Z_H, Z_V, Z_{DR} and ρ_{hv}, made at 52 km from the radar

As a summary of the obtained radar observations, Fig. 4.14 is given along with processes that possibly lead to the observed Z_{DR} enhancement. Vertical profiles in figures 4.8 and 4.12 show that Z_H and Z_V increase from the cloud top down gradually, which means that there are no sudden changes in concentration. In three out of five profiles (Figures 4.9, 4.11 and 4.13), there is maximum in reflectivity factor coinciding with Z_{DR} maximum, which can be a consequence of secondary ice production in localized areas.
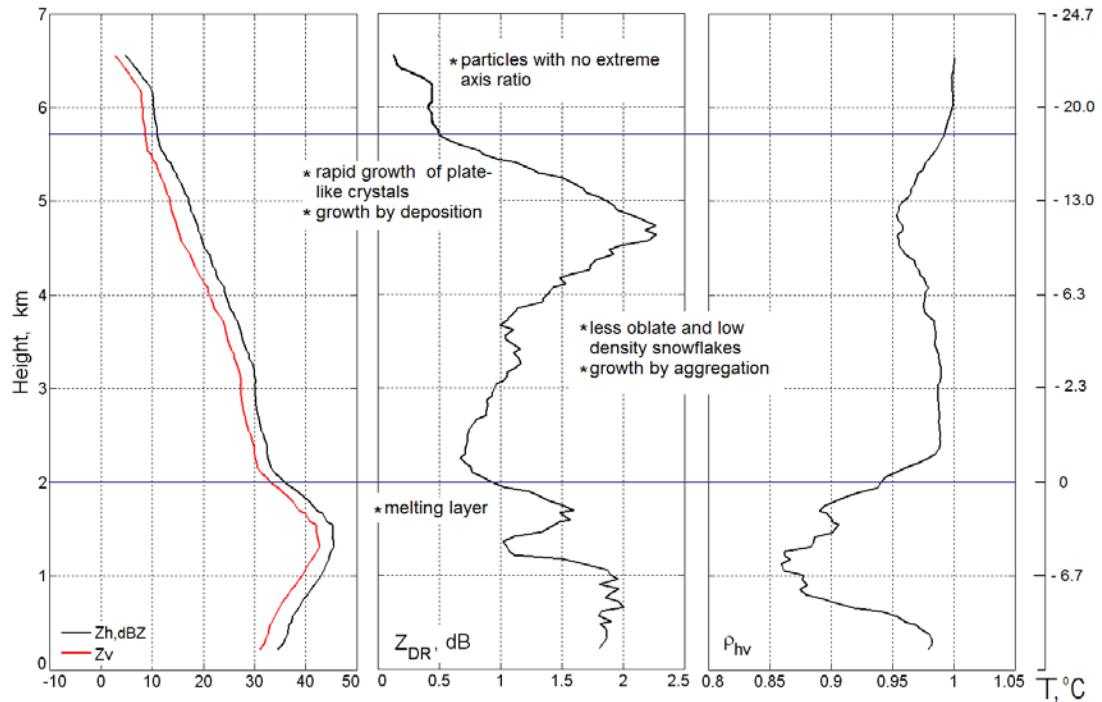
Fig. 4.14: Vertical profile of observed polarimetric variables with temperature profile on the right side.

The increased difference between Z_H and Z_V produces the maximum in Z_{DR} (2.3 dB) at approximately 4.7 km. The maximum of enhanced Z_{DR} usually occurs at approximately -12 °C. From both earlier, laboratory based habit diagram (Magono and Lee 1966; Young 1993) and the more recent one, improved with data from cloud particle imager (Bailey and Hallett 2008), we know that temperature regime of -10 °C to -15 °C is favorable for dendritic growth. However, aircraft observation by Korolev *et al.* (2000), indicate that most frequently observed crystals tend to be highly irregular. Also, both dendrites and needles can occur in isolated cells embedded in zones of irregular crystals. Those embedded cells could be the observed "pockets" of enhanced Z_{DR}. Furthermore, particles that occur in temperature range of -8 °C to -10 °C of the new habit diagram (Bailey and Hallett 2008), belong to dendritic type of crystals (Fig 2.6). Note the variety of their shape, going from stellar dendrites with long and narrow branches to dendrites with wide

49

branches that are very much plate-like. The presence of these types of dendrites would result in significantly different polarimetric signature, and that sensitivity to ice crystal habit should be kept in mind during the upcoming discussion about parameterization of ice crystals.

4.2.3 Similar observations of enhanced Z_{DR}

Apart from previous studies described in section 3.1 and the case considered herein, 3 more events where this signature was observed are presented. Only RHI's of Z_H, Z_{DR} and ρ_{hv}, along with sounding closest to the time when RHI's were made, are presented. We can say that the enhanced Z_{DR} signature is frequently observed. Areas where Z_{DR} is enhanced are marked in the figure for all three variables.

An RHI from a winter stratiform cloud, observed along azimuth 27° at 23:02 on 12 January 2007 is given in Fig. 4.15. The sounding at 0000 UTC 12 January 2007, Norman Oklahoma is given in Fig. 4.16. Notice that Z_{DR} of ~1.5 dB occurs in the temperature region from -10 °C to -15 °C, as in the previously analyzed case.
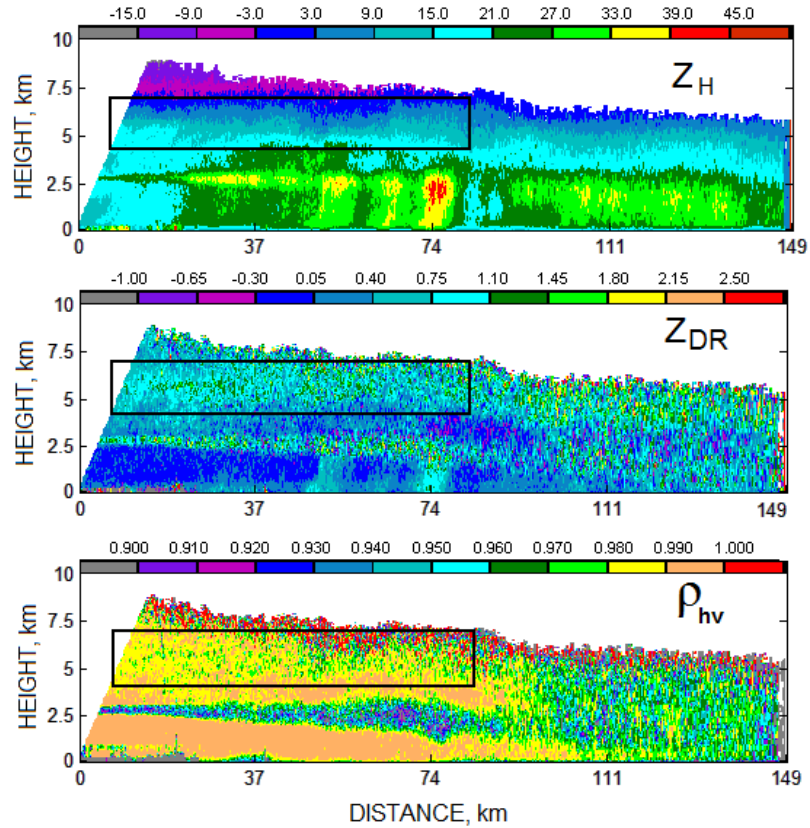
Figure 4.15: Genuine RHI of Z_H (in dB), Z_{DR} (in dBZ), ρ_{hv} at the azimuth of 27°, measured with KOUN radar at 2302 12 January 2007. Emphasized area in each panel indicates the signature under consideration.
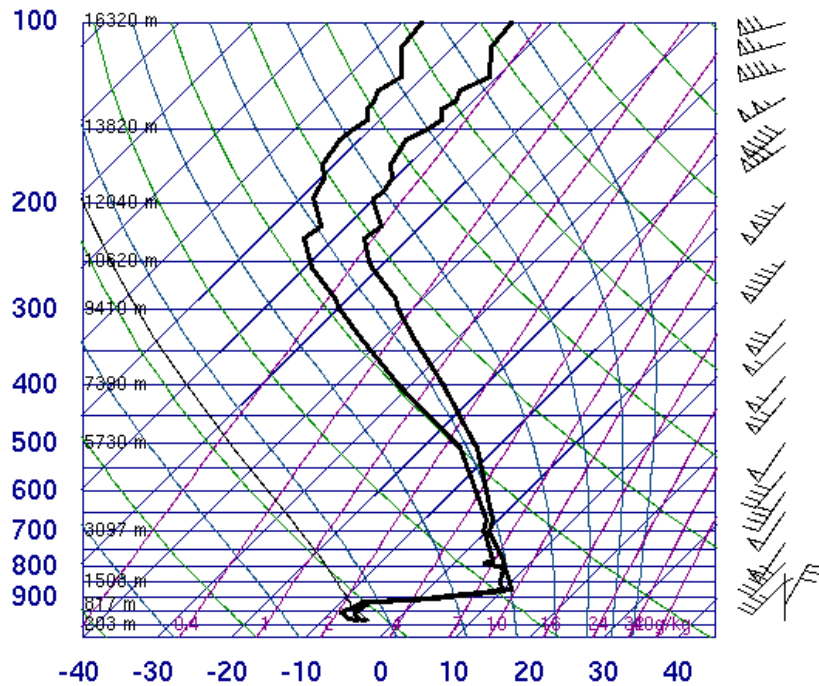
Figure 4.16: Sounding from Norman, Oklahoma at 0000 UTC 13 January 2007.

51

The enhanced Z_{DR} is not observed only in winter stratiform clouds. An RHI along azimuth 180° in a stratiform part of the convective storm made at 1507 on 18 August 2008 is presented in Fig. 4.17. The corresponding sounding is presented in Fig. 4.18. The layer of enhanced Z_{DR} occurred at around 6 km AGL, also in the temperature range of -10 °C to -15 °C. Because of complexity in both dynamical and microphysical properties of convective storms, we are not comparing or analyzing enhanced Z_{DR} signature related to convective clouds.
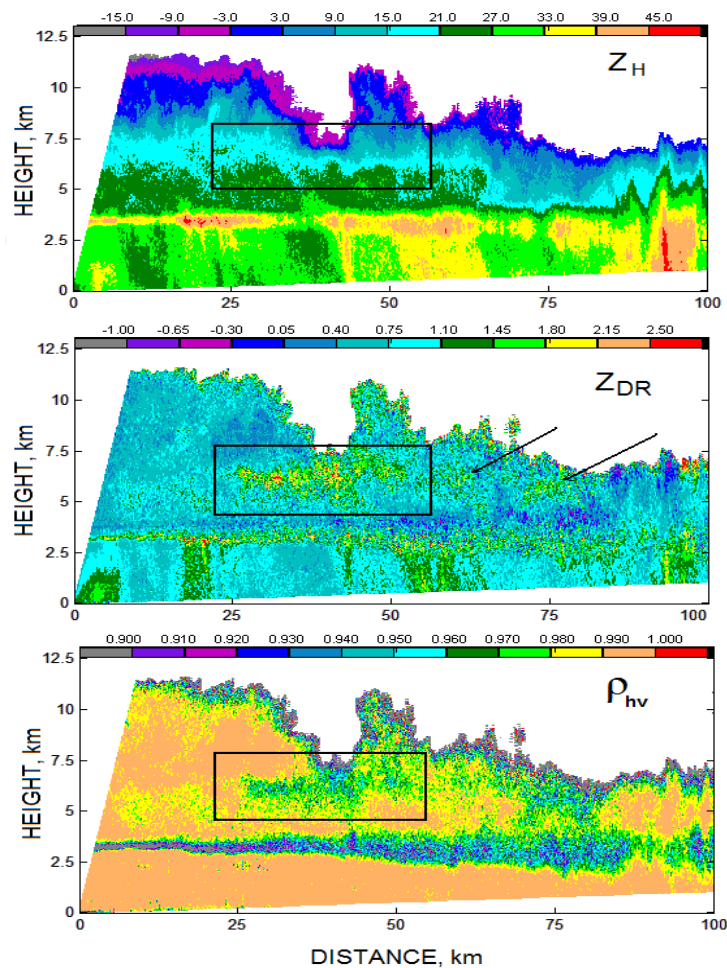
Figure 4.17: Genuine RHI of Z_H (in dB), Z_{DR}, (in dBZ), ρ_{hv} at the azimuth of 180°, measured with KOUN radar on August 18, 2008 at 1507. Emphasized area in each panel indicates the signature under consideration.
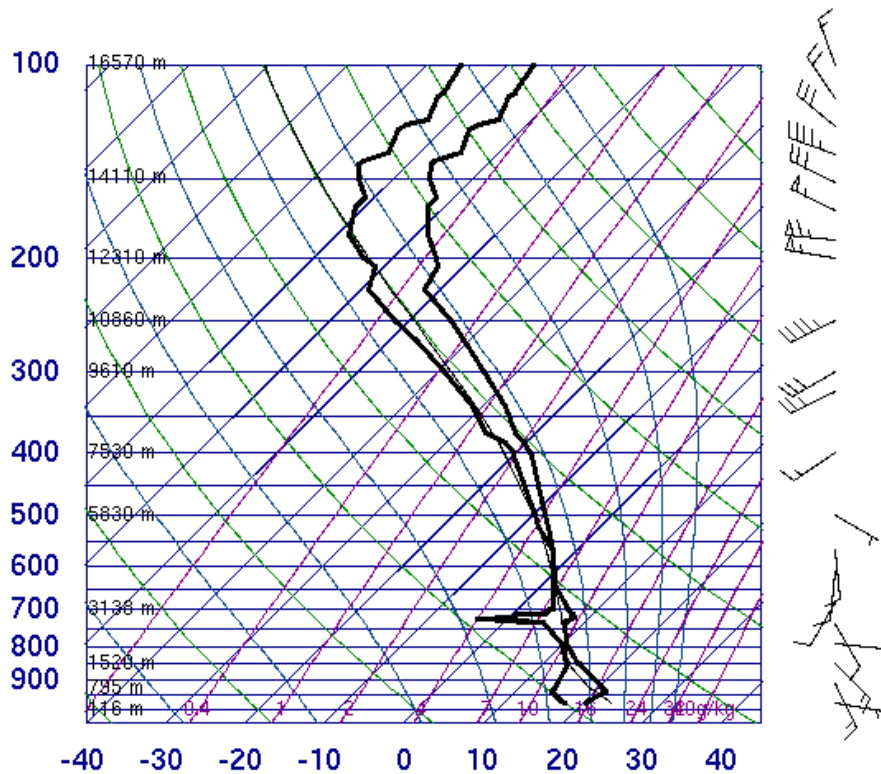
Figure 4.18: Sounding from Norman, Oklahoma at 1200 UTC 18 August 2008.

The last case is a winter storm that occurred on 24 December 2009. Observations were made with the C-band Polarimetric Radar for Innovations in Meteorology and Engineering (OU-PRIME; see Palmer et al. 2011), located in Norman, Oklahoma. Note the very pronounced melting layer in the Z_H profile at 1.5 km in Fig. 4.19. Pockets of enhanced Z_{DR} of near 2.3 dB were present (during the whole storm life time) above the melting level within the layer of 3 to 8 km AGL. The sounding from Norman, Oklahoma for 1800 UTC on 24 December 2009 is given in Fig. 4.20. The temperature in this layer decreases with height from -4 ℃ at 3 km, -8.5 ℃ at 4 km, -15.5 ℃ at 5 km, and -17.5 ° C at 5.5 km to -21.5 ℃ at 6 km. Also note that air was supersaturated with respect to water to approximately 3.5 km AGL.

53
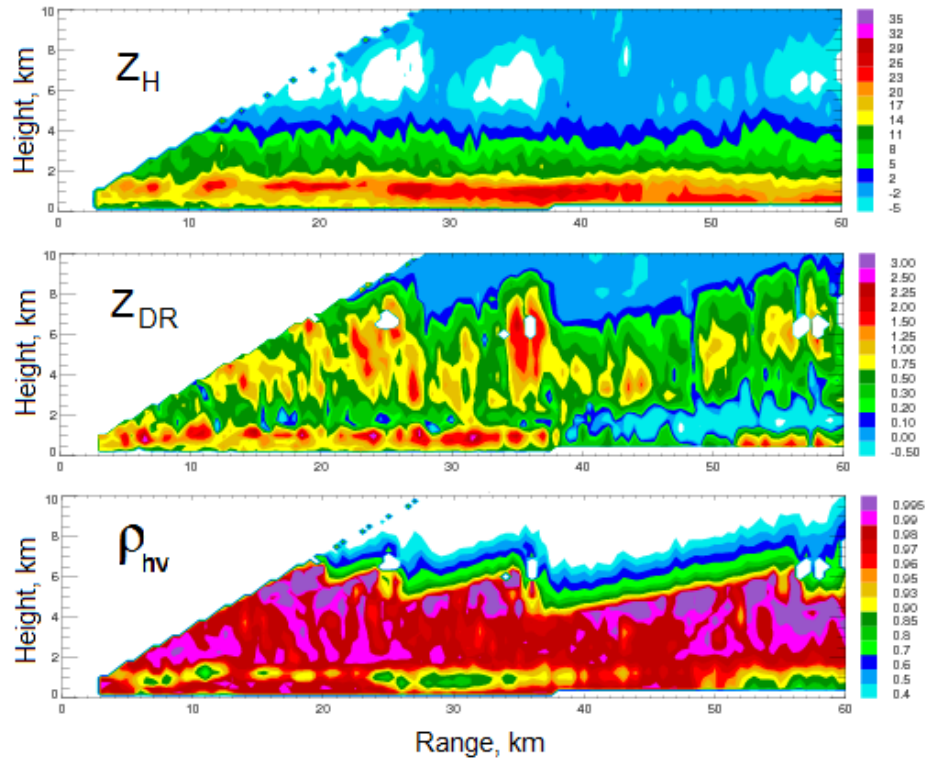
Figure 4.19: Generated RHI of Z_H (in dB), Z_{DR}, (in dBZ), and ρ_{hv} at the azimuth of 270°, measured with the C-band OU PRIME at 1736 UTC 24 December 2009.
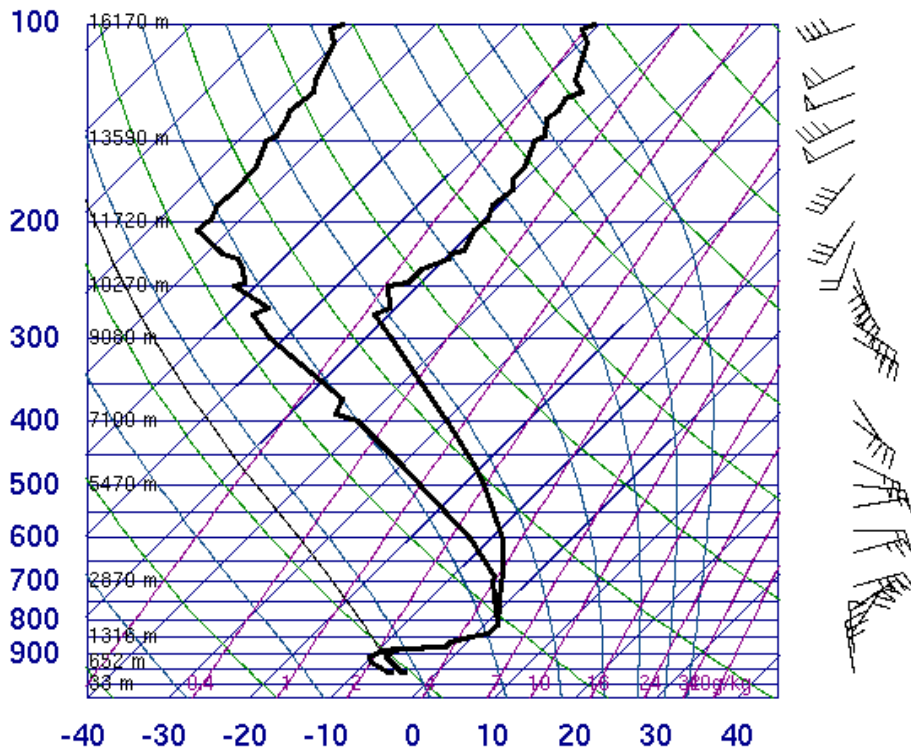
Figure 4.20: Sounding from Norman, Oklahoma at 1800 UTC 24 December 2009.

4. Model description

The model used for reproducing the observed polarimetric signature contains a microphysical component and an electromagnetic scattering component. Decisions about ice crystal habits and processes that are included in the microphysical scheme are based on observations from laboratory experiments and natural clouds described in section two. Given the complexity of crystal shape, their parameterization as spheres or spheroids is a significant simplification. However, the microphysical scheme includes all important processes for the formation of stratiform precipitation. The description of each component of the model and equations used in both parts are given this chapter.

5.1 Description of microphysical component of the model

A one-dimensional (1-D) bulk microphysical and time varying scheme, capable of reaching a steady state, has been developed by Dr. J. Straka. It is a two-moment scheme, meaning it calculates predictive equations for hydrometeor mixing ratio and total number concentration for each particle of hydrometeor category.

The model is based on the 1.5-D model from Ogura and Takahashi (1971) that assumes a circular air column (cylinder), with a large time-independent radius (a=3 km) in an environment at rest. Equations in Ogura and Takahashi (1971) have been formulated in one-dimensional space according to Asai and Kasahara (1967). Their model consists of two concentric air columns, the inner one that represents the cloud and corresponds to updraft and the outer one that represents the environment and region of compensating downward motion.

The model used in this study combines the vertical equation of motion, the equation of mass continuity, and the thermodynamic equation. Thus, it calculates predictive equations for vertical velocity of the air (w), potential temperature (θ), and vapor mixing ratio (Q). The vertical velocity equation, which is integrated over the cross section of the cloud column with radius a, is given as:

$$\frac{\partial w}{\partial t} = -w\frac{\partial w}{\partial z} - \frac{2\alpha^2}{a}w|w| + K_h\frac{\partial^2 w}{\partial z^2} + g\left(\frac{\theta - \theta_0}{\theta_0} + 0.608(Q_v - Q_{v0}) - \sum_{x=1}^{8}Q_x\right) \quad (5.1)$$

The first term on the right hand side (RHS) is vertical advection, the second term is lateral eddy exchange or mixing (where α^2 is mixing parameter = 0.1, from Asai and Kasahara 1967), the third term is turbulent mixing (K_h is eddy mixing coefficient), the fourth term is buoyancy, which includes the drag force or precipitation loading term that is assumed to be provided by the weight of cloud droplets and ice crystals. Q_v is the mixing ratio of water vapor, θ is the potential temperature, g is the gravitational acceleration. Subscripts 0 and x denote environment values and hydrometeor class, respectively.

Similarly, the thermodynamic equation is given as:

$$\frac{\partial \theta}{\partial t} = -w\frac{\partial \theta}{\partial z} - \frac{2\alpha^2}{a}(\theta - \theta_0)|w| + K_h\frac{\partial^2(\theta - \theta_0)}{\partial z^2} + S_\theta . \quad (5.2)$$

The last term S_θ on the RHS represents source and sink terms, given below. The change in potential temperature due to latent heating is given as:

$$S_\theta : \quad \frac{d\theta}{dt} = \frac{L_v}{c_p\pi}(QxINT) + \frac{L_f}{c_p\pi}(QxACC + QxFZy) + \frac{L_s}{c_p\pi}(QxDPV) - \frac{L_f}{c_p\pi}(QxMLy), \quad (5.3)$$

where L_v is the latent heat of condensation/evaporation, L_f of freezing and L_s of deposition, c_p is specific heat of air at constant pressure. The first term on the RHS

56

represents warming due to condensation, the second term due to freezing and accretion, the third term due to deposition, and the last one is cooling due to melting. The Exner function, π is given by:

$$\pi = \left(\frac{p}{p_0}\right)^{\frac{Rd}{Cp}}$$

(5.4)

The model includes two liquid hydrometeor classes (cloud droplets and rain) and six ice classes that are categorized by habit (hollow columns, dendrites, plates, columns/needles, snow aggregates, and ice pallets/sleet). Fig. 5.1 shows the temperature at which certain ice class is initiated. Snow crystals are formed by self-collection and interaction between dendrites, plates and columns.
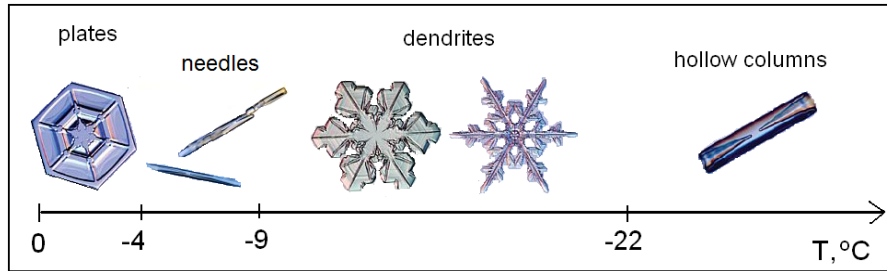
Figure 5.1: Graphical description of initiation ice crystal habits included in the scheme, as a function of environmental temperature.

For each ice class we calculate prognostic equations for mixing ratio (Q_x) and total number concentration (N_{Tx}), given as:

$$\frac{\partial Q_x}{\partial t} = -\frac{1}{\rho}\frac{\partial \rho w Q_x}{\partial z} + \frac{Q_x}{\rho}\frac{\partial \rho w}{\partial z} + \rho K_h \frac{\partial^2 Q_x}{\partial z^2} + \frac{2\alpha^2}{a}|w|Q_x + \frac{1}{\rho}\frac{\partial\left(\rho \overline{V}_{T_{Q_x}}Q_x\right)}{\partial z} + SQ_x,$$

(5.5)

$$\frac{\partial N_{Tx}}{\partial t} = -\frac{\partial w N_{Tx}}{\partial z} + \rho K_h \frac{\partial^2 (N_{Tx}/\rho)}{\partial z^2} + \frac{2\alpha^2}{a}|w|N_{Tx} + \frac{\partial\left(\overline{V}_{T_{Q_x}}N_{Tx}\right)}{\partial z} + SN_{Tx},$$

(5.6)

where the first two terms on RHS of equation 5.5 and the first term of equation 5.6 represents vertical advection, the third term represents turbulent mixing, and the

57

sedimentation term (fallout of crystals due to gravitation) with a source/sink term is at the end. V_{TNx} is mass weighted terminal velocity of each category, and ρ is air density. The model assumes a special form of a gamma size distribution for ice particles, where the shape parameters from the complete gamma function $\alpha, \mu, \nu = 1$. This special case of the gamma function distribution is more commonly known as the inverse exponential distribution.

$$n(D) = \frac{N_T}{D_n} \exp\left[-\left(\frac{D}{D_n}\right)\right] = N_0 \exp(-\Lambda D).$$

(5.7)

Where D is diameter and D_n is the scaling diameter, and N_T is number concentration (number of particles per m^{-3}). The intercept parameter N_0 for exponential distribution, and slope parameter Λ are:

$$N_0 = \frac{N_T}{D_n}, \quad \Lambda = \frac{1}{D_n}.$$

(5.8)

D_n is the characteristic scaling diameter (or horizontal axis of a particle), and it has been calculated for each category using the following equation:

$$D_{nx} = \left(\frac{Q_{nx}}{N_{Tx}} \frac{\rho}{a_x} \frac{1}{\Gamma(1+b_x)}\right)^{\frac{1}{b_x}},$$

(5.9)

where a_x and b_x are parameters from a power low relationship between mass and diameter, and Γ denotes the complete gamma function.

For each ice category we calculate the diagnostic equations for terminal velocity, particle density, and thickness (or vertical axis of a particle). Mean terminal velocity is calculated according to mass-weighted (or mixing ratio-weighted) term, given as:

$$V_{TNx} = c_x D_{nx}^{d_x} \frac{\Gamma\left(b_x + v_x + d_x\right)}{\Gamma\left(b_x + v_x\right)}.$$

(5.10)

Mass, density and thickness are calculated using the power low relationships:

$$m_x = aD_{nx}^b, \quad \rho_x = eD_{nx}^f, \quad h_{nx} = gD_{nx}^h$$

(5.11)

Densities of plates and sleet are equal to density of solid ice (0.917 g cm^{-3}). Densities for dendrites, columns, and snow aggregates are being calculated using the equation given above. Snow aggregates and sleet are parameterized as spheres, dendrites and plates as oblate spheroids, whereas needles and hollow columns are parameterized as prolate spheroids. However, for snow aggregates, a constant axis ratio equal to 0.75 is used in the scattering part of the model.

Equations are integrated using the finite-difference method on staggered grid. For all spatial derivatives we have used second-order centered differences, and leap-frog scheme for time derivatives. The model time step is 0.5 s and spatial resolution is 25 m. For boundary conditions, we set the vertical velocity $w = 0$ at the surface and at the top of the atmosphere, which is assumed to be at 10 km. Equations were initiated with temperature, water vapor mixing ratio and pressure from the 0000 UTC 28 January 2009 sounding from Norman, Oklahoma (see Fig. 4.1).

5.1.1. Microphysical processes

The microphysical scheme includes the following processes: condensation of water vapor that forms cloud droplets, nucleation of ice crystals (contact and depositional), depositional growth, riming, aggregation, melting of ice crystals and refreezing that produces ice pellets. Because the model does not include a saturation

59

adjustment scheme, saturation with respect to water (S_l) as well as saturation with respect to ice (S_i) is set to constant value ($S_l = S_i = 0.80$ from 7.5 to 10 km; $S_l = 1.05$ from 7.5 km to the ground and $S_i = 1.15$ from 3 km to the ground).

Condensation

For initiation of cloud droplets, we are using the procedure adapted from Milbrandt and Yau (2005b), where cloud nucleation rate is given as:

$$cc\,\text{int} = \frac{\max\big[(actccn(w,T,p)-ccnn),0\big]}{\Delta t},$$ (5.12)

where *actccn* is concentration of nucleated cloud droplets in ascending air to the maximum supersaturation, and *ccnn* is total number concentration of cloud droplets initiated per time step. The procedure described by Cohard and Pinty (2000a) provides a solution for maximum supersaturation as a function of updraft speed, temperature and pressure. In our simplified model *actccn* and S_l are constant values (these would be different if saturation adjustment scheme were introduced). Cloud droplets are initialized when S_l is greater than 1.

Ice nucleation

The number of ice nuclei initiated by deposition and by contact is a function of temperature and supersaturation and is determined using a parameterization described by Meyers et al. (1992). Depositional nucleation is a process where water vapor molecules attach to ice nuclei, and conditions for its occurrence are temperature below -5 ℃ and vapor mixing ratio that exceeds that of saturation over ice. A parameterization of ice-nucleus concentrations as a function of ice supersaturation is given as:

60

$$N_{id} = 1000 \cdot \exp\left(12.96\left(S_i - 1\right) - 0.639\right), \tag{5.13}$$

where N_{id} is the number of nucleated crystals in m^{-3}. This equation may be applied for temperature ranges from -7 ºC to -20 ºC and from 2% to 25% ice supersaturation, and -5% to +4.5% of water supersaturation.

Contact nucleation occurs when ice nuclei come into contact with existing supercooled cloud droplet. Potential contact-freezing concentrations (in m^{-3}) were parameterized according to Meyers et al. (1992) as:

$$N_{ic} = 1000 \cdot \exp\left(-2.8 + 0.262\left(T_0 - T\right)\right) \tag{5.14}$$

where T is cloud droplet temperature and $T_0 = 273.15$ °C. According to this mode of nucleation, ice cannot be formed at temperatures warmer than -2 ºC. It is assumed that contact-freezing nuclei have size 0.1 µm. Colliding of ice nuclei and cloud droplets that can lead to contact nucleation is caused by Brownian, thermophoretic and diffusiophoretic effects Young (1974a,b). Collection rates determine the actual number of nucleated ice crystals.

Depositional growth

Particles that grow by deposition are: dendrites, plates, columns, and snow aggregates. The growth equation assumes an inverse exponential distribution and is taken from Straka (2009), but originates from Prupacher and Klett (1997):

$$Q_x DS_L = \frac{2\pi}{\rho}\left(S_i - 1\right)G_i\left(T, P\right) \times \left(0.78 D_{nx} + 0.308\Gamma\left(\frac{3 + d_x}{2}\right)N_{sc}^{1/3} c_x^{1/2} D_{nx}^{(3+d_x)/2}\left(\frac{\rho_0}{\rho}\right)^{1/4}\right), \tag{5.15}$$

where S_i is supersaturation with respect to ice, ρ is air density, and G_i is given as:

$$G_i(T,P) = \cfrac{1}{\left(\cfrac{L_s}{R_v T} - 1\right)\cfrac{L_s \rho_i}{KT} + \cfrac{\rho_i R_v T}{\psi e_{SI}(T)}}.$$

(5.16)

Here, the Schmidt number *Nsc* number is assumed to be a constant equal to 0.71. Ventilation factors for particles with diameter > 120 μm are included in the growth equation and given as:

$$f_v = \left(0.78 + 0.308 N_{sc}^{1/3} N_{re}^{1/2}\right).$$

(5.17)

Riming

The continuous collection equation is used for snow, dendrites, plates, and columns which collect cloud water. The equation is explained in Pruppacher and Klett (1997) and Rodgers and Yau (1989). The form of the equation used in the model is written for the modified gamma distribution from Straka (2009):

$$Q_x A C_y = \frac{\pi}{4} c_x D_{nx}^{2+d_x} E_{xy} Q_y \frac{N_{Tx}}{\Gamma(v_x)}\left(\frac{\rho_0}{\rho}\right)^{\frac{1}{2}} \Gamma\left(2 + d_x + v_x\right).$$

(5.18)

Where E_{xy} is the collection efficiency and is equal to 1.

Aggregation

Two processes of crystal accretion are included: 1) self collection of dendrites, ice plates, columns and snow aggregates, and 2) collection of dendrites, plates, and columns by snow aggregates and collection of plates and columns by dendrites. The growth equation for self collection (Passarelli and Srivastava 1979) is given as:

$$Q_x C N_y = \frac{\pi}{4} E_{xy} D_y^2 Q_y^2 V_y,$$

(5.19)

62

where V_y is the terminal velocity and E_{xy} is the ice-ice collection efficiency equal to 0.1.

The continuous growth equation is given according to Gilmore et al. (2004a):

$$QxACy = \frac{\pi}{4} E_{xy} Q_x n_x \left| \overline{V_x} - \overline{V_y} \right| \times \frac{1}{\Gamma(4)} \left[\Gamma(4)\Gamma(3)D_{nx}^2 + 2\Gamma(5)\Gamma(2)D_{nx}D_{ny} + \Gamma(6)\Gamma(1)D_{ny}^2 \right].$$
(5.20)

Also, the correction for terminal velocity from Murakami (1990) was included. A correction is made to $\left| \overline{V_x} - \overline{V_y} \right|$, because of underestimation of $QxACy$ when V_x is too close to V_y, and it is given as:

$$\left| \overline{V_x} - \overline{V_y} \right| \approx \sqrt{(\overline{V_x} - \overline{V_y})^2 + 0.04\overline{V_x V_y}}.$$

(5.21)

Similarly, the equation for concentration change is given as:

$$N_{Tx}ACy = \frac{\pi}{4} E_{xy} N_{Txy} n_x \left| \overline{V_x} - \overline{V_y} \right| \times \frac{1}{\Gamma(4)} \left[\Gamma(3)\Gamma(1)D_{nx}^2 + 2\Gamma(2)\Gamma(2)D_{nx}D_{ny} + \Gamma(1)\Gamma(3)D_{ny}^2 \right].$$
(5.22)

Melting of ice

All ice crystals begin to melt into rain when they reach level with 0 °C. The equation for melting ice particles is from Gilmore et al. (2004), which was adapted from Lin et al. 1983, is given as:

$$Q_xML_{rw} = \left\{ \begin{array}{c} -\dfrac{2\pi N_{Tx}\left[K(T-T_0) + \rho\psi L_v(Q_v - Q_{s0}) \right]}{\rho\Gamma(v_x)L_f} \\[2ex] \times \left[0.78\Gamma(1+v_x)D_{nx} + 0.308c_x^{1/2}v^{-1/2}N_{sc}^{1/3}D_{nx}^{(3+d_x)/2}\Gamma\left(\dfrac{3+d_x}{2}+v_x\right)\left(\dfrac{\rho_0}{\rho}\right)^{\frac{1}{4}} \right] \\[2ex] -\dfrac{c_L(T-T_0)}{\rho L_f}\left(\displaystyle\sum_M Q_xAC_L\right) \end{array} \right\}$$
(5.23)

It is assumed that mass from all melted crystals is transferred to raindrops. The number concentration change owing to melting is given as:

$$N_{T_x} ML_{rw} = Q_x ML_{rw} \frac{N_{T_x}}{Q_x}.$$

(5.24)

Freezing

The equation for freezing of the raindrops is based on Bigg (1953) design of the data fit for the freezing of raindrops, and on the parameterization of Wisner et al. (1972). The equation for mixing ratio and concentration for each hydrometeor category, derived for modified gamma distribution is given as:

$$Q_{fw} FZ_x = \frac{\Gamma(6+\nu_x)\pi^2 BN_{Tx} D^{5+\nu_x}{}_{nx}}{36\Gamma(\nu_x)}\left(\frac{\rho_L}{\rho}\right)\left\{\exp\left(A\max[T_0-T],0.0\right)-1\right\},$$

(5.25)

$$N_{Tfw} FZ_x = \frac{\Gamma(3+\nu_x)\pi BN_{Tx} D^{2+\nu_x}{}_{nx}}{6\Gamma(\nu_x)}\left\{\exp\left(A\max[T_0-T],0.0\right)-1\right\}.$$

(5.26)

5.2 Description of scattering component of the model

The scattering model is applied to each ice class of the microphysical scheme to calculate polarimetric variables and its description is given herein. Thus, using the output from bulk microphysical scheme, we attempt to reproduce quantitatively and qualitatively the observed radar polarimetric signature. As mentioned in the previous text, an inverse exponential distribution is used for all types of hydrometeors that are included in the model. This is a simplification of the microphysical computations that has been accepted by many researchers, although it might not capture all the details of the actual polarimetric signature observed in winter stratiform clouds.

Radar polarimetric variables depend on size, shape, orientation of individual hydrometeor as well as on the dielectric constant, which is a function of hydrometeor density, water content, temperature, and the wavelength of the incident radiation. Thus, from microphysical model, diameter, thickness and density of particles are used to calculate polarimetric variables for dendrites, needles, plates, and snow aggregates individually as well as their cumulative sum. Calculations for rain and sleet are omitted, because the focus is on reproducing the signature above melting layer. Calculations for hollow columns are also omitted, because their size and concentration are small enough that they do not produce appreciable Z_H and therefore their contribution to the radar variables is negligible.

For the winter stratiform event considered herein, the observed sounding shows that temperatures were subfreezing from the cloud top (-30 °C at 7.3 km) down to 3 km AGL (-4 °C). The melting level is at approximately 1.6 km and the enhanced Z_{DR} signature is observed in a layer between 4.5 and 5 km AGL. Thus, the melting particles did not affect the observed signature, which is the reason for treating only the ice phase.

For calculations of polarimetric variables at S-band (radar wavelength equal to 11 cm), the Rayleigh approximation is used. This approximation is valid because the model treats ice particles that are all much smaller than the radar wavelength. All equations used in the scattering model can be found in Ryzhkov *et al*. (2011), unless otherwise specified.

The equation for scattering amplitude is given as:

$$f_{a,b} = \frac{\pi^2 D^3}{6\lambda^2} \frac{1}{L_{a,b} + \frac{1}{(\varepsilon_s - 1)}}$$

(5.27)

where D represents equivalent volume diameter of the particle, given as:

$$D = \left(ab^2\right)^{\frac{1}{3}}. \qquad (5.28)$$

where a is the vertical axis of the hydrometeor (thickness), and b is its horizontal axis (diameter). $L_{a,b}$ are shape parameters, which for oblate spheroids are defined as:

$$L_a = \frac{1+f^2}{f^2}\left(1 - \frac{\arctan f}{f}\right), \quad f = \sqrt{\frac{b^2}{a^2} - 1}, \quad L_b = \frac{1 - L_a}{2} \qquad (5.29)$$

and for prolate spheroids, as:

$$L_a = \frac{1-e^2}{e^2}\left(\frac{1}{2e}\ln\left(\frac{1-e}{1+e}\right) - 1\right), \quad e = \sqrt{1 - \frac{b^2}{a^2}}, \quad L_b = \frac{1 - L_a}{2} \qquad (5.30)$$

For calculating the dielectric constant, the Maxwell Garnett (1904) mixing formula is used. Dielectric constant of dry snow ε_s is determined by volume fraction of ice f_{vi} ($f_{vi} \approx \dfrac{\rho_s}{\rho_i}$) in the mixture with air and dielectric constants of ice ε_i and air ε_a.

Assuming that $\varepsilon_a \approx 1$ we obtain the following equation:

$$\varepsilon_s = \frac{1 + 2\dfrac{\rho_s}{\rho_i}\dfrac{\varepsilon_i - 1}{\varepsilon_i + 2}}{1 - \dfrac{\rho_s}{\rho_i}\dfrac{\varepsilon_i - 1}{\varepsilon_i + 2}}, \qquad (5.31)$$

where ρ_s is the density of particles (coming from model), and ρ_i is the solid ice density equal to 0.917 g cm^{-3}. The dielectric constant of pure ice ε_i is given by:

$$\varepsilon_i = 3.17 + i0.0013. \qquad (5.32)$$

This equation is used for plates, dendrites, columns, and snow aggregates.

Four radar polarimetric variables are computed: reflectivity factor for horizontal (Z_h) and vertical polarizations (Z_v), differential reflectivity (Z_{DR}), cross-correlation

coefficient (ρ_{hv}), and specific differential phase (K_{DP}). The equations are given for M different hydrometeor classes (i), as:

$$Z_h = \frac{4\lambda^4}{\pi^4 |K_i|^2} \sum_{i=1}^{M} \int_0^\infty \left\{ |f_{bi}|^2 - 2\,\mathrm{Re}\left[f_{bi}^* \left(f_{bi} - f_{ai} \right) \right] A_{2i} + |f_{bi} - f_{ai}|^2 A_{4i} \right\} N_i(D)\, dD$$

(5.33)

$$Z_v = \frac{4\lambda^4}{\pi^4 |K_i|^2} \sum_{i=1}^{M} \int_0^\infty \left\{ |f_{bi}|^2 - 2\,\mathrm{Re}\left[f_{bi}^* \left(f_{bi} - f_{ai} \right) \right] A_{1i} + |f_{bi} - f_{ai}|^2 A_{3i} \right\} N_i(D)\, dD$$

(5.34)

$$Z_{dr} = \frac{Z_h}{Z_v}, \quad Z_{DR} = 10\log_{10}\left(Z_{dr} \right)$$

(5.35)

$$\rho_{hv} = \frac{4\lambda^4}{\pi^4 |K_w|^2} \frac{\displaystyle\sum_{i=1}^{M} \int_0^\infty \left\{ |f_{bi}|^2 + |f_{bi} - f_{ai}|^2 A_{5i} - f_{bi}^* (f_{bi} - f_{ai}) A_{1i} - f_{bi}(f_{bi}^* - f_{ai}^*) A_{2i} \right\} N_i(D)\, dD}{(Z_h Z_v)^{1/2}}$$

(5.36)

$$K_{DP} = \frac{0.18\lambda}{\pi} \sum_{i=1}^{M} \int_0^\infty \mathrm{Re}(f_{bi} - f_{ai}) A_{7i} N_i(D)\, dD$$

(5.37)

We have assumed that particles are oriented horizontally, but experience fluctuations in their orientations. A 2-D axisymmetric Gaussian distribution of orientation has been used for dendrites, plates and snow aggregates. Angular moments for 2-D axisymmetric Gaussian distribution of orientation are given as (from Ryzhkov 2001; Ryzhkov et al. 2011):

$$A_1 = \frac{1}{4}(1+r)^2, \quad A_2 = \frac{1}{4}(1-r^2),$$

$$A_3 = \left(\frac{3}{8} + \frac{1}{2}r + \frac{1}{8}r^4\right)^2,$$

$$A_4 = \left(\frac{3}{8} - \frac{1}{2}r + \frac{1}{8}r^4\right)\left(\frac{3}{8} + \frac{1}{2}r + \frac{1}{8}r^4\right),$$

$$A_5 = \frac{1}{8}\left(\frac{3}{8} + \frac{1}{2}r + \frac{1}{8}r^4\right)(1-r^4),$$

$$r = \exp(-2\sigma^2), \tag{5.38}$$

where σ is the width of the canting angle distribution, and in calculations it is expressed in radians. For $\sigma = 0°$, particles are oriented horizontally. Gaussian distribution allows some degree of influence by choosing the different value for σ. In this study $\sigma = 35°$, for dendrites and plates, showed that calculated variables have values closest to the observed ones. For snow aggregates no orientation fluctuation is used. For the orientation fluctuation in the case of columns we used random orientation in horizontal plane, where angular moments are given as:

$$A_1 = \frac{1}{2}\sin^2\beta, \quad A_2 = \frac{1}{2}, \quad A_3 = \frac{3}{8}\sin^2\beta,$$

$$A_4 = \frac{3}{8}, \quad A_5 = \frac{1}{8}\sin^2\beta, \tag{5.39}$$

where β is the radar antenna angle.

6. Results

Using the output form the microphysical scheme, the following polarimetric variables are calculated: Z_H, Z_V, Z_{DR}, ρ_{hv} and K_{DP}. We used the output from the microphysical part of the model after 4 hours of integration. Calculations are done for

each ice category as well as for their cumulative sum. Notice that only bulk values (cumulative sums) of each modeled polarimetric variable can be compared with the observed ones. The calculated polarimetric variables are presented as a function of height (y axis), from the ground level up to 7 km. However, the emphasis is on the signature above the melting layer (i.e., above 2 km).

Note that signatures for all variables decrease toward the melting layer instead of increasing. This physically unrealistic result appears because particles are melting into rain, and only ice crystals were included in the calculation of polarimetric variables. For the 27 January 2009 winter stratiform event considered in the study, the sounding is given in Fig. 4.1. Note that temperatures were subfreezing from the cloud top (-30 °C at 7.3 km) down to the 3 km AGL (-4 °C). Melting level is at approximately 1.6 km and the enhanced Z_{DR} signature is observed in a layer from 4.5 to 5 km AGL. Thus, the melting particles did not affect the observed signature of interest in this study.

For the results presented herein, the microphysical scheme included only deposition and aggregation, with no riming. The shape and density of particles grown by riming depend on the degree of riming, which is a function vertical velocity of wind (a source of water vapor and supercooled liquid droplets). Fig. 6.1 shows the variety of ice crystal shapes grown by riming. Herein, when we talk about rimed particles we refer to densely or lightly rimed particles, where original habit of a crystal is still recognizable. Rimed particles usually have bulk density less than 0.8 g cm^{-3}, but it can vary from 0.05 to 0.89 g cm^{-3} due to the presence of a large number of air capillaries (List 1958a,b). Crystals fall with their larger surface oriented horizontally, thus droplets tend to "stick" onto their larger surfaces. Such growth regime makes crystals thicker or less oblate, as

the ratio between horizontal (diameter) and vertical (thickness) dimension decreases. As a result, Z_{DR} of rimed particles should be lower, compared to the particles grown by deposition. However, the expected enhancement of Z_{DR} depends on the degree of riming. Even only slightly rimed crystals could produce enhancement in Z_{DR}. Riming was not considered in this study because necessary conditions (i.e., supersaturation with respect to water) for riming were not satisfied above the melting layer (see Fig. 4.1). Thus, there is no contribution from riming to the part of the signature under consideration.
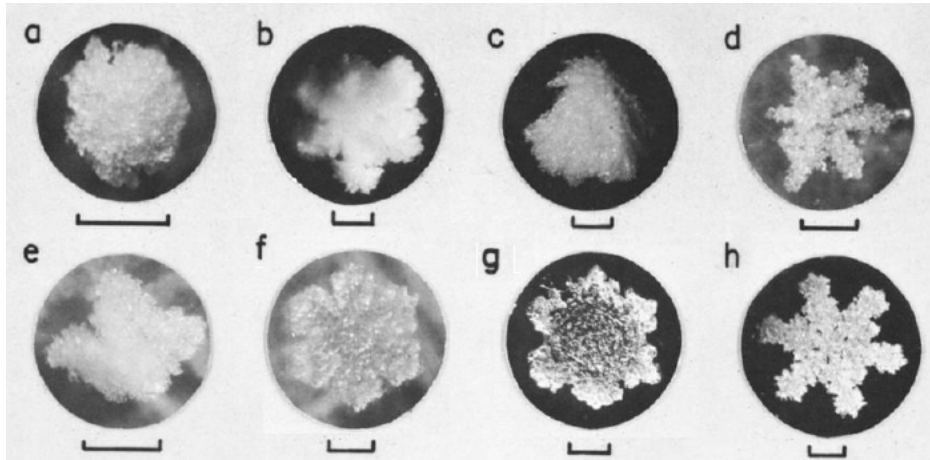
Figure 6.1: Ice crystals grown by riming. (a) lump graupel,(b) hexagonal graupel, (c) conical graupel, (d) graupel-like snow of hexagonal type, (e) graupel-like snow of lump type, (f) densely rimed crystal with sector-like branches, (g) densely rimed plate with simple extensions and (h) densely rimed dendrite. (Adapted from Locatelly and Hobbs 1974).

In the model, all particles start to grow from 10 µm. The maximum value allowed for the diameter of a dendrite is 3 mm, for snow aggregates 5 mm, plates have diameters up to 600 µm, and columns length is about 800 µm.

Ice water content (IWC) is calculated for each ice class separately as well as for their cumulative sum (Fig. 6.2). Dendrites and plates have IWC of about 0.05 g m^{-3}, needles have the highest IWC of about 0.1 g m^{-3}, whereas IWC for snow is the lowest (0.022 g m^{-3}). All maximum values occur within the layer between 3.5 and 4 km AGL.

Only the cumulative sum of IWC that includes all ice habits is comparable to the measured IWC. The maximum IWC for cumulative sum of about 0.21 g m^{-3} is at approximately 3.5 km. Calculated IWC agree to some extent with IWC measured by Hogan et al. (2001), which were made through the embedded convection regions, where values were 0.1 g m^{-3} for temperatures below 0 ℃. They measured the highest value of IWC (0.22 g m^{-3}) in high Z_H and low Z_{DR} regions which suggest contained rimed particles. According to the formula IWC = $3.22K_{DP}$ (Ryzhkov et al. 1998), for K_{DP}= 0.4 ° km^{-1}, the estimated IWC can reach 1.3 g m^{-3}.
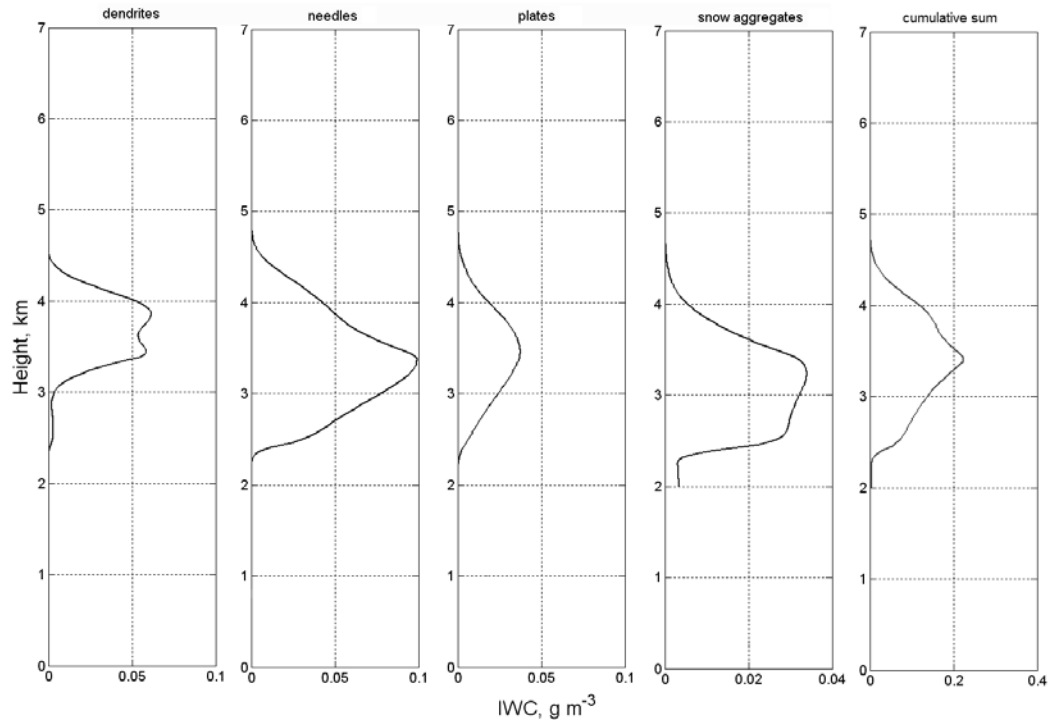
Figure 6.2: Ice water content (IWC) for each ice class and the cumulative sum of all classes.

Total number concentration, as obtained by the microphysical scheme for all ice categories and their cumulative sum, is presented in Fig. 6.3. Dendrites have the highest concentration and it is about 1.7×10^4 m^{-3} at 6 km; thus, the cumulative sum is affected by dendrite concentration the most. The concentration for columns, plates and snow

aggregates increases below 5 km and reaches the maximum concentration of 3000 particles in m^{-3} at 4.1 km for columns, near 1700 particles in m^{-3} for plates at 3.8 km, and near 16 particles in m^{-3} for snow aggregates at approximately 3.3 km.
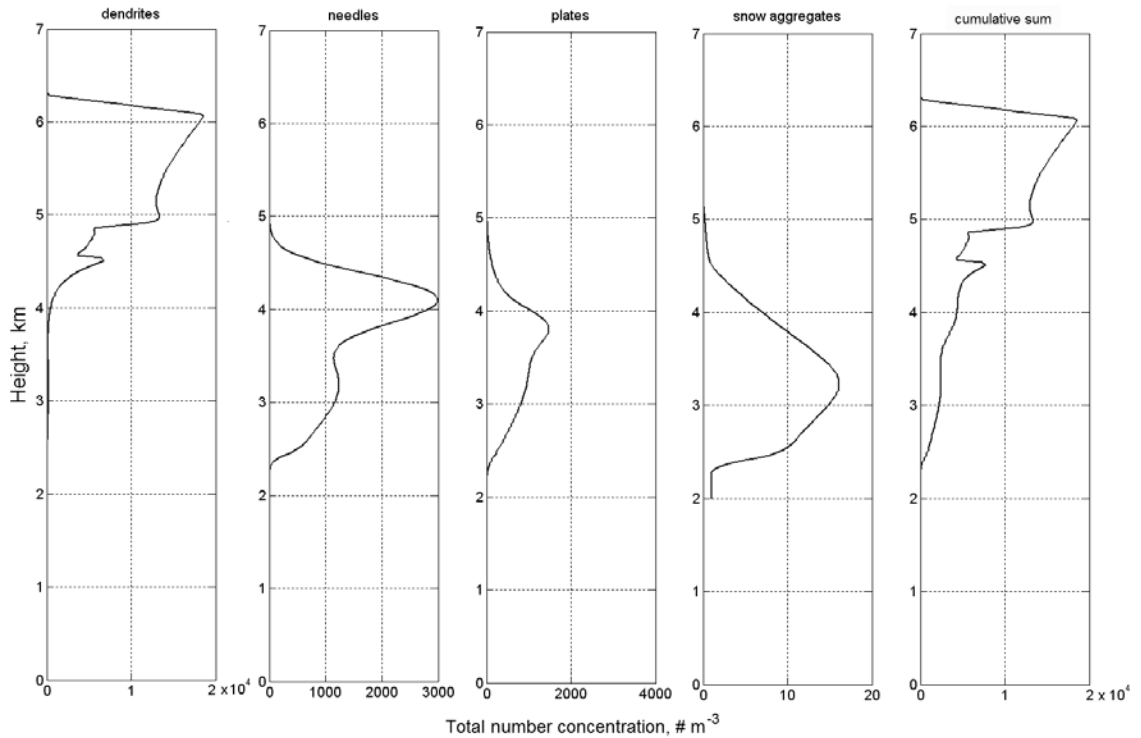
Figure 6.3: Total number concentration for each ice class and the cumulative sum of all classes.

The Z_{DR} is strongly dependent on particle density, so the calculated density for each ice class given in Fig. 6.4 is used for the analysis of calculated radar variables. The density of plates is constant and equal to 0.92 g cm^{-3}, the density of dendrites ranges form 0.92 to 0.4 g cm^{-3}, for snow it is from 0.08 down to 0.02 g cm^{-3}, whereas needles have density of about 0.86 g cm^{-3}.
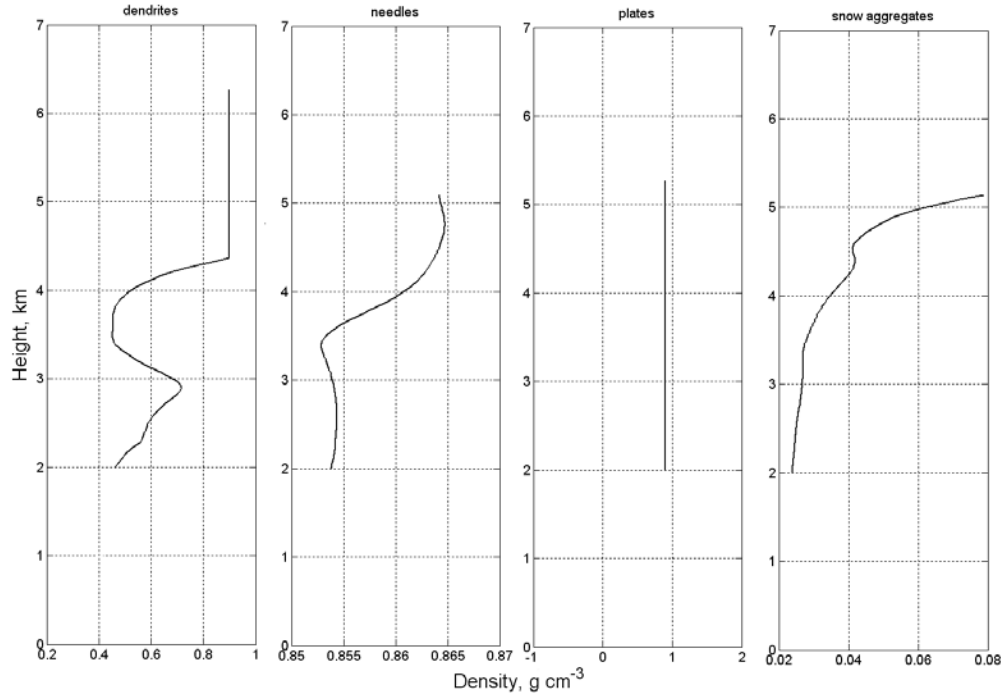
Figure 6.4: Calculated density for each ice class

Figure 6.5 presents calculated reflectivity factor at horizontal and vertical polarization for dendrites, needles, plates, snow aggregates and their cumulative sum. Z_H of -20 dBZ for dendrites appears at approximately 6.3 km, as well as Z_V which is less than Z_H by about 2 dBZ. Z_H and Z_V reach 0 dBZ at approximately 5.3 km, and decrease to -20 dBZ thereafter. The reason for such small Z_H values is the high total number of concentration and very small crystals (about 35 µm), implying high competition for water vapor and inability for dendrites to grow to larger sizes. Z_H and Z_V increase again to a maximum value of 17 dBZ at 4.6 km. Z_H and Z_V of needles that are initiated at approximately 5 km are about -20 dBZ. They increases up to a maximum of about 15 dBZ at 4.3 km, and below that height decrease to -20 dBZ at 2.2 km. Z_H and Z_V of plates appear at 5.2 km, with slightly negative values, and increase gradually reaching 27 dBZ at 4 km. Because plates have high Z_H, their contribution to the bulk value of reflectivity factor is significant. For snow aggregates Z_H and Z_V are the same, because of their

73

assumed spherical shape. The initial Z_H value for snow aggregates is 20 dBZ and it appears at 4.5 km. It increases gradually to nearly 35 dBZ at 3.5 km and stays nearly constant down to 2.5 km, and then it decreases again.

Finally, the bulk Z_H, Z_V profiles are comparable in shape to the observed signature described above, but have different values. Initial values of Z_H and Z_V at the cloud top are modeled at near 500 m below the initial value of the observed signature, and are -20 dBZ. The biggest contribution to the bulk Z_H is from snow aggregates and plates. Dendrites are important at the top part of the signature from 6.3 down to 5.3 km. The maximum of bulk Z_H between 3.5 and 2.5 km is 35 dBZ, and agrees very well with the observed value of Z_H, of about 33 dBZ (Fig. 4.13). Notice that the largest difference between observed and modeled values is at highest between 5.3 and 4.5 km.
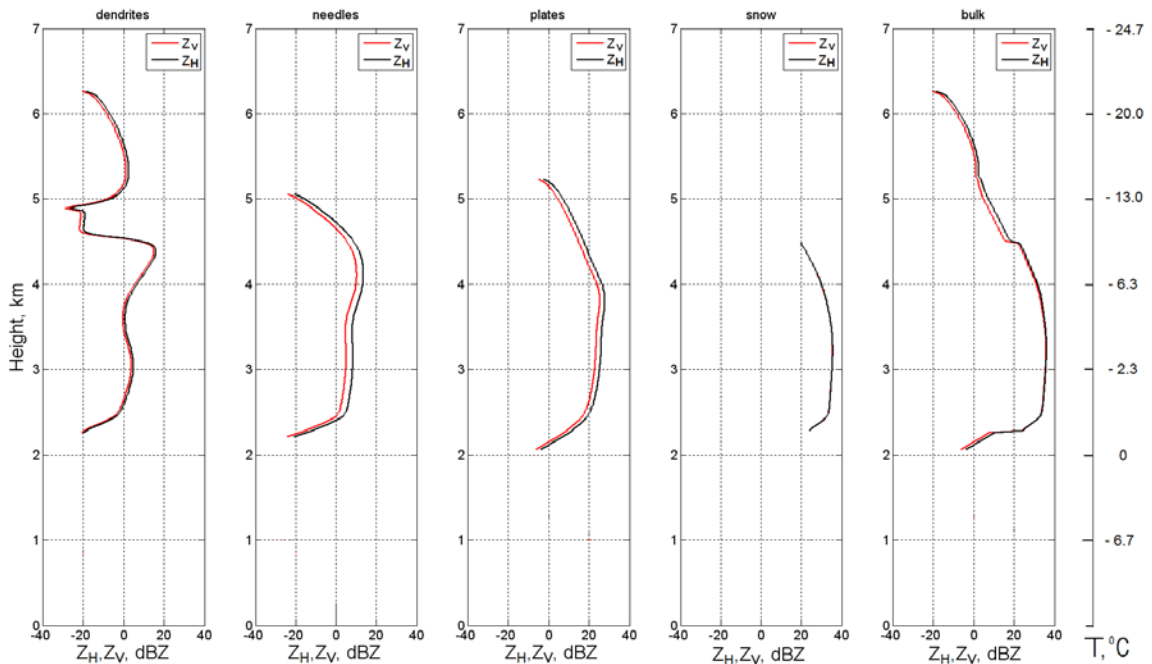
Figure 6.5: Calculated Z_H and Z_V for each ice class and their cumulative sum. On the right side of the figure temperature profile from sounding is included.

Fig. 6.6 presents the differential reflectivity calculated for dendrites, needles, plates, snow aggregates and their cumulative sum. Z_{DR} for dendrites at the cloud top is 1.7 dB, since plate-like axis ratios and solid ice density produce significant Z_{DR}. Moving down from 5 km, Z_{DR} increases and reaches its maximum value of 2 dB in the layer from 4.9 to 4.5 km. Beneath this height, Z_{DR} for dendrites drops to 1 dB due to aggregation. More about the reason for decrease in Z_{DR} for dendrites is given in the following section. Needles have a constant Z_{DR} of 3.3 dB from 5 km down to 2.2 km because their density changes very little. For the same reason (density is equal to 0.92 g cm^{-3}) plates have constant Z_{DR} equal to 2.5 dB. This difference in values can be explained by change in orientation. Snow aggregates start to form from 4.5 km and have weak and constant Z_{DR} (about 0.03 dB), because of their very low density and nearly spherical shape (constant aspect ratio of 0.75).

The bulk Z_{DR} has the same value as the one for dendrites (1.7 dB at the cloud top decreasing to 1.3 dB at near 5.2 km AGL) as long as dendrites are the only habit present. From height 5237 m, plates are initiated and have slightly negative Z_H (but higher from Z_H of dendrites), which causes Z_{DR} to increase reaching the maximal value of 2.6 dB at 4562 m. From the height of 5062 m AGL needles are initiated, but with negligible contribution to Z_{DR}, because Z_H for plates dominates (see Fig. 6.5). There is little contribution from needles to this part of the signature. In the case where needles are excluded from calculations the signature becomes smoother, and the slight increase in Z_{DR} at 4 km disappears (not shown). From 4562 m AGL, snow is initiated once aggregation process starts to dominate. This causes Z_{DR} to decrease suddenly to 0.9 dB at 4487 m, reaching the 0.1 dB at 2487 m.
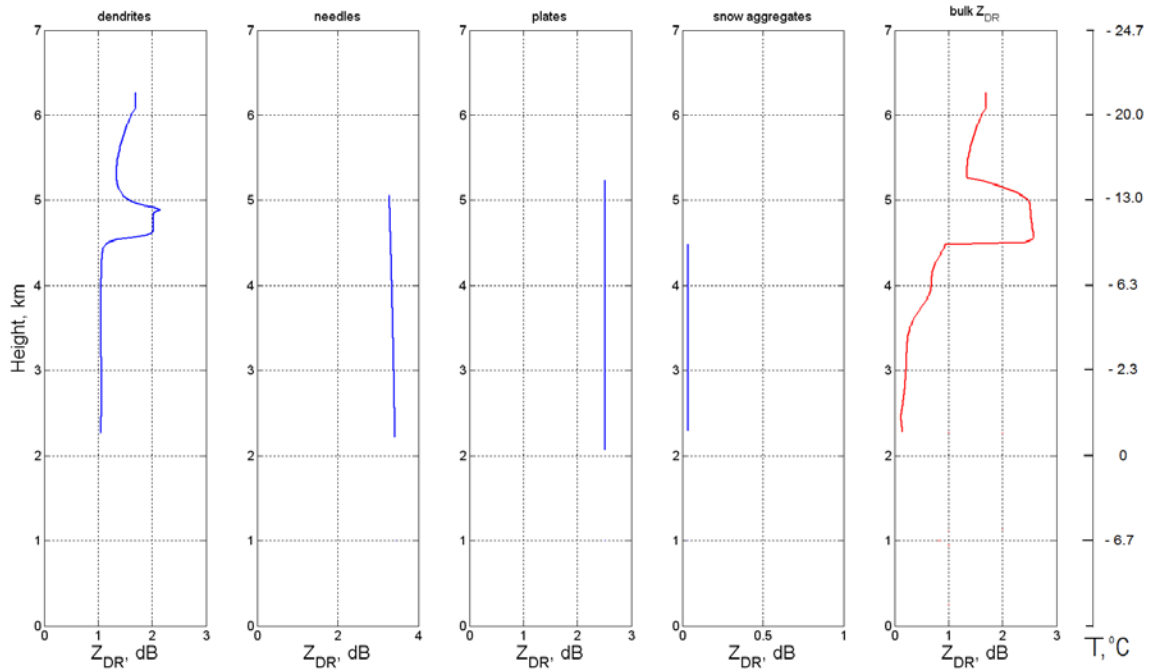
Figure 6.6: As in Fig. 5.4, for calculated Z_{DR}

Cross-correlation coefficient calculated for each ice class and their cumulative sum is presented in Fig. 6.7. As stated in section 3.4, ρ_{hv} depends on diversity in size, shape, orientation and phase composition of particles. Herein, we do not consider dependence on phase composition, because we are concerned only with the ice phase and therefore have omitted the melting process in calculations of the polarimetric variables. The orientation fluctuations are constant with height and affect the quantitative aspect, but not the shape of the calculated signature. Just like in the observations, the modeled signature shows Z_{DR} increasing with height that is coincident with decreasing in ρ_{hv}. Looking at the signature calculated for individual ice classes, notice that ρ_{hv} resembles the Z_{DR} signature. ρ_{hv} signatures for needles, plates and snow are constant. The minimum in ρ_{hv} for dendrites is in the layer from 4.7 to 4.9 km, where it reaches 0.944. Below 4.7 km,

ρ_{hv} increases to 0.986 again and remains constant. Needles have nearly constant ρ_{hv} that ranges from 0.969, at 5 km to 0.975, at 2.5 km. ρ_{hv} for plates is constant and equal to 0.911, and reason for that is constant aspect ratio and density. In the case of snow aggregates, ρ_{hv} is equal to unity because orientation fluctuation is not applied, and it is constant because aspect ratio is constant across the spectrum of sizes.

To analyze the bulk ρ_{hv} , consider the equation 5.36 for calculation of ρ_{hv} and note that integral is divided (normalized) by square root product of Z_H and Z_V. If plates are turned off (excluded from calculation of bulk ρ_{hv}), the bulk ρ_{hv} signature behaves very similar to the ρ_{hv} signature for dendrites (not shown). Bulk ρ_{hv} follows ρ_{hv} for dendrites until needles start contributing (from height 5062 m). Since Z_H and Z_V for needles is lower than for plates (but higher than ρ_{hv} for dendrites), their contribution to the bulk ρ_{hv} is not as significant as in case with plates, so the bulk ρ_{hv} drops but not below 0.96 (it does not decrease to 0.94 which is the minimal value of ρ_{hv} for dendrites). However, if plates are turned on, values are lower, because the product of Z_H and Z_V is larger for plates, so ρ_{hv} is decreased to the intrinsic value of ρ_{hv} for plates.
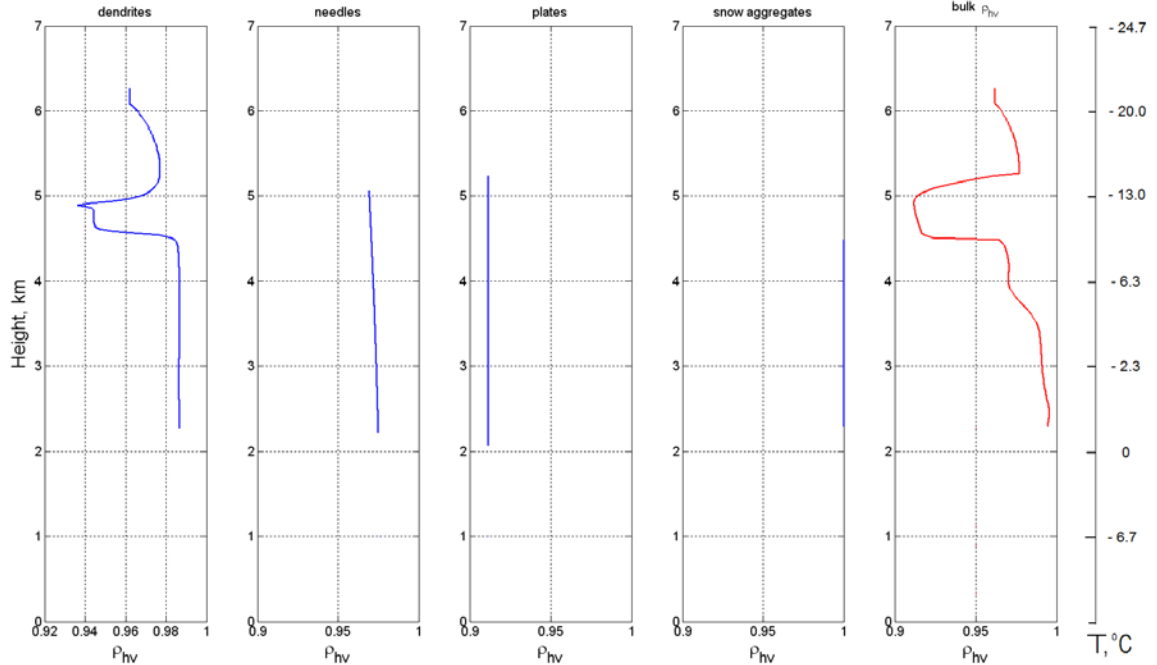
Figure 6.7: As in Fig. 5.4, for calculated ρ_{hv}.

Because the observed K_{DP} is very noisy the vertical profiles were not made. However, K_{DP} calculated for each class individually and their cumulative sum is presented in Fig. 6.8. K_{DP} for dendrites is very low with maximum of 0.011 ° km^{-1} at 4.4 km. Needles have the highest values of K_{DP} 0.15 ° km^{-1} at near 4.2 km, and contribute the most to the cumulative sum. In the case of plates maximum is at 3.8 km. K_{DP} maxima for needles and plates coincide with their total number concentration maxima. As expected, snow aggregates with their low concentration and density have $K_{DP} = 0$ ° km^{-1}, thus they do not contribute to increasing the bulk K_{DP}. Bulk K_{DP} is near 0.2 ° km^{-1} at 4 km. Remember that observed K_{DP} was 0.4 ° km^{-1} in the region of enhanced Z_{DR} (see Figures 4.4 and 4.5).
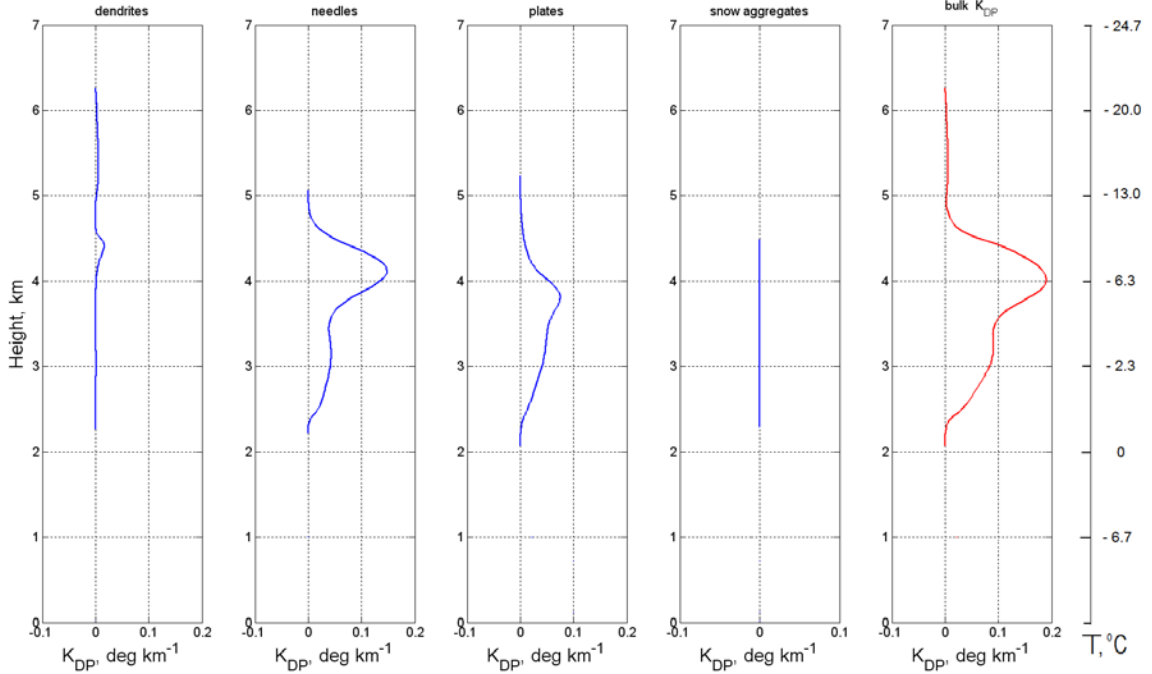
Figure 6.8: As in Fig. 5.4, for calculated K_{DP}.

6.1 Discussion

With the focus on Z_H, Z_V, Z_{DR} and ρ_{hv}, we compare the observed (Fig. 6.9) and modeled polarimetric signatures (Fig. 6.10). The reproduced polarimetric signatures resemble the observed ones. However, the shape of modeled Z_H and Z_V signatures differ significantly from the shape of observed ones. There is an enhancement in modeled Z_{DR} almost matching the height and the value of the observed Z_{DR}. The Z_{DR} maximum occurs in the temperature range of -11.5 °C to -17.2 °C. Although the Z_{DR} signature for dendrites alone resembles the bulk Z_{DR} signature, dendrites are not solely causing the maximum in bulk Z_{DR}. The modeled bulk ρ_{hv} signature agrees well to the observed one in shape but not in the magnitude. The contribution to the modeled Z_H, Z_V, bulk Z_{DR} and ρ_{hv} comes from all four habits considered in the model, where plates contribute the most.

Dendrites have very small diameter (about 35 µm) and high concentration near the cloud top, and therefore their Z_H is negative. Because there is a significant difference between Z_H and Z_V, high Z_{DR} is produced. All ice habits included in the microphysical component of the model are involved in aggregation, but dendrites have higher collection efficiency compared to other ice habits. Thus, the total number concentration of dendrites is more affected by aggregation. In the case where aggregation is turned off, dendrites grow as pristine crystals and produce Z_{DR} of 1 dB (not shown). In that case snow aggregates are not formed and dendrites are not depleted. We conclude that aggregation is responsible for the decrease of concentration of dendrites, due to transport of mass to the snow aggregates. Because of the decrease in concentration of dendrites at approximately 4.9 km, Z_H drops (see Figures 6.2 and 6.4), and with it their contribution to the bulk Z_{DR}. However, from 5.3 km plates are initiated. Within the layer from 5.2 to 4.5 km the oblateness of plates is maximal, and that causes the increase in Z_{DR}. Plates contribute the most to the bulk Z_{DR} as their Z_H is about 10 dBZ within the layer of 5.2 km to 4.5 km, whereas the Z_H of dendrites and needles is negative. Note that this contradicts the speculations of Kennedy and Rutledge (2011), who (based on a limited model) assumed that dendrites were responsible for the Z_{DR} enhancement. Then, from 4.5 km snow aggregates are formed, and because of their high Z_H (20 dBZ) the bulk Z_{DR} is affected causing Z_{DR} to drop from 2.5 to 1 dB.
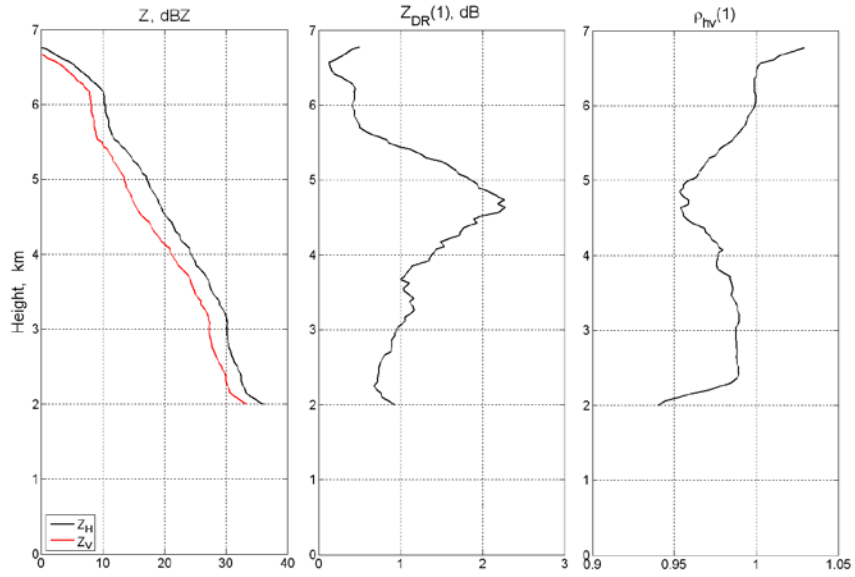
Figure 6.9: Vertical profile of observed Z_H, Z_{DR} and ρ_{hv}.
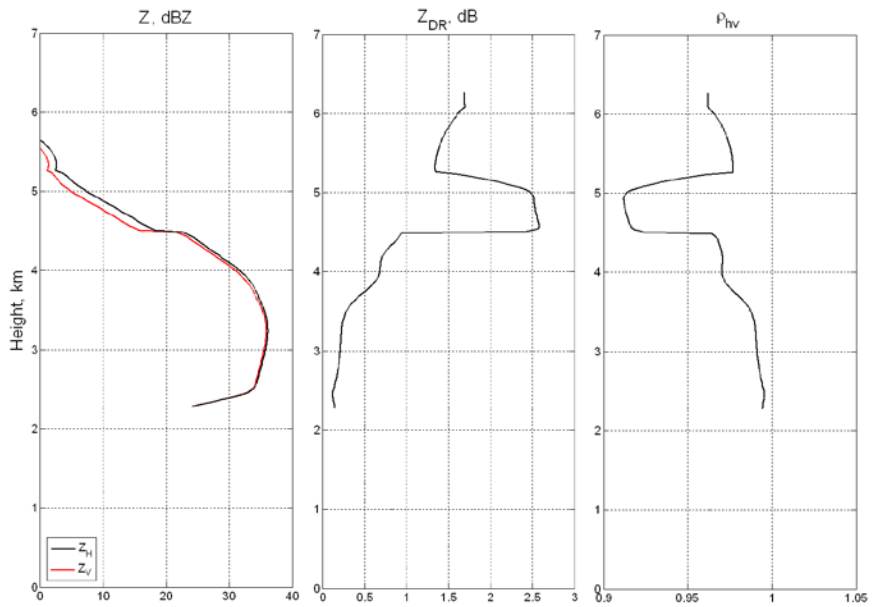
Figure 6.10: Vertical profile of modeled Z_H, Z_{DR} and ρ_{hv}.

The differences of the modeled and the observed polarimetric signature are given bellow along with an explanation for their occurrence.

1) The cloud top height of the modeled signatures (6.3 km) does not match with the observed cloud top height (about 6.8 km). This is partly because particles (dendrites in this case) are too small to be seen by radar.

2) The value of modeled Z_{DR} at the cloud top is too high (about 1.5 dB), which is the result of non-spherical particles (dendrites). The cloud top height of the observed variables is probably caused by nearly spherical particles. Ice particles with axis ratio close to unity and solid ice density are most likely dominate at the cloud top where temperature is around -30 °C and low supersaturation with respect to ice. Fig. 6.11 shows the types of crystals that form in temperature range of -35 °C to -25 °C, and ice supersaturation of 0.1. According to Bailey and Hallett (2008), these crystals are "budding rosette", which describe barely developed bullets, thick plates, columns or rosettes.
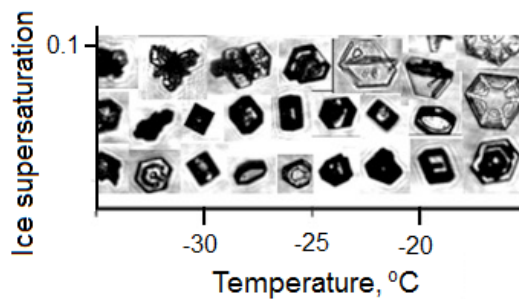
Figure 6.11: A part of the ice crystal habit diagram for low ice supersaturation and temperature range of -15 to -35° C. (Adapted from Bailey and Hallett 2008).

3) The transition from low Z_{DR} to its maximum and following transition back to the low values is sharp, unlike the smooth transition in observed signatures. That is the consequence of simply adding contributions of each ice class, where each class affects a different part of the signature. The observed signature is smoother because real crystals gradually change their shape and size whereas the modeled

82

signature is produced by only 4 dominant ice classes. There are a lot of intermediate crystal habits that occur during the growth process, thus a non-smooth signature is a consequence of parameterization.

4) The lowest part of the modeled Z_{DR} signature from 3.5 km, has lower values than the observed one, since snow aggregates that contribute that part have very low density. This is the consequence of snow aggregates parameterized as spheres in the microphysical component of the code, by which the complex effect of the shape is severely reduced.

5) Modeled ρ_{hv} is too low (0.92) compared to the observed one. It is caused by orientation fluctuation. The chosen value for the width of canting angle distribution σ is suitable for Z_{DR} signature, but it makes ρ_{hv} too low.

6.2 The effect of radar antenna pattern

To demonstrate how the modeled signatures would be observed by radar, the two way antenna weighting function in elevation is appropriately applied. The KOUN radar beamwidth $\theta_1 = 1°$, which at 45 km from the radar corresponds to approximately 750 m. Assume that the antenna patterns for both polarizations are equal and well represented with the Gaussian function. Normalized to unit area the pattern is given by (Doviak and Zrnic 1993):

$$f_n(\theta) = \frac{1}{\sqrt{2\pi}\sigma}\exp\left(-\frac{\theta^2}{2\sigma^2}\right)$$
(6.1)

$$\sigma = \frac{\theta_1}{4\sqrt{\ln 2}}$$
(6.2)

The relation between the model (point reflectivity) and reflectivity the radar would observe is:

$$Z(y_0) = \int f_n(y - y_0)Z(y)dy \qquad (6.3)$$

where $Z(y_0)$ is filtered (smoothed) reflectivity factor, $Z(y)$ the modeled one, y_0 is distance from ground to the center of the beam (that is where the beam is pointing above ground), and y is the variable (distance units) of integration within the beam. The integral is evaluated numerically by summing values at steps of 25 m apart corresponding to the steps in the microphysical model. The equation 6.3 is applied to both Z_H and Z_V, and then Z_{DR} is calculated. A similar procedure was used for obtaining the expected ρ_{hv} signature observed by radar. The procedure is as follows. Radar measures correlation between the $H*$ and V voltages. In the case of very small particles compared to wavelength the backscatter differential phase is zero. Therefore the product $H(y)V(y)$ corresponds to the correlation of voltages from the point y (discrete value in height as given in the microphysical model). The expected value of the product is proportional to $R_{hv}(y) = \rho_{hv}\left(\sqrt{Z_H(y)}\sqrt{Z_V(y)}\right)$. This $R_{hv}(y)$ is weighted by the pattern function same as Z in equation 6.3 to produce $R_{hv}(y_o)$. Then the $\rho_{hv}(y_o)$ is obtained by division as:

$$\rho_{hv}(y_0) = \frac{R_{hv}(y_0)}{\sqrt{Z_H(y_0)Z_V(y_0)}} \qquad (6.4)$$

Both smoothed and modeled signatures of Z_{DR} and ρ_{hv} are presented in Fig. 6.12.
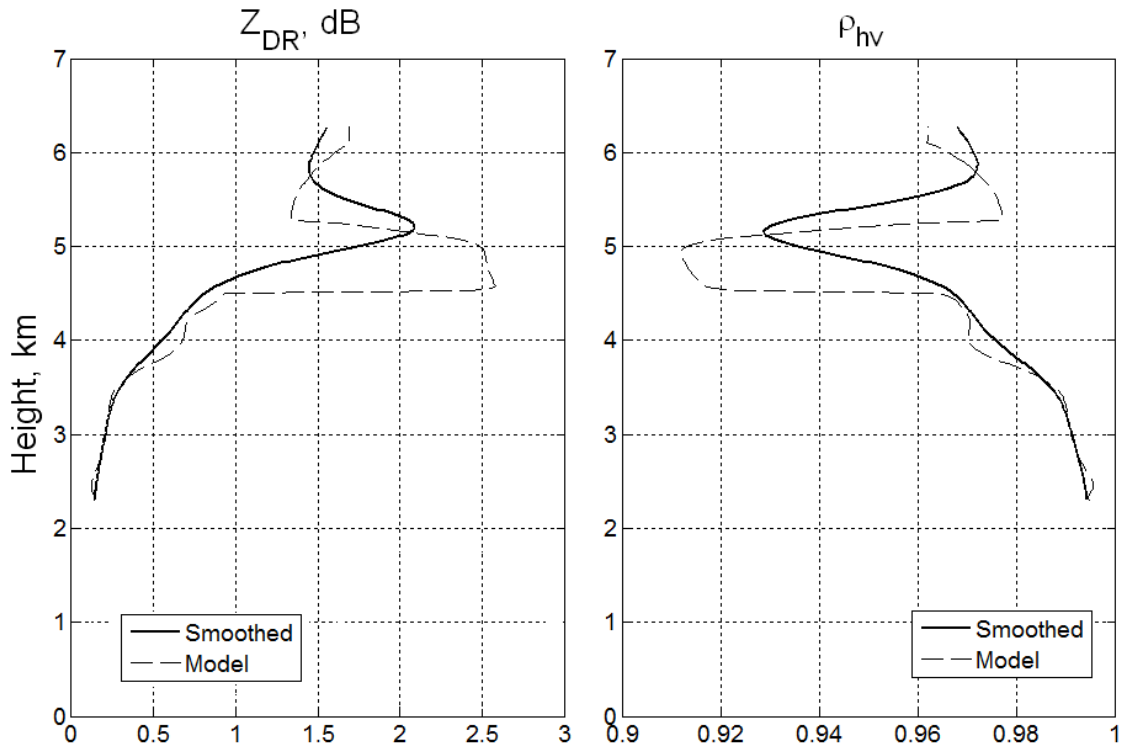
Figure 6.12: The calculated Z_{DR} and ρ_{hv} signature, smoothed by Gaussian weighting function.

The smoothed profiles of Z_{DR} and ρ_{hv} capture the main features of the observations. The general shapes are faithfully reproduced but values of the smoothed Z_{DR} and ρ_{hv} peaks are somewhat reduced, compared to the modeled signatures (see Fig. 6.9). Maximal value of Z_{DR} is 2.1 dB and the minimum of ρ_{hv} is 0.93. Notice that peaks of the smoothed profiles at 5.2 km are at a higher level by 400 m from the level in the case of the modeled signature. Also, the "broken" signature due to sharp transition of the contribution by different ice habit is now smoothed out.

6.3 Summary and implications for future research

A polarimetric radar signature is observed above the freezing level in winter stratiform clouds. This signature is observed as a layer or "pockets" of enhanced Z_{DR} and reduced ρ_{hv} in the temperature range -10 °C to -15 °C.

To aid in the interpretation and quantitative description of this signature, a one-dimensional microphysics scheme coupled with the electromagnetic scattering model was developed. The microphysical scheme accounts for initiation of ice crystals and their subsequent growth by a variety of processes as described in section 5. The electromagnetic scattering component of the model calculates the polarimetric radar variables based on the microphysical output. The model is capable of reproducing basic features of the observed signature. The model indicates that the Z_{DR} enhancement is caused by a decrease in concentration of dendrites, allowing for a greater contribution from plates, which is in disagreement with previous studies. However, there are certain differences between the observed and modeled polarimetric signature. Application of the radar antenna pattern weighting function, smoothes the modeled signature and brings it to closer agreement with the observed one in both qualitative and quantitative aspects.

The more sophisticated microphysics model employed in this study is likely better able to capture the essential physical processes than the previous studies. However, a few changes to the existing model could improve the result. For instance, to increase the modeled Z_{DR} for snow (closer to the observed value, ~0.5 dB) it should be parameterized as spheroids instead of spheres. Furthermore, the model should be modified in such way to allow the effect of weak updraft as well as secondary ice production. These changes

would produce more realistic microphysical conditions, and provide more accurate verification of polarimetric signature.

8. References

Andrić, J., D. Zrnić, and V. Melnikov, 2009: Polarimetric observations of precipitating and non-precipitating clouds. Preprints, 34th *Conference on Radar Meteorology*, Williamsburg, Virginia, Amer. Meteor., Soc. P2.12

Andrić, J., D. Zrnić, J. Straka, and V. Melnikov, 2010: The enhanced Z_{DR} signature in stratiform clouds above the melting layer. Preprints, 13th *Conference on Cloud Physics*, Portland, Oregon, Amer. Meteor., Soc. P2.89

Asai, Tomio, Akira Kasahara, 1967: A Theoretical Study of the Compensating Downward Motions Associated with Cumulus Clouds. *J. Atmos. Sci.*, **24**, 487–496

Bader, M. J., S. A. Clough, and G. P. Cox, 1987: Aircraft and dual polarization radar observations of hydrometeors in light stratiform precipitation. *Q. J. R. Meteor. Soc.*, 113, pp. 491– 515

Bailey, M. P. and J. Hallett, 2009: A comprehensive habit diagram for atmospheric ice crystals: Conformation from the laboratory, AIRS II, and other field studies. *J. Atmos. Sci.*, **66**:2888–2899

Bigg, E. K., 1953: The supercooling of water. *Proc. Phys. Soc. London,* **B66,** 688–694. Bergeron, T., 1935: On the physics of clouds and precipitation. *Proces Verbaux del'Association de Météorologie,* International Union of Geodesy and Geophysics, 156–178.

Braham, Roscoe R., 1964: What is the Role of Ice in Summer Rain-Showers? *J. Atmos. Sci.*, **21**, 640–645.

Cotton, G. J. Tripoli, R. M. Rauber, and E. A. Mulvihill, 1986: Numerical simulation of the effects of varying ice crystal nucleation rates and aggregation processes on orographic snowfall. *J. Climate Appl. Meteor.,* **25,** 1658–1680.

Choularton, T. W., Griggs, D. D., and Hunood, Y., 1980: Laboratory studies of riming, and its relation to ice splinter production. *Quart. J. Roy. Meteor. Soc.,* **106**, 367.

Cohard, J.-M. and Pinty, J. P., 2000: A comprehensive two-moment warm microphysical bulk model scheme: I: Description and tests. Q. J. Roy. Meteor. Soc., 126, 1815–1842.

Doviak, R.J. and D.S. Zrnić, 1993: Doppler Radar and Weather Observations. *Academic Press*, 242 pp.

Doviak, R. J., V. Bringi, A. Ryzhkov, A. Zahrai, D. Zrnić, 2000: Considerations for Polarimetric Upgrades to Operational WSR-88D Radars. *J. Atmos. Oceanic Technol.*, **17**, 257–278.

Evans, K. F., and J. Vivekanandan, 1990: Multiparameter radar and microwave radiative transfer modeling of nonspherical atmospheric ice particles. *IEEE Trans. Geosci. Remote Sens.,* **38,** 423–437.

Findeisen, W., 1938: Kolloid-meteorologische Vorgänge bei Neiderschlags-bildung. *Meteor. Z.,* **55,** 121–133.

Gilmore, M. S., J. M. Straka, and E. N. Rasmussen, 2004a: Precipitation and evolution sensitivity in simulated deep convective storms: Comparisons between liquid-only and simple ice and liquid phase microphysics. *Mon. Wea. Rev.,* **132**, 1897–1916.

Hallett, J., and Mason, B. J., 1958: The influence of temperature nad supersaturation on the habit of ive crystal grown from the vapour. *Proc*. *Roy. Soc. London* **A247**, 440.

Hallett, J., 1964: Experimental Studies of the Crystallization of Supercooled Water. *J. Atmos. Sci.*, **21**, 671–682.

Hallet, J. and Mossop, S. C., 1974: Production of secondary ice particles during the riming process. *Nature*, **249**, 26–28.

Heymsfield, A. J., and Mossop, S. C., 1984:*Quart*. *J. Roy. Meteor. Soc.* **110**, 765.

Hobbs, Peter V., 1969: Ice Multiplication in Clouds. *J. Atmos. Sci.*, **26**, 315–318.

Hobbs, P. V., and Farber, J., 1972: Fragmentation of ice particles in clouds. *H. Dessens Memorial Vol*., *J. de Rech. Atmos.* **6**, 245-258.

Hobbs, P. V. *et al.,* 1971a: *Res. Rept. VI,* Dept. of Atmospheric Sciences, University of Washington, Seattle, Washington.

Hobbs, P. V. *et al*., 1974b: *Res. Rept. VIII,* Cloud Physics Group, Dept. Atmos. Sci., University of Washington, Seattle, Washington.

Hobbs, Peter V., Marcia K. Politovich, Lawrence F. Radke, 1980: The Structures of Summer Convective Clouds in Eastern Montana. I: Natural Clouds. *J. Appl. Meteor.*, **19**, 645–663.

Hogan, R., P. Field, A. Illingworth, R. Cotton, and T. Choularton, 2002: Properties of embedded convection in warm-frontal mixed-phase cloud from aircraft and polarimetric radar. *Quart. J. Roy. Meteorol. Soc.*, **128**, 451 – 476

Isono, K., 1965: *Preprints Cloud Phys. Conf.*, Tokyo, p. 150, Meteor. Soc. of Japan, Tokyo.

Iwai, K.. 1973: On the Characteristic Features of Snow Crystals Developed along c-axis. *J. Meteor. Soc. Japan* **51**, 458.

Jayaweera, K. O. L. F., T. Ohtake, 1974: Properties of Columnar Ice Crystals Precipitating front Layer Clouds. *J. Atmos. Sci.*, **31**, 280–286.

Jiusto, J. E., H. K. Weickmann, 1973: Types of Snowfall. *Bull. Amer. Meteor. Soc.*, **54**, 1148–1162.

Ji, W., 1991: *Ph. D. Thesis,* Dept. Meteor., Univ. of Wisconsin, Madison, Wisconsin.

Kikuchi, K., 1972a: On Snow Crystals with Small Raindrops. *J. Meteor. Soc. Japan* **50**, 142.

Kobayashii, T., 1957: Experimental researches on the snow crystal habit and growth by means of a diffusion chamber. *J. Meteor. Soc. Japan,* **35**, 38-47.

Kobayashi, T., 1958: On the Habit of Snow Crystals Artificially Produced at Low Pressures. *J. Meteor. Soc. Japan* **36**, 193.

Kobayashi, T., 1965a: Vapour Growth of Ice Crystal between -40 and -90 C. *J. Meteor. Soc. Japan* **43**, 359.

Kobayashi, T., 1965b: Contrib. of Inst. Low Temp. *Sci.*, Ser. A, **20**, Hokkaido University, Sapporo, Japan.

Koenig, L. Randall, 1963: The Glaciating Behavior of Small Cumulonimbus Clouds. *J. Atmos. Sci.*, **20**, 29–47.

Koenig, L. R., 1965b: *Preprints Cloud Phys. Conf.,* Tokyo, Japan, p. 242, Meteor. Soc. of Japan, Tokyo.

Kennedy, Patrick C., Steven A. Rutledge, 2011: S-Band Dual-Polarization Radar Observations of Winter Storms. *J. Appl. Meteor. Climatol.*, **50**, 844–858.

Korolev, Alexei, 2007: Limitations of the Wegener–Bergeron–Findeisen Mechanism in the Evolution of Mixed-Phase Clouds. *J. Atmos. Sci.*, **64**, 3372–3375.

Korolev, A., G. A. Isaac and J. Hallett, 1999: Ice particle habits in Arctic clouds. *Geophysical Research Letters*, Vol. **26**, pp.1299-1302

Korolev, A., G. A. Isaac and J. Hallett, 2000: Ice particle habits in stratiform clouds. *Q. J. R. Meteorol. Soc.*, **126,** pp. 2873-2902.

Kumai, Motoi, 1982: Formation of Ice Crystals and Dissipation of Supercooled Fog by Artificial Nucleation, and Variations of Crystal Habit at Early Growth Stages. *J. Appl. Meteor.*, **21**, 579–587.

Kumjian, M.R., and A. V. Ryzhkov, 2008a: Polarimetric signatures in supercell thunderstorms. *J. Applied Meteorology and Climatology*, **47**, 1940 – 1961.

Kumjian, M.R., and A. V. Ryzhkov, 2008b: Microphysical size sorting revealed by dual-polarization Doppler radar. Extended Abstracts, *88th Annual AMS Meeting*, New Orleans, Amer. Meteor. Soc., P2.13.

Kumjian, M.R., S. Ganson, and A. V. Ryzhkov, 2010: Polarimetric characteristics of freezing drops: Theoretical model and practical implications. *5th European Conf. of Radar in Meteorology and Hydrology*, Sibiu, Romania.

Kumjian, M. R., and A. V. Ryzhkov, 2009: Storm-relative helicity revealed from polarimetric radar measurements. *J. Applied Meteorology*, **66**, 667 – 685.

Kumjian, M. R., and A. V. Ryzhkov, 2010: The impact of evaporation on polarimetric characteristics of rain: Theoretical model and practical implications. *J. Applied Meteorology and Climatology*, **49**, 1247 – 1267.

Kumjian, M. R., 2008: Polarimetric radar analysis of microphysical processes in supercell storms. M.S. Thesis, University of Oklahoma, 188 pp.

Lin, Y. L., Farley, R. D., and Orville, H. D. (1983). Bulk parameterization of the snow field in a cloud model. J. Climate Appl. Meteorol., 22, 1065–1092.

List, R., 1958a: Kennzeichen atmosphärischer Eispartikeln, 1. Teil. *Z. angew. Math. Phys.*, **9a**, No. 2, 180-192.

List, R., 1958b: Kennzeichen atmosphärischer Eispartikeln, 2 Teil. *Z. angew. Math. Phys.*, **9a**, No. 3, 217-234.

Locatelli, J. D. and Hobbs, P. V. (1974). Fall speeds and masses of solid precipitation particles. J. Geophys. Res., 79, 2185–2197.

Lo, K. Kenneth, and Richard E. Passarelli, 1982: The Growth of Snow in Winter Storms: An Airborne Observational Study. *J. Atmos. Sci.*, **39**, 697–706.

Magono, C., and Nakamura, T., 1965: Aerodynamic Studies of Falling Snowflakes. *J. Meteor. Soc. Japan,* **43**, 139.

Magono, C. and Lee, C. W.,1966 Meteorological classification of natural snow crystals. J. Fac. Sci., Hokkaido Univ., Ser. VII, 2, 321–335.

Magono, C., and Lee, C. W., 1973: The Vertical Structure of Snow Clouds, as Revealed by "Snow Crystal Sondes", Part II. *J. Meteor. Soc. Japan,* **51**, 176.

Mason, B. J., and Shaw, D., 1955: *J. Meteor.* **12**, 93.

Matsuo, T., and Sasyo, Y., 1981b: Melting of Snowflakes below Freezing Level in the Atmosphere. *J. Meteor. Soc. Japan,* **59**, 10.

Matrosov, Sergey Y., Roger F. Reinking, Robert A. Kropfli, Bruce W. Bartram, 1996: Estimation of Ice Hydrometeor Types and Shapes from Radar Polarization Measurements. *J. Atmos. Oceanic Technol.*, **13**, 85–96.

Maxwell Garnett, J. C., 1904: Color in metal glasses and in metallic films. Philos. Trans. Roy. Soc. London, A203, 385–420.

Melnikov, Valery M., Dusan S. Zrnić, 2004: Estimates of Large Spectrum Width from Autocovariances. *J. Atmos. Oceanic Technol.*, **21**, 969–974.

Melnikov, Valery M., 2007: One-Lag Estimators for Cross-Polarization Measurements. *J. Atmos. Oceanic Technol.*, **23**, 915–926.

Meyers, M. P., P. J. DeMott, and W. R. Cotton, 1992: New primary ice-nucleation parameterizations in an explicit cloud model. *J. Appl. Meteor.,* **31,** 708–721.

Mossop, S. C., Ono, A., and Heffernan, K. J., 1967: Studies of ice crystals in natural clouds. *J. de Rech. Atmos.* **3**, 45.

Mossop, S. C., R. E. Ruskin, K. J. Heffernan, 1968: Glaciation of a Cumulus at Approximately −4C. *J. Atmos. Sci.*, **25**, 889–899.

Mossop, S. C., A. Ono, 1969: Measurements of Ice Crystal Concentration in Clouds. *J. Atmos. Sci.*, **26**, 130–137.

Mossop, S. C., A. Ono, and E. R. Wishart, 1970: Ice particles in maritime clouds near Tasmania. *Quart. J. Roy. Meteor. Soc.,* **96,** 487–508.

Mossop, S. C., Cottis, R. E., and Bartelett, B. M., 1972: Ice crystal concentrations in cumulus and stratocumulus clouds. *Quart. J. Roy. Meteor. Soc.* **98**, 105.

Mossop, S.C. and Hallett, J., 1974. Ice crystal concentration in cumulus clouds: influence of the drop spectrum. Science 186, 632–634.

Mossop, S. C., 1970: Concentrations of Ice Crystals in Clouds. *Bull. Amer. Meteor. Soc.*, **51**, 474–479.

Mossop, S. C., 1971: *Weather* **26**, 222.

Mossop, S. C., 1972: *J. de Rech. Atmos.* **6**, 377.

Mossop, S. C., 1976: Production of secondary ice particles during the growth of graupel riming. Q. J. Roy. Meteorol. Soc., 102, 25–44.

Moisseev, D., E. Saltikoff, and M. Leskinen, 2009: Dual-polarization weather radar observations of snow growth processes. *34ᵗʰ Conference on Radar Meteorology*. Williamsburg, VA, Amer. Meteor. Soc., 13B2. Available online at [http://ams.confex.com/ams/pdfpapers/156123.pdf].

Milbrandt, J. A. and Yau, M. K., 2005: A multimoment bulk microphysics parameterization. Part II: A proposed three-moment closure and scheme description. J. Atmos. Sci., 62, 3065–3081.

Murakami, M., 1990: Numerical modeling of dynamical and microphysical evolution of an isolated convective cloud—The19 July 1981 CCOPE cloud. *J. Meteor. Soc. Japan,* **68,** 107–128.

Nakaya, U., 1954: Snow Crystals*, Harvard University Press*.

Ogura, Y. and Takahashi, T., 1973: The development of warm rain in a cumulus model. J. Atmos. Sci., 30, 262–277.

Ono, A., 1969: The Shape and Riming Properties of Ice Crystals in Natural Clouds. *J. Atmos. Sci.*, **26**, 138–147.

Ono, A., 1970: Growth mode of ice crystals in natural clouds. *J. Atmos. Sci.,* **27,** 649-658.

Ono, A., 1972: *J. de Rech. Atmos.* **6**, 399.

Ohtake, T., 1970b: *Final Rept. Ap-100449,* Geophys. Institute, University of Alaska, Fairbanks, Alaska.

Ohtake, Takeshi, 1970: Factors Affecting the Size Distribution of Raindrops and Snowflakes. *J. Atmos. Sci.*, **27**, 804–813.

Rauber, Robert M., 1987: Characteristics of Cloud Ice and Precipitation during Wintertime Storms over the Mountains of Northern Colorado. *J. Climate Appl. Meteor.*, **26**, 488–524.

Rogers, D. C., 1974a: *Preprints Cloud Phys. Conf.,* Tuscon, Arizona, p. 108, Am. Meteor. Soc., Boston.

Rogers, D. C., 1974b: The aggregation of natural ice crystals. *M*.S. Thesis Res*. Rept. AR110, Dept. of Atmos. Sci*., University of Wyoming, Laramie, WY, 91 pp.

Rogers, R. R. and Yau, M. K., 1989: A Short Course in Cloud Physics. Pergamon. Press.

Ryzhkov, A. V., D. S. Zrnic, B. A. Gordon, 1998: Polarimetric Method for Ice Water Content Determination. *J. Appl. Meteor.*, **37**, 125–134.

Ryzhkov, Alexander V., 2001: Interpretation of Polarimetric Radar Covariance Matrix for Meteorological Scatterers: Theoretical Analysis. *J. Atmos. Oceanic Technol.*, **18**, 315–328.

Ryzhkov, A., M. Pinsky, A. Pokrovsky, A. Khain, 2011: Polarimetric Radar Observation Operator for a Cloud Model with Spectral Microphysics. *J. Appl. Meteor. Climatol.*, **50**, 873–894.

Passarelli, R. E. and Srivastava, R. C., 1979: A new aspect of snowflake aggregation theory. J. Atmos. Sci., 36, 484–493.

Palmer, R.D., D. Bodine, M.R. Kumjian, B. Cheong, G. Zhang, Q. Cao, H.B. Bluestein, A.V. Ryzhkov, T.-Y. Yu, and Y. Wang, 2011: Observations of the 10 May 2010 tornado outbreak using OU-PRIME: Potential for new science with high-resolution polarimetric radar. *Bull. Amer. Meteor. Soc.*, **in press**.

Plummer, David M., Sabine Göke, Robert M. Rauber, Larry Di Girolamo, 2010: Discrimination of Mixed- versus Ice-Phase Clouds Using Dual-Polarization Radar with Application to Detection of Aircraft Icing Regions*. *J. Appl. Meteor. Climatol.*, **49**, 920–936.

Pruppacher, H. R. and Klett, J. D.,1997: Microphysics of Clouds and Precipitation, 2nd edn. Dordrecht: Kluwer Academic Publishers.

Sasyo, Y., and Matsuo, T., 1980: *Papers* in *Meteor. and Geophys., Japan* **31**, 61.

Seliga, T. A., V. N. Bringi, 1976: Potential Use of Radar Differential Reflectivity Measurements at Orthogonal Polarizations for Measuring Precipitation. *J. Appl. Meteor.*, **15**, 69–76.

Straka M. J., 2009: Cloud and Precipitation Microphysics, Cambridge University Press, Cambridge

Vali, G., 1980:*Preprints Cloud Phys. Conf.,* Clermont-Ferrand, p. 227, Blaise Pascal Université, Aubière, France.

Vardiman, L., 1974: *Sci. Paper 230,* Dept. Atmos. Sci., Colorado State University.

Wang, P. K. and Ji, W., 1992: A numerical study of the diffusional growth and riming rates of ice crystals in clouds. Preprints volume, *11th International Cloud Physics Conference*, August 11–17, Montreal, Canada.

Woods, Christopher P., Mark T. Stoelinga, John D. Locatelli, 2008: Size Spectra of Snow Particles Measured in Wintertime Precipitation in the Pacific Northwest. *J. Atmos. Sci.*, **65**, 189–205.

Wegener, A., 1911: *Thermodynamik der Atmosphäre*. Leipzig, 331 pp.

Wisner, C., H. D. Orville, and C. Meyers, 1972: A numerical model of a hail-bearing cloud. *J. Atmos. Sci.,* **29,** 1160–1181.

Young, K. C. 1974: A numerical simulation of wintertime, orographic precipitation: Part I. Description of model microphysics and numerical techniques. *J. Atmos. Sci.*, **31**, 1735-1748.

Young, K. C., 1974a: The role of contact nucleation in ice phase initiation in clouds. *J. Atmos. Sci.,* **31,** 768–776.

Young, K. C., 1974b: A numerical simulation of wintertime, orographic precipitation. I: Description of model microphysics and numerical techniques. *J. Atmos. Sci.,* **31,** 1735–1748.

Young, K. C., 1993: Microphysical processes in clouds. Oxford university press, Oxford, page 427

Zrnić, Dusan S., Alexander V. Ryzhkov, 1999: Polarimetry for Weather Surveillance Radars. *Bull. Amer. Meteor. Soc.*, **80**, 389–406.